



LABYRINTH SEAL OPTIMIZATION AND ITS EFFECT ON ROTOR DYNAMICS IN A TURBOMACHINE

Lappeenranta–Lahti University of Technology LUT

Master's Thesis

2023

Lauri Rauhala

Examiners: Professor Jussi Sopanen

Tuhin Choudhury, D. Sc.

ABSTRACT

Lappeenranta–Lahti University of Technology LUT

LUT School of Energy Systems

Mechanical Engineering

Lauri Rauhala

Labyrinth seal optimization and its effect on rotor dynamics in a turbomachine

Master's thesis

2023

101 pages, 54 figures, 12 tables and 7 appendices

Examiners: Professor Jussi Sopanen and Tuhin Choudhury, D.Sc. (Tech)

Keywords: Labyrinth seal, contactless seal, leakage optimization, rotor dynamics, seal effect to rotor dynamics, turbomachine, axial forces optimization

The objective of the research was to study what are the most relevant labyrinth seal design variables including different geometrical dimensions, the number of blades, and seal location to affect leakage, and how much they affect individually. Also, which seal variables affect rotor instability, their individual impacts, and the relationship between leakage, radial labyrinth seal location, and axial thrust in a radial compressor impeller was studied.

Computational Fluid Dynamics and three different analytical methods, Egli's, Martin's, and Kearton's methods, were used in leakage calculations. Black's and Child's methods were used to obtain seal rotor dynamic coefficients. Alford's and Wachel's methods were used in calculation of impeller aerodynamic cross-coupled stiffnesses. A rotor dynamic model was made using input values from high temperature heat pump compressor design project. The effect of change in seal rotor dynamic coefficients and impeller aerodynamic stiffnesses to natural frequencies and damping ratios were studied.

The main findings were that seal radius, clearance, and blade shape have a major effect, chamber width and number of blades have a moderate effect, and blade height and width have a minor effect on leakage. Other main findings were that only seal length and clearance affect rotor dynamic coefficients, and the effect of labyrinth seal and impeller aerodynamic cross-coupled stiffness to natural frequencies and damping ratios is small. It was concluded that, in a radial seal, the closer the seal is to the rotor, the smaller the leakage, but the larger are the axial forces, and vice versa.

TIIVISTELMÄ

Lappeenrannan–Lahden teknillinen yliopisto LUT

LUT Energiajärjestelmät

Konetekniikka

Lauri Rauhala

Labyrinttitiivisteiden optimointi ja sen vaikutus roottoridynamiikkaan

Konetekniikan diplomityö

2023

101 sivua, 54 kuvaa, 12 taulukkoa ja 7 liitettä

Tarkastajat: Professori Jussi Sopanen ja Tuhin Choudhury, D.Sc.

Avainsanat: Labyrinttitiiviste, kontaktiton tiiviste, vuodon optimointi, roottoridynamiikka, tiivisteiden vaikutus roottoridynamiikkaan, turbokone, aksiaalivoimien optimointi

Tutkielman tehtävänä oli tutkia mitkä labyrinttitiivisteiden suunnittelutekijät, mukaan lukien eri geometriset mitat, terien lukumäärä ja tiivisteiden paikka, vaikuttavat tiivisteiden vuotoon, sekä kuinka paljon eri muuttujat vaikuttavat itsenäisesti. Tehtävänä oli tutkia myös, mitkä labyrinttitiivisteiden muuttujat vaikuttavat roottoridynamiikkaan epätasapainoon ja kuinka paljon, sekä miten radiaalisen labyrinttitiivisteiden paikan muutos vaikuttaa vuotoon.

Labyrinttitiivisteiden vuodon laskemiseen käytettiin tietokonepohjaista fluididynamiikan laskemismenetelmää ja kolmea erilaista analyttistä menetelmää, Eglin, Martinin, ja Keartonin menetelmää. Blackin ja Childin menetelmiä käytettiin roottoridynamiikan kerrointen laskemisessa. Alfordin ja Wachelin menetelmiä käytettiin siipipyörän aerodynaamisen ristijäykkyyden laskemisessa. Korkealämpötilalämpöpumpun suunnitteluprojektin tietoihin pohjaten luotiin roottoridynamiikan malli. Labyrinttitiivisteiden roottoridynamiikan kerrointen ja siipipyörän aerodynaamisen ristijäykkyyden muutosten vaikutusta luonnolliseen värähtelytaajuuteen ja vaimennussuhteisiin tutkittiin.

Tärkeimmät löydökset olivat, että tiivisteiden säteellä, välyksellä ja terän muodolla oli suuri vaikutus, kammion leveydellä ja terien määrällä oli keski-suuri vaikutus, ja että terän korkeudella ja leveydellä oli vähäinen vaikutus vuotoon. Muita tärkeitä löydöksiä olivat, että vain tiivisteiden aksiaalinen pituus ja välyys vaikuttavat roottoridynamiikkaan kertoimiin, ja että labyrinttitiivisteiden ja siipipyörän aerodynaamisen ristijäykkyyden tuomat vaikutukset luonnolliseen värähtelytaajuuteen ja vaimennussuhteisiin olivat vähäisiä. Yhtenä tärkeänä johtopäätöksenä oli, että mitä lähempänä tiiviste on roottoria radiaalisessa labyrinttitiivisteessä, sitä pienempi on vuoto, mutta sitä suuremmat ovat aksiaalivoimat, ja toisin päin.

ACKNOWLEDGEMENTS

First, I would like to thank D.Sc Tuhin Choudhury for giving a huge amount of support and guidance during spring 2023, especially with MATLAB and rotor dynamic problems. The thesis would have been incredibly difficult without Tuhin's support. I also want to thank Prof. Jussi Sopanen for the opportunity for this thesis and work as a mechanical designer in HT COMP project. I also want to thank D.Sc Eerik Sikanen, D.Sc Petri Sallinen, and D.Sc Ahti Jaatinen-Värri for supporting in individual problems. Lastly, I want to thank my wife Riina Korhonen, who was very supportive along the journey.

SYMBOLS AND ABBREVIATIONS

Symbols

A	surface area of leakage gap	[m ²]
B	chamber width	[m]
\mathbf{C}	damping matrix	
C_d	discharge or damping coefficient	[unitless], [N · s/m]
c	seal clearance	[m]
c_c	cross coupled damping coefficient	[N · s/m]
D	impeller blade pitch mean diameter	[m]
e	Euler's number or radial displacement	[unitless], [m]
F	pressure difference correction factor or force	[unitless], [N]
\mathbf{G}	gyroscopic matrix	
H	impeller blade height	[m]
hp	power in horse powers	[hp]
I_p	polar moment of inertia	[kgm ²]
\mathbf{K}	stiffness matrix	
K_d	direct stiffness coefficient	[N/m]
k_c	cross coupled stiffness coefficient	[N/m]
k_ω	rotation coefficient	[unitless]
L	length of the seal	[m]
\mathbf{M}	mass matrix	
M_g	gyroscopic momentum	[kg · m/s]
M_w	molecular weight of fluid	[g/mol]
m_d	principal inertia coefficient	[kg]
m_u	unbalance mass	[kg]
N_T	state shape function	[unitless]
N_R	state shape function	[unitless]
n	number of seal blades	[unitless]

p	pressure	[Pa]
q_m	mass flow	[kg/s]
$\mathbf{q}, \dot{\mathbf{q}}, \ddot{\mathbf{q}}$	displacement, velocity, acceleration vectors	
r	seal radius	[m]
R	gas constant	[J · kg ⁻¹ · K ⁻¹]
Re	Reynolds number	[unitless]
R_a	Axial Reynolds number	[unitless]
R_c	Circumferential Reynolds number	[unitless]
t	width of labyrinth seal blade	[m]
T	temperature or torque	[K], [Nm]
u	circumferential speed	[m/s]
v	specific volume	[kg/m ³]
w	velocity	[m/s]
x, \dot{x}, \ddot{x}	displacement, velocity, acceleration	[m], [m/s], [m/s ²]
Z	b / h	[unitless]
z	eigenvector	

Greek characters

α	flow coefficient or inlet swirl ratio	[unitless]
β	efficiency factor	[unitless]
ζ	entrance loss factor or damping ratio	[unitless]
ε	kinetic energy carryover coefficient	[unitless]
ϕ	total area factor	[unitless]
γ	C_p / C_v	[unitless]
$\dot{\theta}$	angular velocity change	[unitless]
φ	expansion factor for labyrinth seal	[unitless]
π	pressure ratio or relation of circle ring to its diameter	[unitless]
ρ	density	[kg/m ³]
λ	friction loss factor or eigenvalue	[unitless]

μ	gas kinematic viscosity or fluid viscosity	[m ² /s], [Pa · s]
ψ	expansion factor for a single constraint	[unitless]
Ω	rotational velocity	[rad/s]
Δ	change in a parameter	[unitless]
σ	nonlinear function of mean axial velocity	[unitless]

Subscripts

0	before the seal
1, 2, 3 etc.	chamber number 1., 2., 3. etc. or blade number 1., 2., 3. etc.
min	minimal value
max	maximum value
n	nth chamber or blade
rot	rotating
stat	static
th	theoretical
u	tangential
d	principal term or value at impeller discharge
c	cross coupled term or corrected term
i	value in inches
d	value at impeller discharge
s	value at impeller suction
x, y, z	direction along axis

Abbreviations

CAD	Computer Aided Design
CFD	Computational Fluid Dynamics
COP	Coefficient of Performance
FEM	Finite Element Method
HP	Heat Pump
HPC	High Pressure Compressor
HT COMP	High Temperature Heat Pump Compressor
LPC	Low Pressure Compressor
LUT	Lappeenranta University of Technology
R2B	Research to Business
RPM	Revolutions per Minutes
SDG	Sustainable Development Goal

Table of contents

abstract

tiivistelmä

acknowledgements

symbols and abbreviations

table of contents

1	Introduction	11
1.1	Background and motivation	13
1.2	Labyrinth seals	14
1.3	High temperature heat pump compressor project	19
1.4	Research problem.....	20
1.5	Objectives.....	21
1.5.1	Research questions.....	21
1.5.2	Hypotheses.....	21
1.6	Scope	22
1.7	Structure of thesis.....	22
2	Methods for optimization and analysis of labyrinth seal leakage and rotor dynamics	24
2.1	Analytical methods for leakage optimization	24
2.2	Computational methods for leakage optimization	28
2.3	Dynamic coefficients for an axial seal	29
2.4	Aerodynamic cross-coupled stiffness caused by an impeller	35
2.5	Rotor dynamic theory.....	36
2.6	Rotor-Bearing Dynamics toolbox	41
2.7	Calculation of axial forces caused by an impeller	41
3	Results	43
3.1	Case study	43
3.2	Leakage optimization	45
3.2.1	Ansys Fluent Computational Fluid Dynamic – CFD.....	47

3.2.2	Results of leakage calculation.....	49
3.3	Dynamic coefficients for an axial seal	63
3.4	Aerodynamic cross-coupled stiffness caused by an impeller	72
3.5	Rotor dynamic analysis	73
3.6	Effect of radial seal placement on axial forces	80
4	Discussion.....	86
4.1	Leakage optimization	86
4.2	Rotor dynamic analysis	90
4.3	Effect of radial seal placement on axial forces	92
5	Conclusions	94
	References.....	97
	Appendix 1. Matlab code for leakage of axial seal with Egli's equation	102
	Appendix 2. Matlab code for leakage of radial seal with Kearton's equation.....	104
	Appendix 3. Matlab code for leakage of radial seal with Martin's equation.....	105
	Appendix 4. Matlab code for axial thrust created by an impeller.....	106
	Appendix 5: Matlab code for axial seal dynamic coefficients with Black's method	115
	Appendix 6: Matlab code for axial seal dynamic coefficients with Child's method.....	117
	Appendix 7: Matlab code for aerodynamic cross-coupled stiffness by an impeller.....	119

Appendices

Appendix 1. Matlab code for leakage of axial seal with Egli's equation

Appendix 2. Matlab code for leakage of radial seal with Kearton's equation

Appendix 3. Matlab code for leakage of radial seal with Martin's equation

Appendix 4. Matlab code for axial thrust created by an impeller

Appendix 5. Matlab code for axial seal dynamic coefficients with Black's method

Appendix 6. Matlab code for axial seal dynamic coefficients with Child's method

Appendix 7. Matlab code for aerodynamic cross-coupled stiffness by an impeller

1 Introduction

A turbomachine can be defined as a machine where energy is delivered either from a continuous fluid flow to a rotational element, known as a rotor, or from a rotational element to fluid flow. If a turbomachine uses continuous fluid flow to drive the rotor, it is known as a power delivering application, more commonly known as a turbine. Turbines are common in energy producing applications such as wind turbines, hydro-turbines in dams, steam turbines in nuclear plants or gas turbines in jet engines. (Dick 2022, p. 1.)

In reverse, if a turbomachine uses an external motor to drive the fluid flow, it is known as a power receiving application. These applications can be divided into two categories based on what type of fluid they are moving: incompressible fluids and compressible fluids. Turbomachines that drive incompressible fluids, usually oil or water, are known as pumps. Turbomachines that move compressible fluids, such as air, gas or steam can be yet divided into two categories: low-pressure and high-pressure systems. Compressible fluid driving turbomachines working with low pressures are typically fans, and one that work with high pressure are known as compressors. The main function of pumps and compressors is to move fluid by increasing pressure in the system. (Dick 2022, p. 1.)

During recent decades, high-speed rotating machines have been researched intensively and they have become more common across industries due to their improved size-power ratio (power-density) and energy-efficiency. High-speed rotating machine applications usually operate without a gearbox, which makes them more reliable than traditional ones. As shown in Table 1, high-speed rotating applications typically operate in working speeds between tens of thousands of rpm (revolutions per minute) to hundreds of thousands of rpm transferring huge amounts of power. (Rosu 2021, p. 11.; Prasad 2021, p. 2.)

Table 1. Rotational velocities of different turbomachines. (Prasad 2021, p. 2)

Application	Speeds (power)
Automotive/ power generation (more electric engine)	220,000 rpm (2 kW), 35,000 rpm (150 kW)
Fly-wheel energy storage	40,000 rpm (up to 120 kW)
High-speed spindles	9,000 to 180,000 rpm (24 - 1 kW)
Turbo-molecular pumps	100,000 rpm (hundred's of watt)
Gas compressors	20,000 rpm (10 MW)
Air compressors and air blowers	80-15,000 rpm (100-150 kW)
Micro-turbines	80,000 rpm (50 kW)

Although clear advantages come with high-speed rotation machines, there are also challenges. Use of traditional bearings is complicated due to the increased friction and wearing significantly decreases the life cycle of a bearing. For this reason, many high-speed rotating machines use contactless bearings such as gas, oil, or magnetic bearings instead of traditional ball bearings. From these options, magnetic bearings are thought to be the best options due to their freedom of lubrication and maintenance. Additional challenges faced when operating at high speeds are high friction caused by viscosity of the fluid and high stresses and possible deformations of the rotating elements. These challenges can be solved by using correct materials and weight-optimized design. (Prasad 2021, p. 2.; Rosu 2021, p. 11.)

The theory behind rotor vibration has been already developed widely in the end of 19th century. The locomotive and steam engine industry accelerated growing interest towards high-speed machinery. During the late 19th century, vast research on rotor vibration was made by Dunkerley and Reynolds. De Laval researched and experimented with steam turbines solving most of rotor dynamic problems that were considered relevant in those days. The shaft whirling problem was analytically resolved by A. Föpl. During the late 19th century and early 20th century, the research of Rankine, Jeffcott and A. Stodola form a basis of modern rotor dynamic analysis. (Dimarogonas 2013, p. 1–2.)

Rotor vibration occurs when the mass of the rotor or its inertia properties are distributed in a non-uniform way creating unbalance. In other words, the rotors main axes of inertia are not aligned with the geometrical axes of symmetry and the mass center is not aligned to the

bearing center line. (Nayek 2020, p. 4.) Controlling rotor vibration is an important element of failure prevention in rotational machines.

1.1 Background and motivation

Creating energy-efficient innovations in the fields of energy and electrical motor applications has a large impact in creating a more sustainable future. The world's energy use in 2015 was approximately 21000 TWh according to International Energy Agency report made in 2015, and it is estimated to rise more than 30% by 2030. In 2015, electrical machines accounted for approximately 40% of the electric energy demand, therefore innovating more energy-efficient electrical machinery directly affects controlling the global warming. (Uzhegov 2016, p. 13.)

High-speed rotating electrical applications are a part of the electric machines field. The markets using high-speed rotating electrical application has grown exponentially during the last decades. The challenges described in the previous chapters has led to vast research in the field. Lappeenranta University of Technology (LUT) has been researching high-speed rotating machines for over 30 years. LUT has had, and also currently has, numerous projects about high-speed rotating machines together with different industry operators. (Uzhegov 2016, p. 13–14.)

In high-speed rotating machines, it is crucial to separate the rotating components from the stationary components preventing the flow leakage as well as possible as the leakage directly affects the efficiency of the machine. (Wróblewski 2018, p. 726) Sealing between the rotor and the stator can be done using a wide range of solutions for a wide range of applications. Even though different applications have different demands, same seal types can be found in totally different applications. For example, mechanical seals are used in aircraft jet engines as well as in consumer washing machines. There typically is not a rotational seal that dominates in one specific application, but they are rather selected based on boundaries given by operating conditions, such as space, amount of friction, allowable leakage, and reliability. (Flitney 2014, p. 105.) Because of the high speeds used in these applications as well as high temperatures, contactless seals are typically used. The most commonly used contactless seal is the labyrinth seal shown in Figure 1 below. (Wróblewski 2018, p. 726.).

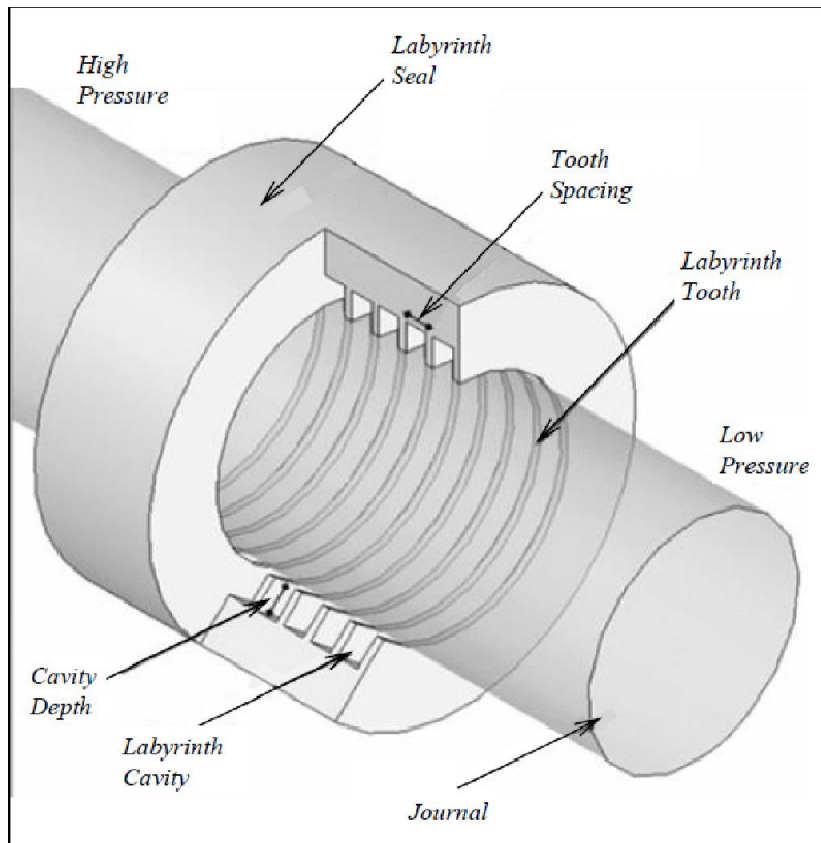


Figure 1. Labyrinth seal. (Woo 2011, p. 2)

1.2 Labyrinth seals

Rotational contactless seals are widely used technology in applications such as turbines, centrifugal compressors, and turbomachines. The popularity of the seal is based on its simplicity and low manufacturing and maintenance costs. In contactless seal there is always a gap between the stator and the rotor meaning that there is no abrasion between them, such as in a mechanical seal for example. This results in minimal maintenance. Another advantage of contactless seals is that they work well in high speeds. (Baha 2021, p. 1.; Tisarev 2024, p. 1.; Flitney 2014, p. 238.)

Labyrinth seal is a contactless seal, where pressure and flow are reduced by consecutive chambers as shown in Figure 2. As the fluid travels through the labyrinth seal, it experiences consecutive restrictions and volume expansions which causes the pressure to reduce. (Flitney 2014, p. 238.) As the fluid comes out of a chamber, only part of the original pressure recovers. The velocity of the fluid increases when it passes the restriction phase, which is

where the distance between the blade and the stator is at its minimum. The smaller the width of a chamber and the sharper the edges of the blade, the less partial pressure recovery happens after every chamber and therefore the more efficient the seal is. After the restriction phase the fluid continues to a chamber, where the flow changes to turbulent and the kinetic energy of the fluid reduces. Because of the inner friction of the fluid, some of the kinetic energy converts into heat which causes the pressure to drop between the chambers. (Aslan-Zada 2013, p. 216.)

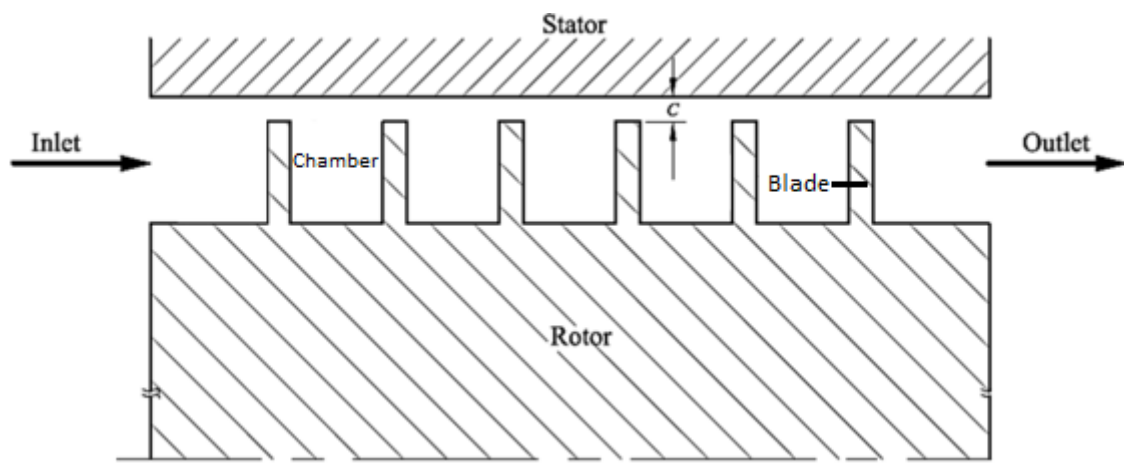


Figure 2. Labyrinth seal, where the blades are in rotor side. c is the seal clearance. (Subramanian 2018, p. 267)

If compressible fluid is used instead of incompressible fluid, it expands as it flows from the inlet (high pressure) to the outlet (low pressure). Volume flow increases and mass flow stays constant. The velocity of the fluid increases towards the outlet of the seal.

Labyrinth seals need a clearance between the rotor and the stator. This is sometimes called a gap. The smaller the gap, the less leakage there is and therefore more efficient the operation is. On the other hand, the gap needs to be large enough to allow proper installation, vibration of the rotor and thermal expansion. Apart from decreasing the gap, the efficiency can also be increased by increasing the number of blades and chambers and optimizing the geometry of the seal. (Aslan-zada 2013, p. 3.)

Labyrinth seals can be used to protect bearings or for sealing the working fluid from entering from the high-pressure side to the low-pressure side. When it comes to turbomachinery, the latter is the purpose of their use. Labyrinth seals are commonly used in gas or steam turbines

and in centrifugal gas compressors. Traditionally, labyrinth seals have been used between the atmosphere and the working fluid, but since more efficient ways were invented for that purpose, such as dry gas seals, labyrinth seals are not commonly used any more between the working fluid and the atmosphere. Instead, labyrinth seals are more commonly used as inner seals to prevent working fluid from leaking too much inside different parts of the machine. If the system is closed, meaning there is a hermetic sealing between the working fluid and the atmosphere, and small leakages are allowed between the insides of the system, labyrinth seals are a good solution due to their simplicity, price, and easy manufacturability. (Flitney 2014, p. 237.)

Optimizing labyrinth seal design has a large impact on the efficiency of the machine. The more leakage, the worse efficiency. Decreased efficiency can result in increased energy consumption. Worn labyrinth seal can result to an annual 1% increased energy consumption in a large turbomachine. Reducing the clearance as much as possible as well as optimizing the shapes of the blades, chamber dimensions, chamber edges, and the number of chambers being the most important parameters when optimizing labyrinth seals. (Flitney 2014, p. 237.) Normally, the gap when the system is running, is somewhere between 0.25 – 0.50 mm. (Aslan-zada 2013, p. 216)

There are different types of contactless seals, such as half labyrinth seals, full labyrinth seals, stepped labyrinth seals, and honeycomb seals acting either axially or radially depending on the application. (Childs 2014, p 582) Half labyrinth seal has chambers and blades on one side and flat surface in the opposing side as shown in Figure 3. Blades and chambers can be machined either to the rotor or to the stator. The advantage is its simplicity and easy assembly in axial direction. The disadvantage is that some of the fluid flows along the straight face without entering the chamber allowing more leakage compared, for example, to full labyrinth seals. The extra leakage from the half labyrinth seal compared to full labyrinth seal is estimated to be around 20 – 30% higher. (Flitney 2014, p. 237.)

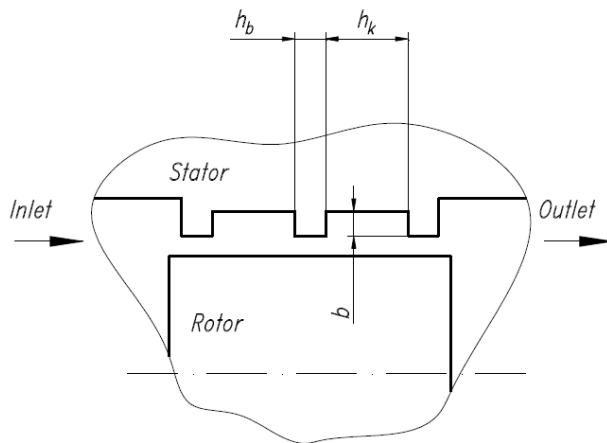


Figure 3. Half labyrinth seal: h_b – blade width, h_k – chamber width, b – clearance. (Ivanova 2015, p. 127)

A full labyrinth seal has blades on both rotor and stator side, as shown in Figure 4. Compared to a half labyrinth seal, the main advantage of a full labyrinth seal is decreased leakage due to the lack of a straight surface making the travel of the fluid more complicated. The disadvantage of a full labyrinth seal is that it is usually not possible to assemble axially. Because of this, full labyrinth seals are more commonly used in radial direction. (Flitney 2014, p. 237.)



Figure 4. Full labyrinth seal. (Woo 2011, p. 3)

In a stepped labyrinth seal the rotor side is flat but stepped, while the stator side has chambers and blades as shown in Figure 5. The clearance between the blade and the stator is uniform throughout the seal. Stepped labyrinth seals are more efficient in terms of leakage compared to half labyrinth seals. Stepped labyrinth seals can be assembled axially, but only from one side, where half labyrinth seals can be assembled from both sides. Compared to half labyrinth seal, the stepped labyrinth seal is much more complex to manufacture. (Flitney 2014, p. 244.)

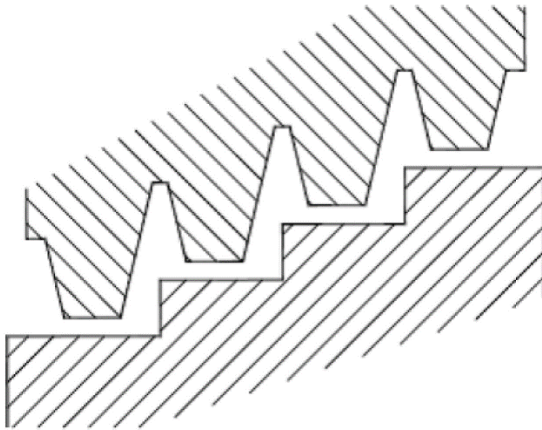


Figure 5. Stepped labyrinth seal. (Aslan-zada 2013, p. 216)

Abradable seals work by intentionally wearing a softer counterpart of the seal in operation. This way it is possible to achieve a smaller gap between the rotor and the stator compared to conventional seals as shown in Figure 6. The softer, abradable counterpart is usually a changeable ring, which is assembled to the stator side, because it is easy to maintain and change. During installation phase, there is a gap between the blades and the abradable ring. When the operation starts and the rotor expands due to heat, the blades and the abradable ring collide. After the blade wears an engravingment to the softer part, the gap between the ring and the blade is very small making the leakage minimal. (Flitney 2014, p. 244.)

	Installation	Transition (initial rub)	Transition (after rub)	Normal operation
Conventional seal				
	Normal clearance	Fins contacts rotor	Contact continues until seal wear	Increase of clearance
Abradable seal				
	Reduced clearance	Fins cut coating	Fin and metal don't touch fin shape is kept	Clearance at normal position is kept

Figure 6. The difference between conventional seals and abradable seals in operation (Enomoto 2017, p. 430)

There are different blade shapes in labyrinth seals. In Figure 7 are presented most common geometries, which are slanted, straight flat and straight sharp. In the figure, the examples show only half labyrinth seals, but the different shapes can be used for other labyrinth seal types as well. All these can have different characteristics. For example, the slanted shape, because of the inclined chamber, trap more fluid in the chambers compared to straight blades, making it more effective. The straight sharp blade creates more turbulence to the flow compared to the straight flat. (Aslan-zada 2013, p. 216.)

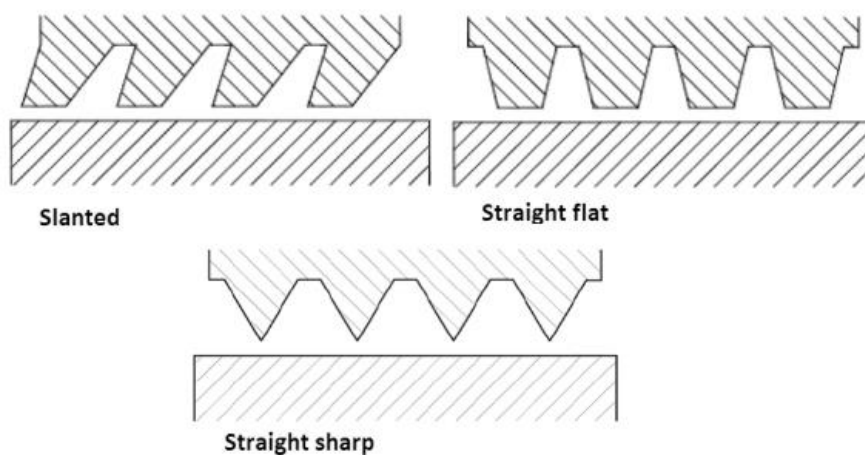


Figure 7. Different shapes of labyrinth seal blades: slanted, straight flat, and straight sharp. (Aslan-zada 2013, p. 216)

1.3 High temperature heat pump compressor project

The results of this thesis work are used in a project called HT COMP, which comes from the words high temperature heat pump compressor. The objective of the project is developing a megawatt class compressor for a high temperature heat pump. The project is a LUT University research-to-business (R2B) project funded by Business Finland. The project group consists of experts from LUT University and relevant industries from fields of machine dynamics, fluid dynamics and business.

In the Finnish market, there are manufacturers who specialize in electric machines, heat exchangers, and heat pumps, but there are no compressor manufacturers who specialize in heat pumps. In the market, there are no available compressors in mega-watt class. To create a unique product, stand-out from the competitors, and be sustainable, the product needs to

be mega-watt class, oil-free, produce high temperatures, have low maintenance, high capacity, use carbon neutral refrigerants and have a high coefficient-of-performance (COP).

The final product is estimated to provide operating cost reduction of about 20% and significantly lower maintenance costs, while having same or lower price compared to conventional technology. As a result, over 20% lower heat price can be achieved together with long life cycle and low life cycle costs. The markets already offer large, mega-watt class, heat pumps, which use oil lubrication, require a lot of service, are large in size and use old technology. In the other hand, markets also offer solutions, which use new technology and are oil-free, but do not achieve mega-watt class in power. HT COMP aims to fill this gap in the market, developing a mega-watt class heat pump, which is oil and service free, and uses modern technology.

1.4 Research problem

There are numerous analytical and computational ways to calculate leakage of a labyrinth seal with a specific geometry and number of blades, but there is no extensive research on how much different variables in geometry or the number of blades affect the outcome.

Rotor dynamic analysis typically focuses on the rotor, bearings, and their interconnections. There is no research on the effect of different labyrinth seal geometries on rotor dynamics. In many cases, labyrinth seals are neglected from rotor dynamic analysis, because their effect is considered to be small. As the rotating machines get larger and more powerful, it is important to also note the small effects, which may become significant when the machines are scaled up. This work studies the relationship of different seal parameters to leakage and rotor dynamic stability.

To optimize a seal design in terms of reducing leakage and harmful vibration, a number of calculations with different variables have to be conducted to obtain data showing causal effect of different seal geometric variables to leakage and rotor dynamic stability.

1.5 Objectives

There are three objectives in this study. First objective is to provide results, which can act as a guide for a seal designer to focus on the most relevant variables, when optimizing design in terms of leakage and rotor stability. The second objective is to provide the best possible seal design as a combination of leakage, axial forces, and rotor dynamics for the HT COMP LUT research-to-business project. The third objective of this study is to provide new information about the effect of different seal parameters to rotor dynamics for the scientific community.

1.5.1 Research questions

There are three main subjects of research in this study, which formulates three main research questions with additional secondary questions:

- i. What are the most relevant seal variables including different geometrical dimensions, the number of blades and seal location to affect leakage?
 - How much do they affect individually?
 - Why they are the most relevant?
- ii. What are the most relevant seal variables to affect rotor instability?
 - How much do they affect individually?
 - Why they are they the most relevant?
- iii. What is the relationship between leakage caused by a radial labyrinth seal location and axial thrust in a radial compressor impeller?

1.5.2 Hypotheses

This thesis has two hypotheses:

- i. In a labyrinth seal, leakage optimization is contradictory to rotor instability (in axial seal case) and to axial forces (in radial seal case), meaning that the final design is a compromise between these factors.
- ii. Seal design variables, such as clearance and seal length, have greater impact on leakage and rotor instability than variables, such as blade width, blade height and chamber width. The impact of the least effective variables is negligible.

1.6 Scope

The scope of this thesis is in optimizing seals regarding leakage, rotor instability and axial thrust inside a framework of the HT COMP project. The base values are set by the boundaries of the project and are presented in chapter 3.1. The calculations are then constructed based on those values. No additional calculation is done for machines in different sizes, fluids, operational speeds, power, torque, shaft thickness, temperature, material, and so on. This means the results may differ for different machines and it is the reader's responsibility to interpret these results in a framework of one's own application and needs. The results can be very different if, for example, a different working fluid or temperature is used.

Only analytical and computational calculation methods are inside the scope of this work. Even though empirical testing would give the most accurate results, there is no possibility to conduct those.

1.7 Structure of thesis

The thesis is structured so, that after the introduction chapter, in chapter two, the methods for labyrinth seal leakage optimization and rotor dynamic analysis are presented. In chapter two, first are presented analytical methods for calculation of leakage of a seal. Several analytical leakage calculation methods, Matrin's, Kearson's, and Egli's methods are presented and later used to obtain results. Second, computational method for calculation of seal leakage, computational fluid dynamics (CFD) is presented. Third, two different methods, Black's and Child's methods, are presented for calculation of labyrinth seal dynamic coefficients. Fourth, two different methods, Alford's, and Wachel's methods, for calculation of impeller aerodynamic cross-coupled stiffness are presented. Fifth, rotor dynamic theory behind the analysis conducted

in preceding chapter is presented. Sixth, MATLAB-based toolbox for modelling rotor-bearing systems and analysing them is presented. Seventh, a method for calculating axial forces created by an impeller is presented. All methods presented in chapter 2, are used in obtaining results in the preceding chapter.

In chapter 3, the results are presented. First, a case study HT COMP is presented. All calculations are done using the input parameters derived from the case study. Several seal variables of seal geometry are selected as changing variables, and a number of setups is designed using a variety of combinations with different values. First are presented the results of leakage calculation using computational and analytical methods, and the effect of the variables to leakage and analysed. Second are presented the results for calculation of labyrinth seal dynamic coefficients using different seal parameters and the effect of the variables to the coefficients are analysed. Third are presented the results of calculation of impeller aerodynamic cross-coupled stiffness. Fourth, a rotor dynamic analysis is conducted using a MATLAB-based Rotor-Bearing Dynamics toolbox. The natural frequencies and damping ratios for different modes are calculated and presented in Campbell diagrams and damping ratio charts. Several analyses are made using different variables to further analyse the impact of change in those variables. Fifth are presented the results of radial seal placement on axial forces and leakage. The results are analysed using different values for seal radius.

In chapter 4, the results are analysed using a broad perspective. In chapter 5, the main findings are summarized, the research questions and hypotheses are answered, the impact of the research is discussed, and the possible future research and continuity is discussed.

2 Methods for optimization and analysis of labyrinth seal leakage and rotor dynamics

In this chapter methods for design and calculations are presented including respective theory behind those methods. These methods are for calculation of labyrinth seal leakage for axial and radial labyrinth seals, obtaining rotor dynamic coefficients for an axial labyrinth seal, rotor dynamic analysis for an axial labyrinth seal, calculation of aerodynamic stiffness caused by an impeller, and calculation of axial thrust caused by a radial labyrinth seal.

2.1 Analytical methods for leakage optimization

Labyrinth seal effectiveness is heavily related to its leakage; therefore, seal's effectiveness is usually viewed only from the leakage point of view. There are different ways to calculate leakage and several equations for different configurations. Leakage can be calculated with analytical equations or by using a Computational Fluid Dynamics (CFD) software. Most analytical methods ignore rotation of the seal, because of its complexity to include to the equations, but also because of its relatively small effect on the outcome. In analytical methods, a labyrinth seal is viewed as a consecutive series of circular gaps. (Cao 2017, p. 205.)

This thesis focuses on two configurations: axial and radial labyrinth seals for compressible gases. In this paper, rotation of seal is neglected. Three different analytical methods for calculating leakage flow are presented: Martin's method, Egli's method and Kearton's method. Egli's method is used only for axial seal, Kearton's method is used for only radial seal, and Martin's method is used for both. (Child's 2014, p. 593, 613.)

The first analytical method for estimating leakage flow through a labyrinth seal by simplifying gas dynamics was invented by Martin in 1908 and 1917. Martin makes two assumptions: 1. All kinetic energy is dissolved in a labyrinth chamber before the flow moves on to the next chamber, and 2. The actual flow area is the same as the theoretical flow area. Because of these assumptions, Martin's equation tends to overestimate the leakage flow. (Childs 2014, p. 591.). The mass flow, using Martin's method, is calculated as follows.

$$q_m = Ap_0 \sqrt{\frac{1-(p_n/p_0)^2}{RT_0[n-\ln(p_n/p_0)]}} \quad (1)$$

where q_m is mass flow, A is leakage area, p_0 and p_n are starting and ending pressures, R is the gas constant, T_0 is the starting temperature, and n is the number of blades.

Egli introduces a more accurate equation compared to Martin's equation. Egli's method is similar to Martin's method, but it is corrected with several specific coefficients to simulate real world more accurately. (Reunanen 1995, p. 15-16)

$$q_m = \varepsilon \alpha A \varphi_n \sqrt{\frac{p_0}{v_0}} \quad (2)$$

where ε is kinetic energy carryover coefficient, α is flow coefficient, φ is expansion factor for labyrinth seal, and v_0 is specific gravity of the gas.

Kinetic energy carryover coefficient ε is a corrective coefficient, which is used when the labyrinth seal is not ideal, meaning the dynamic pressure is not dissolved in each labyrinth chambers. The kinetic energy carryover coefficient accounts for some dynamic pressure not dissolved in a labyrinth chamber. In an ideal seal, where all dynamic pressure dissolves in each chamber, the kinetic energy carryover coefficient is 1, meaning it can be neglected. A full labyrinth seal is close to ideal, whereas a half labyrinth usually gets a kinetic energy carryover coefficient value of 2-3. (Childs 2014, p. 597.) The kinetic energy carryover coefficient can be calculated as follows.

$$\varepsilon = \sqrt{\frac{n/(n-1)}{\left(\frac{n}{n-1}\right) - \left[\frac{c/B}{\left(\frac{c}{B}\right) + 0.02}\right]}} \quad (3)$$

where ε is kinetic energy carryover coefficient, n is the number of blades, c is the seal clearance, and B is the chamber width.

Flow coefficient α is a corrective coefficient, which is the relation between the real and theoretical flow. It includes friction's effect on flow. Flow coefficient is usually considered to be equal for every blade. Flow coefficient can be obtained from Figure 8, which contains a lot of measurement data from different seal geometries and gases. Flow coefficient can be obtained from the figure from the cross-section of the correct line and Reynold's number. Correct line is picked or estimated by the relation of seal clearance c and blade width t . (Childs 2014, p. 600.)

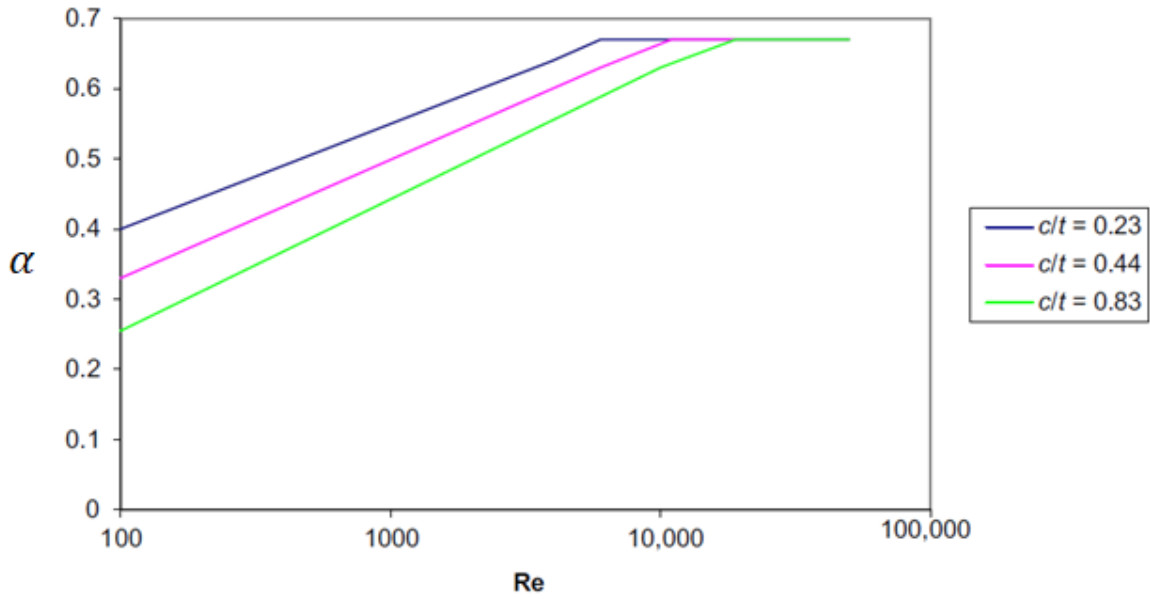


Figure 8. Flow coefficient is obtained from the cross-section of correct line and Reynold's number. (Childs 2014, p. 600, figure modified)

Setting flow coefficient is an iterative process, where Reynold's number is first initiated and iterated later. Initial flow coefficient is obtained using an estimated Reynold's number. After initial mass flow is calculated, more accurate Reynold's number can be calculated from the following equation. (Childs 2014, p. 599-600.)

$$Re = \frac{\rho u_{mean} D_h}{\mu} = \frac{\rho q_m 2c}{\mu A \rho} = \frac{q_m 2c}{\mu \pi d c} = \frac{2 q_m}{\mu \pi 2r} \quad (4)$$

where μ is kinematic viscosity of gas and r is seal radius. Once iterated flow coefficient is obtained using once iterated Reynold's number, and once iterated mass flow can be calculated using equation 2. Iterations are done as many times as a more accurate flow coefficient can be obtained from figure 8. (Childs 2014, p. 599-600.) The accuracy, in terms of number of iterations, is defined by the designer.

In a labyrinth seal, mass flow over each labyrinth chamber is the same, but volume flow increases as the gas expands when losing pressure. Expansion factor ϕ is needed for a seal with multiple cavities. In Egli's method, the expansion factor can be calculated with enough accuracy, if the pressure ratio between adjacent chambers is greater than 0.8. (Reunanen 1995, p. 15–16.) Expansion factor can be calculated using the following equation.

$$\varphi_n = \sqrt{\frac{1-(p_n/p_0)^2}{n+\ln(p_0/p_n)}} \quad (5)$$

For radial labyrinth seal calculations, Kearton's method is used. Kearton's equation was introduced first time in 1952 and it works with radial seals flowing both ways and with compressible gases. Like in Martin's method, also in Kearton's method it is assumed that all kinetic energy dissolves in each labyrinth seal chamber. But unlike Martin's second assumption about theoretical flow area being the same as actual flow area, in Kearton's method, this is considered using a discharge coefficient, which is always < 1 . The equation is valid only if the flow does not reach speed of sound in the last discharge point. (Childs 2014, p. 613; Reunanen 1995, p. 17.). The mass flow using Kearton's method is calculated as follows.

$$q_m = C_d A_1 \sqrt{\frac{F(p_0^2 - p_n^2)}{RT_0 \phi_n}} \quad (6)$$

where C_d is discharge coefficient, A_1 is the flow area, F is a function of pressure ratio, p_0 and p_n are starting and ending pressures, R is the gas constant, T_0 is the starting temperature and ϕ_n is total area factor. The flow area A_1 is calculated using the following equation. (Reunanen 1995, p. 17.)

$$A_1 = 2\pi r h \quad (7)$$

A significant difference between a radial seal and an axial seal is that in radial seal, the discharge area is not constant, but either increases or decreases in the flow direction. Because of that, total area factor ϕ_n is used to include that information into the equation. In radial seal, flow direction can be inwards or outwards. The difference is the sign after n . If the flow is outwards, minus sign is to be used and if the flow is inwards, + sign is to be used after n . (Reunanen 1995, p. 17–18.)

$$\phi_n = n \pm \frac{2(B-t)n(n-1)}{2r+(B+t)(2n-1)} \quad (8)$$

F is a dimensionless pressure difference correction factor, that can be taken from Table 2.

Table 2. Dimensionless pressure difference correction factor F . (Reunanen 1995, p. 17)

p_1/p_0	F
1.00	1.00
0.95	0.95116
0.90	0.90425
0.85	0.85872
0.80	0.81400

Discharge coefficient C_d is virtually same as flow coefficient α . Figure 8 can be used to set discharge coefficient the same way flow coefficient is set in Egli's method. Reynold's number is first assumed, and discharge coefficient is picked from Figure 8. Mass flow is then calculated and iterated for obtaining a more accurate Reynold's number using equation 4. This process is continued for as long as no more accurate discharge coefficient can be obtained.

2.2 Computational methods for leakage optimization

In this thesis work, CFD – Computational Fluid Dynamics tool is used to obtain results together with analytical methods. CFD is a finite element-based method to calculate fluid flow. CFD tools are used to simulate and predict fluid flow and aerodynamic behavior in complex structures, that would be overly laborious for hand calculations. CFD tools utilize numerical methods and algorithms in solving partial differential equations to solve problems. CFD environment can consist of dynamic movement of liquids or gases, surfaces defined by boundary conditions, and their interactions. (Zoll 2009, p. 4; Wang 2010, p. 180-181.)

In CFD, a complex structure can be divided into a number of small cells, which together form a mesh. After the mesh is formed, either Euler or Navier-Stokes equation is applied to every element of the mesh to calculate the fluid flow and their behavior in interaction with defined boundaries. CFD calculations typically involve a lot of computational power, since the solutions to sometimes highly complex problems involve highly non-linear equations

with multiple degrees of freedom. The need for computational power depends on the accuracy of the mesh. (Zoll 2009, p. 4.; Wang 2010, p. 180–181.)

2.3 Dynamic coefficients for an axial seal

Axial labyrinth seal's effect on rotor dynamics is often neglected due to the assumption that it's effect would be minor. This chapter presents how different seal shapes and seal lengths affect rotor dynamics in general. First, rotor dynamic coefficients are obtained, and then Rotor-Bearing Dynamics toolbox is used to analyse how different seal parameters affect natural frequencies and damping ratios of the system.

Rotating systems have parts or elements that can be generally divided into three groups based on how they are reviewed in terms of rotor dynamics: 1. rotating parts, such as shafts and discs, 2. stationary supporting parts, such as casings or housings and 3. different kinds of interconnective parts, such as bearings, damping elements, and seals, which create physical links and forces between different elements in the system. In rotor dynamic review, most of these interconnective components can be simplified and represented as spring and dampers. This chapter presents different calculation methods for rotor dynamic coefficients of axial labyrinth seals, which can be reviewed as liquid annular seals. (Chen 2005, p. 191.)

All rotor-bearing systems result some amount of rotor vibration and harmonic displacement of the shaft. The pressure reduction caused by the labyrinth seal creates a considerable radial restoring force to the opposite direction of the shaft displacement, which is called as the *Lomakin effect* as presented in Figure 9. (Chen 2005, p. 191.)

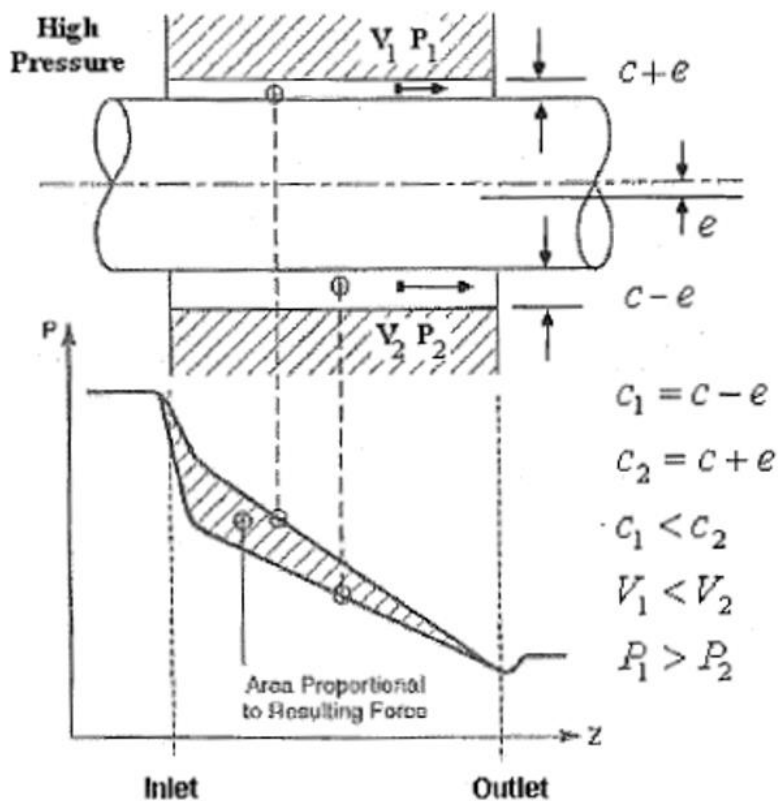


Figure 9. *The Lomakin effect.* (Chen 2005, p. 191, figure modified)

In figure 9, e is the radial displacement of the shaft from the center and c is the seal clearance, when the shaft is centered. As the shaft vibrates, the clearance in the direction of the shaft displacement is $c - e$, i.e., the clearance gets smaller, and in the opposite direction, $c + e$, i.e., the clearance gets larger. The pressure of the flow reduces as its velocity increases when the flow travels through an axial labyrinth seal. This is called *the Bernoulli effect*. Because of this effect and the cyclical displacement of the shaft, in the side of the shaft where the clearance is larger, the pressure is lower, and the velocity is higher than on the side where the clearance is smaller. Also, an additional entrance loss happens at the entrance of the seal creating even larger local pressure and unbalance force. After the entrance phase, the pressure reduction in the seal is almost linear. These non-symmetric pressure distributions create restoring forces opposite to the shaft displacement. (Chen 2005, p. 297.)

Because of the *Lomakin effect*, axial labyrinth seal effects rotor dynamic stability. With radial labyrinth seals, the force it creates is perpendicular to axial seals. Therefore, radial seals do not directly affect rotor dynamic stability, but instead create an axial force. Axial forces are taken into account in a separate axial force review together with bearings and their

axial load capabilities. For this reason, only axial labyrinth seals and their rotor dynamic effects are studied in this chapter.

There are several methods derived from *the Lomakin effect* to develop rotor dynamic coefficients for an axial labyrinth seal. In this study, two methods are presented: Black and Jenssen's method developed in 1970 and Child's method developed first in 1983 and extended further in 1993. (Chen 2005, p. 298.) The presented methods are analytical methods in obtaining rotor dynamic coefficients. More accurate results are obtained by empirical real-life test. When applying the results to design work, a tolerance of $\pm 30\%$ is recommended (Chen 2005, p. 304.).

The linearized forces caused by the axial labyrinth seal acting on the rotor are presented in the following equation. (Chen 2005, p. 298)

$$\begin{Bmatrix} F_x \\ F_y \end{Bmatrix} = - \begin{bmatrix} K_d & k_c \\ -k_c & K_d \end{bmatrix} \begin{Bmatrix} x \\ y \end{Bmatrix} - \begin{bmatrix} C_d & c_c \\ -c_c & C_d \end{bmatrix} \begin{Bmatrix} \dot{x} \\ \dot{y} \end{Bmatrix} - \begin{bmatrix} m_d & 0 \\ 0 & m_d \end{bmatrix} \begin{Bmatrix} \ddot{x} \\ \ddot{y} \end{Bmatrix} \quad (9)$$

where F_x and F_y are forces, x and y are displacements, \dot{x} and \dot{y} are velocities, \ddot{x} and \ddot{y} are accelerations, K_d is direct stiffness, k_c is cross coupled stiffness, C_d is direct damping, c_c is cross coupled damping and m_d is principal inertia coefficient. (Chen 2005, p. 298)

The total axial pressure drop ΔP and the mean axial flow velocity w , in m/s, are related as described in Equation below. The mean axial flow velocity is usually unknown in early design phase, but the total pressure drop between the high-pressure and the low-pressure sides of the seal is usually known. This pressure difference is a prerequisite for calculating the dynamic coefficients for an axial seal. Mean axial flow velocity is therefore defined by iterating it so, that the given value gives a total axial pressure drop ΔP a value that equals to the known pressure difference between the high-pressure and low-pressure sides of the seal. (Chen 2005, p. 298.)

$$\Delta P = \frac{1}{2}(1 + \zeta + 2\sigma)\rho w^2 \quad (10)$$

where ζ is the entrance loss coefficient (typically 0.1), ρ is the fluid density in kg/m^3 , and

$$\sigma = \lambda \frac{L}{c} \quad (11)$$

where L is the length of the seal in meters, c is the seal clearance in meters, and λ is the friction loss factor. λ is defined differently in Black's and Child's methods. In both methods,

σ is a nonlinear function of the mean axial velocity w , which therefore must be determined iteratively. The correct mean axial velocity w is found iteratively by giving it a value, which results in ΔP being the same as the actual pressure reduction caused by the seal. (Chen 2005, p. 298.)

The fluid's circumferential velocity when entering the seal is expressed as a fraction of the shafts surface speed ($R\Omega$). (Chen 2005, p. 298)

$$u_c = \alpha R\Omega \quad (12)$$

where Ω is rotational speed, r is the seal radius and α is the inlet swirl ratio. In Black's method, the inlet swirl ratio is always 0.5. In child's model, the inlet swirl ratio can be changed. The inlet swirl has a relatively large impact on cross coupled stiffness, so by reducing it, stability can be significantly increased. (Chen 2005, p. 298–299.)

Black's method.

The equations to solve dynamic coefficients for axial labyrinth seal using Black and Jenssen's (1970) method are presented here. (Chen 2005, p. 299-300)

$$K_d = \mu_3(\mu_0 - 0.25\mu_2\Omega^2T^2) \quad (13)$$

$$k_c = \mu_3(0.5\mu_1\Omega T) \quad (14)$$

$$C_d = \mu_3\mu_1T \quad (15)$$

$$c_c = \mu_3\mu_2\Omega T^2 \quad (16)$$

$$m_d = \mu_3\mu_2T^2 \quad (17)$$

where

$$\mu_0 = \frac{(1+\zeta)\sigma^2}{(1+\zeta+2\sigma)^2} \quad (18)$$

$$\mu_1 = \frac{(1+\zeta)^2\sigma + (1+\zeta)(2.33+2\zeta)\sigma^2 + 3.33(1+\zeta)\sigma^3 + 1.33\sigma^4}{(1+\zeta+2\sigma)^3} \quad (19)$$

$$\mu_2 = \frac{0.33(1+\zeta)^2(2\zeta-1)\sigma + (1+\zeta)(1+2\zeta)\sigma^2 + 2(1+\zeta)\sigma^3 + 1.33\sigma^4}{(1+\zeta+2\sigma)^4} \quad (20)$$

$$\mu_3 = \frac{\pi r \Delta P}{\lambda} \quad (21)$$

$$\lambda = 0.079 R_a^{-0.25} \left[1 + \left(\frac{7R_c}{8R_a} \right)^2 \right]^{0.375} \quad (22)$$

$$R_a = \frac{2\rho w c}{\mu} \quad (23)$$

$$R_c = \frac{\rho r \Omega c}{\mu} \quad (24)$$

$$T = \frac{L}{w} \quad (25)$$

where R_a is axial and R_c is circumferential Reynold's number, μ is fluid viscosity. μ_0, μ_1, μ_2 are used in a simplified case of a short seal solution. Short seal solution tends to overestimate the dynamic coefficients. To get more accurate results for a finite length seal, the following corrected parameters should be used. (Chen 2005, p. 300.)

$$\mu_{0,c} = \frac{\mu_0}{1+0.28(L/r)^2} \quad (26)$$

$$\mu_{1,c} = \frac{\mu_1}{1+0.23(L/r)^2} \quad (27)$$

$$\mu_{2,c} = \frac{\mu_2}{1+0.06(L/r)^2} \quad (28)$$

Child's method.

The equations to solve dynamic coefficients for axial labyrinth seal using Child's (1983) method are presented here. The method is based on Hirs' lubrication equation. Fluid inertia terms and inlet swirl are included. These equations use short seal theory. (Chen 2005, p. 301–302.)

$$K_d = \left(\frac{\pi r \Delta P}{\lambda} \right) \frac{2\sigma^2}{(1+\zeta+2\sigma)} \left\{ 1.25E - \frac{(\Omega T)^2}{4\sigma} \left\{ \frac{1}{2} \left(\frac{1}{6} + E \right) + \frac{2w_0}{a} \left[\left(E + \frac{1}{a^2} \right) (1 - e^{-a}) - \left(\frac{1}{2} + \frac{1}{a} \right) e^{-a} \right] \right\} \right\} \quad (29)$$

$$k_c = \left(\frac{\pi r \Delta P}{\lambda} \right) \frac{\sigma^2 \Omega T}{(1+\zeta+2\sigma)} \left\{ \frac{E}{\sigma} + \frac{Y}{2} \left(\frac{1}{6} + E \right) + \frac{2w_0}{a} \left\{ AY + \left(\frac{1}{\sigma} - \frac{Y}{a} \right) \left[(1 - e^{-a}) \left(E + \frac{1}{2} + \frac{1}{a} \right) - 1 \right] \right\} \right\} \quad (30)$$

$$C_d = \left(\frac{\pi r \Delta P}{\lambda} \right) \frac{2\sigma^2}{(1+\zeta+2\sigma)} \left[\frac{E}{\sigma} + \frac{Y}{2} \left(\frac{1}{6} + E \right) \right] \quad (31)$$

$$c_c = \left(\frac{\pi r \Delta P}{\lambda} \right) \frac{\sigma^2 \Omega T}{(1+\zeta+2\sigma)} \left\{ \frac{1}{2} \left(\frac{1}{6} + E \right) + \frac{w_0}{a} \left[(1 - e^{-a}) \left(E + \frac{1}{2} + \frac{1}{a^2} \right) - \left(\frac{1}{2} + \frac{e^{-a}}{a} \right) \right] \right\} \quad (32)$$

$$m_d = \left(\frac{\pi r \Delta P}{\lambda} \right) \frac{\sigma \left(\frac{1}{6} + E \right)}{(1+\zeta+2\sigma)} \quad (33)$$

where e is Euler's number and

$$\lambda = 0.066 R_a^{-0.25} \left[1 + \frac{1}{4y^2} \right]^{0.375} \quad (34)$$

$$R_a = \frac{\rho w c}{\mu} \quad (35)$$

$$R_c = \frac{\rho r \Omega c}{\mu} \quad (36)$$

$$y = \frac{R_a}{R_c} = \frac{w}{r \Omega} \quad (37)$$

$$a = \sigma(1 + 0.75\beta) \quad (38)$$

$$\beta = \frac{1}{1+4y^2} \quad (39)$$

$$Y = 1 + 4y^2\beta(0.75) \quad (40)$$

$$E = \frac{(1+\zeta)}{2(1+\zeta+Y\sigma)} \quad (41)$$

$$T = \frac{L}{v} \quad (42)$$

where R_a is axial, and R_c is circumferential Reynold's number.

2.4 Aerodynamic cross-coupled stiffness caused by an impeller

The shaft of a rotor-bearing system always has some vibration. As a result, also the attached impeller tilts cyclically creating variation in the space between the impeller and the casing or other stationary component. This aerodynamic excitation can be described as follows. (Chen 2005, p. 305.)

$$\begin{Bmatrix} F_x \\ F_y \end{Bmatrix} = - \begin{bmatrix} 0 & K_{xy} \\ K_{yx} & 0 \end{bmatrix} \begin{Bmatrix} x \\ y \end{Bmatrix} \quad (43)$$

Chen (2005) presents two different analytical methods: Alford (1965) and Wachel (1983) methods. Alford's method tends to underestimate the reality, whereas Wachel's method tends to overestimate it. Because of this, Alford's equation gives a lower limit and Wachel's equation gives an upper limit for the coefficient and the real value is thought to be somewhere in the middle of these two results. (Chen 2005, p. 305.)

Alford's equation: (Chen 2005, p. 305)

$$K_{xy} = -K_{yx} = \frac{\beta T}{DH} \quad (44)$$

where K_{xy} is the cross coupled stiffness, T is stage torque, D is mean impeller blade pitch, H is impeller blade height, and β is efficiency factor. Alford's method was originally designed for axial flow turbines and compressors, but using efficiency factor, it can be extended for centrifugal compressors as well. Different efficiency factors for different types of rotating machines: $\beta = 0.5$ for shrouded axially bladed discs, $\beta = 1.5$ for un-shrouded axially bladed wings, $\beta = 2-3$ for un-shrouded radial flow impellers and $\beta = 5-10$ for extreme cases, such as overhung impellers. (Chen 2005, p. 305.)

Wachel's equation: (Chen 2005, p. 306)

$$K_{xy} = -K_{yx} = \frac{6300 \text{ hp } Mw}{D_i H_i \text{ Rpm}} \cdot \frac{\rho_d}{\rho_s} \quad (45)$$

where hp is power in horse powers, Mw is the molecular weight of the fluid, D_i is the mean impeller blade pitch in inches, H_i is the impeller blade height, ρ_d is the density of the fluid at discharge and ρ_s is the fluid density at suction.

2.5 Rotor dynamic theory

Rotor dynamics is a branch of mechanical vibration theory with an emphasis on rotating systems and phenomena. The system's natural frequencies are speed dependent in rotor dynamics, because of gyroscopic effect. The dynamic properties of bearings and seals are also speed dependent. Rotors always have some unbalance, which cause excitation in the system, which result as vibration. Vibration response amplitudes are magnified when rotation speed is close to natural frequencies of the system. These critical speeds should be avoided in operation to minimize harmful vibration.

Every rotating object has some amount of gyroscopic effect. Gyroscopic motion can be defined as the tendency of the rotating object to keep its orientation of rotation. It has to be taken into account, when describing and analysing rotor dynamic systems, because it affects the natural frequencies. (Usabamatov 2020, p. 1.) Gyroscopic moment is the rate of change of angular momentum. Its effect is perpendicular to the change of orientation of the rotating axis. Gyroscopic momentum can be described as follows.

$$M_G = I_P \Omega \dot{\theta} \quad (46)$$

where I_P is the polar mass moment of inertia of the flywheel and $\dot{\theta}$ is the angular velocity change of orientation of the rotation axis.

In rotor dynamic analysis, equations of motion are derived, and state-space approach is used for solving damped eigenvalue problem to get natural frequencies. The whole system can be described by matrices in finite element method. The equation of motion is as follows. (Chen 2005, p. 124.)

$$\mathbf{M}\ddot{\mathbf{q}} + (\mathbf{C} + \Omega\mathbf{G})\dot{\mathbf{q}} + \mathbf{K}\mathbf{q} = \mathbf{F}(t) \quad (47)$$

where \mathbf{M} is the mass matrix, \mathbf{C} is the damping matrix, \mathbf{G} is the gyroscopic matrix, \mathbf{K} is the stiffness matrix, $\ddot{\mathbf{q}}$ is acceleration, $\dot{\mathbf{q}}$ is velocity, \mathbf{q} is displacement, \mathbf{F} is the time dependent external force, and Ω is the shaft angular velocity. (Sopanen 2019, p. 31)

Damping matrix \mathbf{C} can be obtained for example by using proportional damping (also known as Rayleigh's damping). In order to calculate the damping matrix using Rayleigh's damping, damping ratios and their respective natural frequencies are known. Constants α and β can be obtained by solving the following system of equations.

$$2\zeta_1\omega_1 = \alpha + \beta\omega_1^2$$

$$2\zeta_2\omega_2 = \alpha + \beta\omega_2^2 \quad (48)$$

where ζ is the damping ratio, ω is the natural frequency, and α and β are the constants to be solved. After solving the constants, the damping ratio C can be solved from the following equation.

$$C = \alpha\mathbf{M} + \beta\mathbf{K} \quad (49)$$

In rotor dynamics, different elements of the system are described in specific mathematical equations. Rigid discs, for example impellers, gear wheels, and other discs, contribute to the mass and gyroscopic matrices in their special location. Rigid discs contribute to mass and gyroscopic matrices of the system, which are derived by the principles of kinetic energy. In Rotor-Bearing Dynamics toolbox, rotor rotates around x-axis. Assuming the rotational axis of the rigid disc coincides with the x-axis of the shaft, the kinetic energy equation can be described as follows. (Chen 2005, p. 120; Sopanen 2019, p 7.)

$$T = \frac{1}{2}m_d(\dot{x}^2 + \dot{y}^2 + \dot{z}^2) + \frac{1}{2}I_P\Omega^2 + \frac{1}{2}I_d(\dot{\theta}_y^2 + \dot{\theta}_z^2) + \frac{1}{2}\Omega I_P(\dot{\theta}_y\theta_z - \theta_y\dot{\theta}_z) \quad (50)$$

where m_d is disc mass, x , y , and z are displacements, θ is rotational displacement, $\dot{\theta}$ is rotational velocity, I_d is diametral mass moment of inertia, and I_P is the polar moment of inertia. The kinetic energy equation can be also written in matrix form as follows. (Chen 2005, p. 120; Sopanen 2019, p. 7)

$$T = \frac{1}{2}\dot{\mathbf{q}}^T\mathbf{M}_d\dot{\mathbf{q}} + \mathbf{q}^T\Omega\mathbf{g}_d\dot{\mathbf{q}} \quad (51)$$

where $\mathbf{q}^T(t) = (x, y, \theta_x, \theta_y)$ is the displacement vector of the specific node. The mass and gyroscopic matrices of a rigid disc take the following forms. (Chen 2005, p. 120)

$$\mathbf{M}^d = \begin{bmatrix} m_d & 0 & 0 & 0 \\ 0 & m_d & 0 & 0 \\ 0 & 0 & 0 & 0 \\ 0 & 0 & 0 & 0 \end{bmatrix} \quad \mathbf{G}^d = \begin{bmatrix} 0 & 0 & 0 & 0 \\ 0 & 0 & 0 & 0 \\ 0 & 0 & 0 & I_P \\ 0 & 0 & -I_P & 0 \end{bmatrix} \quad (52)$$

Rotating beam elements are other important elements in describing rotor-bearing systems. Beams are modelled using nodes in both ends of the beam. Each node has four degrees of freedom, two translational and two rotational. Therefore, a single element beam has total of eight degrees of freedom, before beam-type dependent constraints are applied. Matrices can

be formed with a help of shape functions N_T and N_R . For example, translational mass matrix, rotational inertia matrix, gyroscopic matrix, bending stiffness matrix and shear stiffness matrix can be formed from finite element derivation using their specific equations.

After forming the matrices, natural frequencies can be obtained by solving the damped eigenvalue problem. In order to solve the damped eigenvalue problem, a state-space format needs to be used. Original equation of motion is multiplied by \mathbf{M}^{-1} , and the equation of motion takes the following 2n-by2n matrix form.

$$\mathbf{A} = \begin{bmatrix} \mathbf{0} & \mathbf{I} \\ -\mathbf{M}^{-1}\mathbf{K} & -\mathbf{M}^{-1}(\mathbf{C} + \Omega\mathbf{G}) \end{bmatrix} \quad (53)$$

where \mathbf{A} is the state-space matrix. The eigenvalue problem is then described in following form.

$$\mathbf{A}\mathbf{z} = \lambda\mathbf{z} \quad (54)$$

where λ is the eigenvalue and \mathbf{z} is the eigenvector. The eigenvalues are in complex conjugate pairs as follows.

$$\begin{aligned} \lambda &= \alpha_i + j\beta_i & \bar{\lambda} &= \alpha_i - j\beta_i \\ \mathbf{z}_i &= \begin{bmatrix} \mathbf{u}_i \\ \lambda_i \mathbf{u}_i \end{bmatrix} & \bar{\mathbf{z}}_i &= \begin{bmatrix} \bar{\mathbf{u}}_i \\ \bar{\lambda}_i \bar{\mathbf{u}}_i \end{bmatrix} \end{aligned} \quad (55)$$

where \mathbf{z} and $\bar{\mathbf{z}}$ are the eigenvectors, α is the real part, β_i is the imaginary part, and \mathbf{u}_i is the mode shape. The imaginary part β_i is the damped natural frequency. The eigenvectors contain information about the whirling mode shapes of the rotor. The damping ratio ζ of mode i can be described as follows.

$$\zeta_i = \frac{-\alpha_i}{\sqrt{\alpha_i^2 + \beta_i^2}} \quad (56)$$

Solution to damped eigenvalue problem is used to obtain natural frequencies and whirling modes of the system. There can be either forward or backward whirling in a mode. Forward whirling means that the center point of the rotor rotates in the same direction as the rotor rotates around its own axis. In backward whirling, the rotation of the center of the shaft rotates in the opposite direction compared to the rotation of the shaft around its own axis.

Since there are always unbalances in rotor dynamic systems, it is important to include unbalance responses into the analysis. Unbalance is defined by the unbalance mass times radius and the phase angle of its location. It can be written as follows.

$$\begin{bmatrix} F_x \\ F_y \end{bmatrix} = m_u r \Omega^2 \begin{bmatrix} \cos(\Omega t + \alpha) \\ \sin(\Omega t + \alpha) \end{bmatrix} \quad (57)$$

where m_u is the unbalance mass, r is the radius of its location, and α is the phase angle of its location. Unbalance masses are described as force vectors for node i as follows.

$$\begin{aligned} f_s^i &= m_u r \Omega^2 [-\sin \alpha \cos \alpha \ 0 \ 0]^T \\ f_c^i &= m_u r \Omega^2 [\cos \alpha \sin \alpha \ 0 \ 0]^T \end{aligned} \quad (58)$$

The force vectors can then be written for a system of n number of nodes as follows.

$$\mathbf{F}_s = [f_s^{i^T} \dots f_s^{n^T}]^T \quad \mathbf{F}_c = [f_c^{i^T} \dots f_c^{n^T}]^T \quad (59)$$

Equation of motion then takes the following form.

$$\mathbf{M}\ddot{\mathbf{q}} + (\mathbf{C} + \Omega\mathbf{G})\dot{\mathbf{q}} + \mathbf{K}\mathbf{q} = \mathbf{F}_s \sin \Omega t + \mathbf{F}_c \sin \Omega t \quad (60)$$

And in matrix form.

$$\begin{bmatrix} \mathbf{K} - \mathbf{M}\Omega^2 & -\Omega(\mathbf{C} + \Omega\mathbf{G}) \\ \Omega(\mathbf{C} + \Omega\mathbf{G}) & \mathbf{K} - \mathbf{M}\Omega^2 \end{bmatrix} \begin{bmatrix} \mathbf{p}_s \\ \mathbf{p}_c \end{bmatrix} = \begin{bmatrix} \mathbf{F}_s \\ \mathbf{F}_c \end{bmatrix} \quad (61)$$

After solving all needed calculations, the system can be analysed. Correct interpretation and analysis of the results is the most important part when studying rotor dynamic behaviour of rotor-bearing systems. Natural frequencies, critical speeds and whirling modes have to be interpreted correctly in order to proceed safely avoiding harmful resonance. Also, it is important to know what changes should be made to the system, in case of harmful resonance. Campbell diagram is one of the most informative tools in analysing the systems natural frequencies, and their behaviour at different rotational speeds. In Campbell diagram, natural frequencies and excitation frequencies are plotted as a function of rotation speed. From the Campbell diagram, whirling modes and critical speeds can be obtained. Campbell diagram is presented in Figure 10.

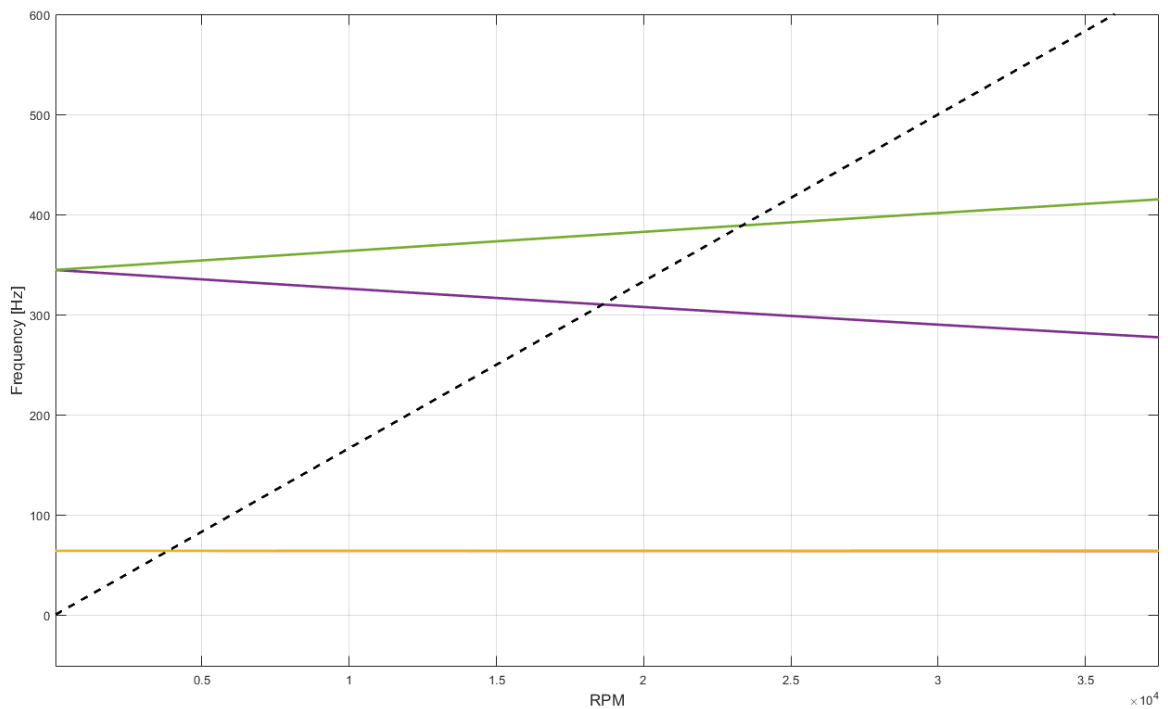


Figure 10. Campbell diagram.

In the Campbell figure, the vertical axis is the frequency of natural frequencies in Hz, and the horizontal axis is the rotation speed of the rotor in revolutions per minute. The dotted line is a linear increase of rpm and frequency. In every point of the dotted line, the x value and the y value are the same, if converted to the same unit. The coloured lines are the natural frequencies, or the modes, of the system. As the rotation speed increases, the lines start to deviate from each other. The higher the rotation speed, the greater the difference between the lines. This happens, because of the gyroscopic effect. The green line in the figure is a mode, and because it is ascending as the rotational speed increases, it is a forward whirling mode. Respectively, the purple line descends as the rotational speed increases, and therefore it is a backward whirling mode. The critical speeds are the values of x-axis, where the natural frequencies coincide with the dotted line. In this example, the critical speeds would therefore be approximately 3900, 18500, and 23500 rpm.

2.6 Rotor-Bearing Dynamics toolbox

Rotor-Bearing Dynamics is a code package used in MATLAB environment for vibration analysis of rotor-bearing systems. It was first created by professor Jussi Sopanen, and later developed further in Machine Dynamics laboratory in LUT by several doctoral and master's level students for research and educational needs. In Rotor-Bearing dynamics, a rotor-bearing system, including the rotor, bearings, discs, impellers, spring-damper elements, and other needed components, is first modelled using a finite element approach. After the modelling phase, the system can be analysed by for example free-free natural frequencies, damping ratios and mode shapes, rotation speed dependent natural frequencies and damping ratios, mode shapes of a rotating rotor at specified speed, limit speed for rotor dynamic instability, harmonic steady state responses due to unbalance forces, and ball bearings and hydrodynamic journal bearing coefficients. (Sopanen 2019, p. 5.)

With the toolbox, it is possible to calculate stiffness and damping coefficients for ball and journal bearings. Axial labyrinth seals can also be included in the toolbox by adding direct and cross-coupled stiffness and damping to the corresponding nodes at their designated axial location in the assembly. The values are then transferred to global stiffness and damping matrices of the whole system. Labyrinth seals are not modelled in the visual representation of the system. The toolbox automatically includes gyroscopic effects into analyses. (Sopanen 2019, p. 5.)

2.7 Calculation of axial forces caused by an impeller

The radial location of a radial labyrinth seal in a back side of an impeller in a centrifugal pump affects the amount of axial thrust force created by the pressure between the impeller back side and the stationary back disc. It can be assumed that the larger the high-pressure volume between the impeller back side and the back disc, the greater axial force is created. Therefore, the closer the seal is to the shaft centre, the more force is created. Newton's second law can be used to estimate the axial thrust. For that, reliable calculation of pressure distribution in the back side of the impeller is needed. (Tiainen, 2021.)

Axial thrust can be estimated using empirical, computational, or analytical methods. This chapter presents an analytical method introduced by Larjola together with a hybrid method

introduced in Tiainen's study. These methods are used to obtain results. The total axial thrust created by the impeller can be estimated using the following equation. (Tiainen 2021, p. 3.)

$$F_{total} = F_{inlet} + F_{shroud} + F_{impulse} - F_{back\ disk} \quad (62)$$

This chapter focuses only on the force created between the impeller back side and the back disc, and therefore only that force is examined. This force can be estimated using the following equation, where the pressure is a function of diameter. (Tiainen 2021, p. 3.)

$$F_{back\ disk} = p_2 \frac{\pi}{4} (d_2^2 - d_0^2) \quad (63)$$

where p is the pressure, and d is the diameter. The subscript 0 refers to the shaft, 2 refers to the impeller outlet. In Larjola's method, the distribution of pressure is presented as function of r . When calculating the distribution of pressure, it is presumed that the working fluid is balanced radially ensuring that the forces created by pressure balance the centrifugal forces. (Tiainen 2021, p. 14.)

$$d\rho = \rho(f\omega)^2 r dr \quad (64)$$

where fraction f is 0.5. In order to obtain the distribution of pressure on the back disc, an adequate amount of datapoints between seal radius r_L and impeller outlet radius r_2 is needed. The pressure for individual datapoint is obtained as follows. (Tiainen 2021, p. 15)

$$\rho = \rho_2 \left[\frac{\gamma-1}{2\gamma\rho_2} \rho_2 f^2 \omega^2 (r_L^2 - r_2^2) + 1 \right]^{\left(\frac{\gamma}{\gamma-1}\right)} \quad (65)$$

where γ is the ratio of specific heats of inlet and outlet, ω is the angular velocity. The force $F_{back\ disk}$ created by the pressure distribution is added into every datapoint between the seal radius and impeller outlet radius. The force affecting to the back disc in centrifugal compressor or pump case can be expressed as follows. (Tiainen 2021, p. 15.)

$$F_{back\ disk} = \rho_{amb} \pi r_0^2 + \left(\frac{\rho_{amb} + \rho_{r_L}}{2} \right) \pi (r_L^2 - r_0^2) + \int_{r_L}^{r_2} \rho \cdot 2\pi r dr \quad (66)$$

where r_L is the outer radius of the seal.

3 Results

In this chapter, the methods described in the last chapter are applied to calculation of leakage, rotor dynamic coefficients of axial seals, impeller aerodynamic stiffness, axial forces, and rotor dynamic analysis in the HT COMP project. Actual HT COMP compressor dimensions are used, but instead of refrigerant used in the project, air is used in this thesis work. Therefore, the results do not directly apply to the project. The case study with starting dimensions is first presented. After that, labyrinth seal leakage calculations for both axial and radial seals, dynamic coefficients for an axial seal, aerodynamic cross-coupled stiffness by an impeller, rotor dynamic analysis, and effect of radial seal placement on axial forces, are presented.

3.1 Case study

The labyrinth seal is used either as an axial seal between the rotor shaft and the stator, or as a radial seal between the impeller back side and the stationary back disc. Both configurations are calculated in this thesis work. Some dimensions and values, such as the shaft diameter, impeller size, and rotation speed of the initial model, set boundaries for the dimensions of the seal design. For example, for radial seal, the impeller back plate diameter gives maximum and minimum values for the placement of the seal. The base values are set to mid-point of these boundaries. For variables, such as blade number or chamber width, the base values are obtained by studying a number of existing seal designs and coming estimating an average or a most common value. The calculations are then constructed so that the base value acts as an average and the calculation are done using both increased and decreased values from the base value.

For radial seal the base values are set to be the following:

- Seal radius r is 100 mm
- Clearance h is 0.5 mm
- Blade height is 2.2 mm

- Chamber width B is 3 mm
- Number of blades n is 10
- Shape: 35° inclined, which gives blade width b is 0.77 mm

Base setups for axial and radial seals are presented in Figures 11 and 12.

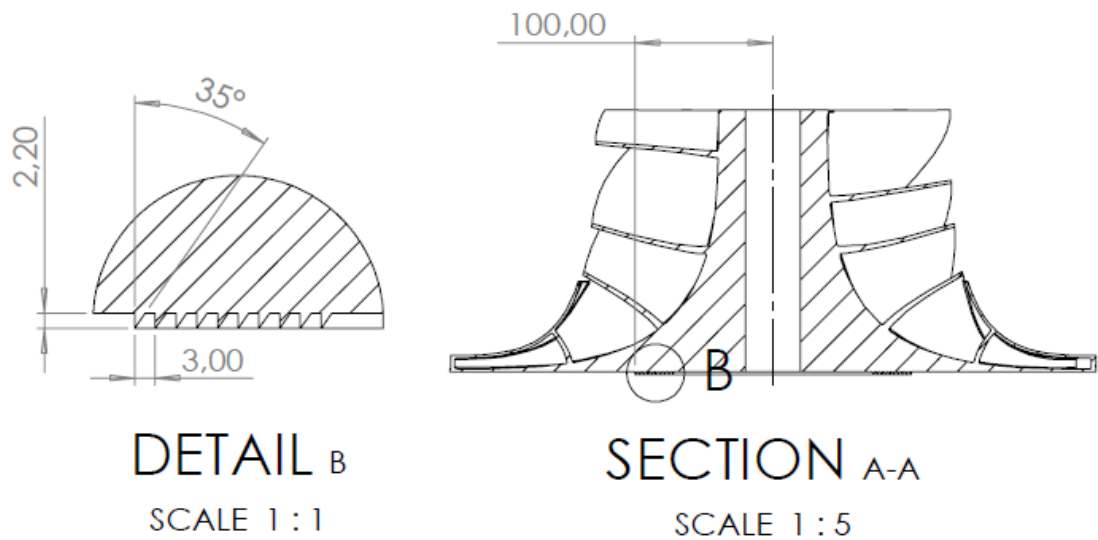


Figure 11. Base dimensions for radial seal.

For an axial seal, same dimensions are used, except seal radius r is 27.2 mm as presented in Figure 12. In axial review, seal radius is not a variable, but stays constant throughout the calculations.

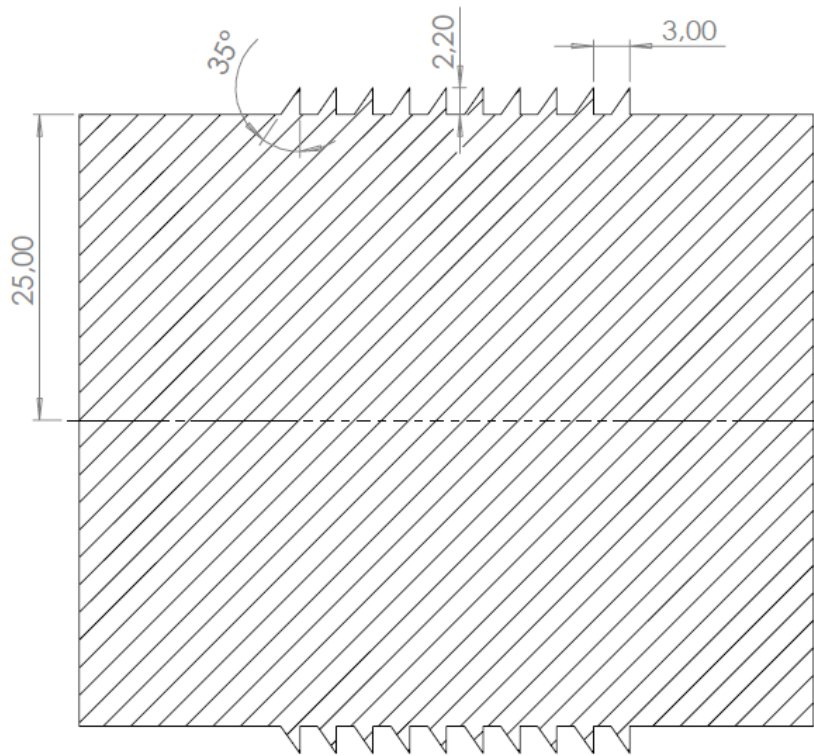


Figure 12. Base dimensions for axial seal.

3.2 Leakage optimization

This chapter presents results of leakage optimization. In a broad perspective, the final seal solution may be a compromise between leakage and some other factor, such as axial force, ease of manufacturability, ease of assembly, reliability, rotor dynamic effect and vibration. These are discussed in chapter 4.1. In this chapter, leakage optimization means leakage minimizing. The results describe how different seal geometries and variables affect leakage.

This chapter presents results of series of calculations, which are executed based on analytical methods presented in previous chapter as well as CFD simulation. All radial seal calculations are calculated or simulated using Ansys fluent, Martin's equation and Kearton's equation. All axial seal calculations are done using Egli's equations or simulated using Ansys Fluent. The results from different analytical methods and computational method, are then compared to each other in.

The calculation setup includes total of seven different variables, with each having 3–5 different values as shown in Table 3, where blue overlining shows the base dimensions. The calculations are done by changing only one variable at a time. Only one setup is needed for base dimensions, which then sums up to 19 setups for a radial seal and 15 setups for an axial seal.

Table 3. Different variables and their values.

Seal r , (mm)	50	75	100	125	150
Clearance c , (mm)		0.3	0.5	0.7	
Blade width b , (mm)		0.5	0.77	1.04	
Chamber width B , (mm)		2	3	4	
Blade height, (mm)		1.7	2.2	2.7	
Number of blades, (n)		7	10	13	
Blade shape	Rectangular	Spike	Inclined	Fishbone	Full labyrinth

Different blade shapes are presented in Figure 13. Inclined blade shape is presented in base setup figures.

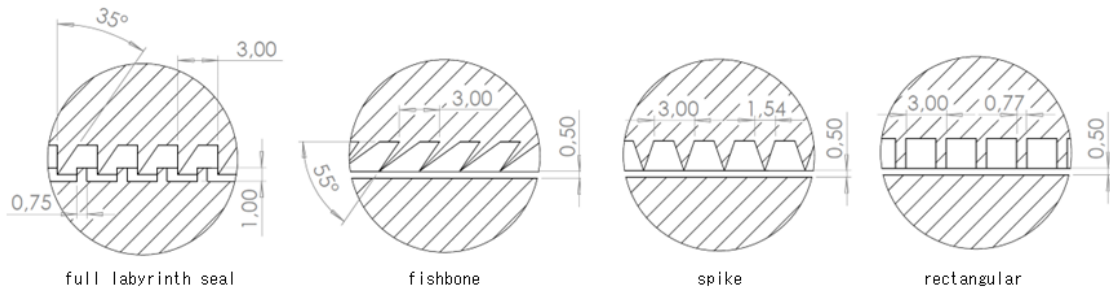


Figure 13. Full labyrinth, fishbone, spike, and rectangular seal blade shapes.

All calculations are done using the base values of the low-pressure compressor LPC in HT COMP project, which are the following:

- Fluid type – air (compressible ideal gas)
- Input temperature – 102°C
- Output temperature – 40°C
- Input pressure – 1.90 bar
- Output pressure – 0.35 bar

- Compressor mass flow – 7.81 kg/s

3.2.1 Ansys Fluent Computational Fluid Dynamic – CFD

In Ansys Fluent, the flow volume is first modelled using CAD, and then meshed into small cells either for a two-dimensional or a three-dimensional model. Base values such as fluid type and its compressibility, fluid density, input and output temperatures and pressures are specified after meshing. Calculation is done using Navier-Stokes equations with a user-defined set of iterations to obtain a more accurate Reynold's number after each iteration. In this thesis work, number of iterations is set to be 100. By solving the equations, mass flow can be obtained as well as visualizations for different physical attributes such as static pressure and velocity distribution as shown in Figures 14 and 15. The colourful area in the figure is the flow volume, and the white sharp geometries are the seal blades. Figure 14 shows, that the biggest pressure change happens at the flow path of the fluid.



Figure 14. Ansys Fluent contour of a static pressure distribution in a two-dimensional model.

Figure 15 presents velocity in different parts of the labyrinth seal. It can be seen that the velocity is not constant, but changes as the fluid moves within the seal. Also, the path of the fluid can be seen from the figure.

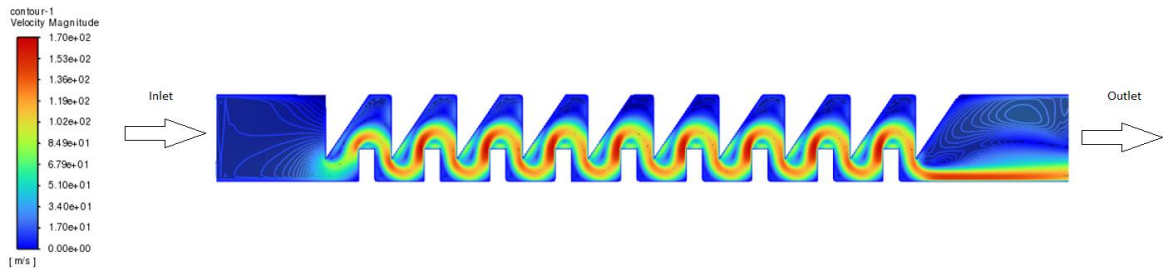


Figure 15. Ansys Fluent contour of velocity of a fluid in different parts of a labyrinth seal in a two-dimensional model.

In three-dimensional Ansys Fluent models, the same principles are used as in two-dimensional models, except the cells of the mesh have one more dimension, and therefore more degrees of freedom. Also in three-dimensional models, the material created by CAD acts as the flow mesh, and the empty space surrounding the material, acts as a solid boundary constraint. The Ansys Fluent model used for the calculations in this thesis work use the input parameters presented in Table 4.

Table 4. Input parameters for CFD calculations.

Mesh element size	0.5 mm
Inlet pressure	1.90 bar
Outlet pressure	0.35 bar
Inlet temperature	359 K
Outlet temperature	307 K
Fluid type	air
Turbulent intensity	5%
Turbulent viscosity ratio	10
Number of iterations for solver	100

When using tetrahedral elements, a good numerical accuracy is achieved using elements which have close to uniform dimensions in all their edges of the tetrahedra in most parts of the mesh. Small edges, curves, thin geometries, and sharp corners all result in edges or the tetrahedra to be inconsistent, decreasing the quality of the mesh. To validate the mesh quality and convergence in this thesis, Jacobian ratio check is used. Jacobian ratio calculates the length of the longest edge of an element in relation to the length of the shortest edge of the same element. By doing this, the Jacobian ratio calculates a specific aspect ratio for every

element. Aspect ratio of 1 means, that the element has a perfect tetrahedral shape, whereas ratio of 5 means, that the longest edge of the element is 5 times longer compared to the shortest edge of the element. In general, a mesh is considered having good quality, if more than 90% of its elements have a Jacobian ratio of less than 5. In this thesis work, all meshes of CFD calculations are validated by this method. (Solidworks Help, Dassault Systemes)

3.2.2 Results of leakage calculation

The calculation results for radial seal are presented in Table 5 and for axial seal in Table 6. The results presented are only for LPC of HT COMP project. The relative leakage is obtained by dividing the absolute leakage value by the total LPC compressor flow, which is 7.81 kg/s.

Table 5. Calculation results for absolute and relative leakages using analytical and computational methods for a radial seal.

Setup number	CFD leakage, m ³ /s, (%)	Martin leakage, m ³ /s, (%)	Kearton leakage, m ³ /s, (%)	Setup variable
1	0.021 (0.273%)	0.026 (0.334%)	0.013 (0.164%)	Seal r = 50.000 mm
2	0.034 (0.434%)	0.039 (0.502%)	0.026 (0.332%)	Seal r = 75.000 mm
3	0.048 (0.612%)	0.052 (0.670%)	0.038 (0.488%)	Seal r = 100.000 mm
4	0.061 (0.778%)	0.065 (0.837%)	0.050 (0.643%)	Seal r = 125.000 mm
5	0.073 (0.935%)	0.078 (1.004%)	0.062 (0.795%)	Seal r = 150.000 mm
6	0.084 (1.076%)	0.091 (1.172%)	0.074 (0.948%)	Seal r = 175.000 mm
7	0.094 (1.211%)	0.104 (1.339%)	0.086 (1.100%)	Seal r = 200.000 mm
8	0.104 (1.333%)	0.118 (1.507%)	0.098 (1.251%)	Seal r = 250.000 mm
9	0.030 (0.388%)	0.031 (0.402%)	0.023 (0.293%)	Clearance c = 0.300 mm
10	0.072 (0.921%)	0.073 (0.937%)	0.053 (0.684%)	Clearance c = 0.700 mm
11	0.049 (0.622%)	0.052 (0.670%)	0.039 (0.498%)	Blade width b = 0.500 mm
12	0.049 (0.626%)	0.052 (0.670%)	0.037 (0.479%)	Blade width b = 1.040 mm
13	0.065 (0.827%)	0.052 (0.670%)	0.041 (0.522%)	Chamber width B = 2.000 mm
14	0.044 (0.561%)	0.052 (0.670%)	0.035 (0.452%)	Chamber width B = 4.000 mm
15	0.048 (0.613%)	0.052 (0.670%)	0.038 (0.488%)	Blade height = 1.700 mm
16	0.048 (0.617%)	0.052 (0.670%)	0.038 (0.488%)	Blade height = 2.700 mm
17	0.059 (0.759%)	0.061 (0.777%)	0.049 (0.633%)	Blade number n = 7
18	0.040 (0.507%)	0.047 (0.598%)	0.030 (0.389%)	Blade number n = 13
19	0.058 (0.746%)	0.052 (0.670%)	0.038 (0.488%)	Blade shape: rectangular
20	0.049 (0.626%)	0.052 (0.670%)	0.038 (0.488%)	Blade shape: spike
21	0.048 (0.612%)	0.052 (0.670%)	0.038 (0.488%)	Blade shape: fishbone
22	0.038 (0.481%)	0.052 (0.670%)	0.038 (0.488%)	Blade shape: full labyrinth

Table 6. Calculation results for absolute and relative leakages using analytical and computational methods for an axial seal.

Setup number	CFD leakage, m ³ /s, (%)	Martin leakage, m ³ /s, (%)	Egli leakage, m ³ /s, (%)	Setup variable
1	0.024 (0.312%)	0.024 (0.307%)	0.019 (0.248%)	Base values
2	0.010 (0.133%)	0.014 (0.181%)	0.009 (0.113%)	Clearance c = 0.300 mm
3	0.040 (0.507%)	0.038 (0.480%)	0.028 (0.356%)	Clearance c = 0.700 mm
4	0.024 (0.312%)	0.024 (0.307%)	0.019 (0.248%)	Blade width b = 0.500 mm
5	0.024 (0.307%)	0.026 (0.329%)	0.019 (0.248%)	Blade width b = 1.040 mm
6	0.027 (0.351%)	0.027 (0.339%)	0.021 (0.269%)	Chamber width B = 2.000 mm
7	0.021 (0.273%)	0.022 (0.284%)	0.018 (0.232%)	Chamber width B = 4.000 mm
8	0.024 (0.306%)	0.024 (0.307%)	0.019 (0.241%)	Blade height = 1.700 mm
9	0.025 (0.316%)	0.024 (0.307%)	0.019 (0.241%)	Blade height = 2.700 mm
10	0.028 (0.357%)	0.027 (0.343%)	0.021 (0.262%)	Blade number n = 7
11	0.022 (0.279%)	0.022 (0.286%)	0.018 (0.234%)	Blade number n = 13
12	0.028 (0.353%)	0.024 (0.307%)	0.019 (0.248%)	Blade shape: rectangular
13	0.025 (0.315%)	0.024 (0.307%)	0.019 (0.248%)	Blade shape: spike
14	0.022 (0.278%)	0.024 (0.307%)	0.019 (0.248%)	Blade shape: fishbone
15	0.010 (0.124%)	0.009 (0.118%)	0.009 (0.110%)	Blade shape: full labyrinth

As can be seen from Figure 16 representing seal radius's effect on leakage with radial seal, as the radius increases, both analytical methods result in linear increase showing straight ascending lines, whereas CFD shows a slightly curving ascending line. The red and yellow lines are linear, because in all equations, the discharge area acts as a multiplier to the result, and seal radius acts as a multiplier for the discharge area. The absolute leakage difference between these three methods at 50 mm radius is about twice, which is a lot. But the relative effect in different radii is relatively uniform, which is more important. On average, the leakage increases by 0.25%, when seal radius is increased by 50 mm. In HT COMP project, the possible range of seal radius at the back of an LPC impeller is between 50...225 mm. In this range, the leakage varies on average between 0.26...1.36%, so the effect is major.

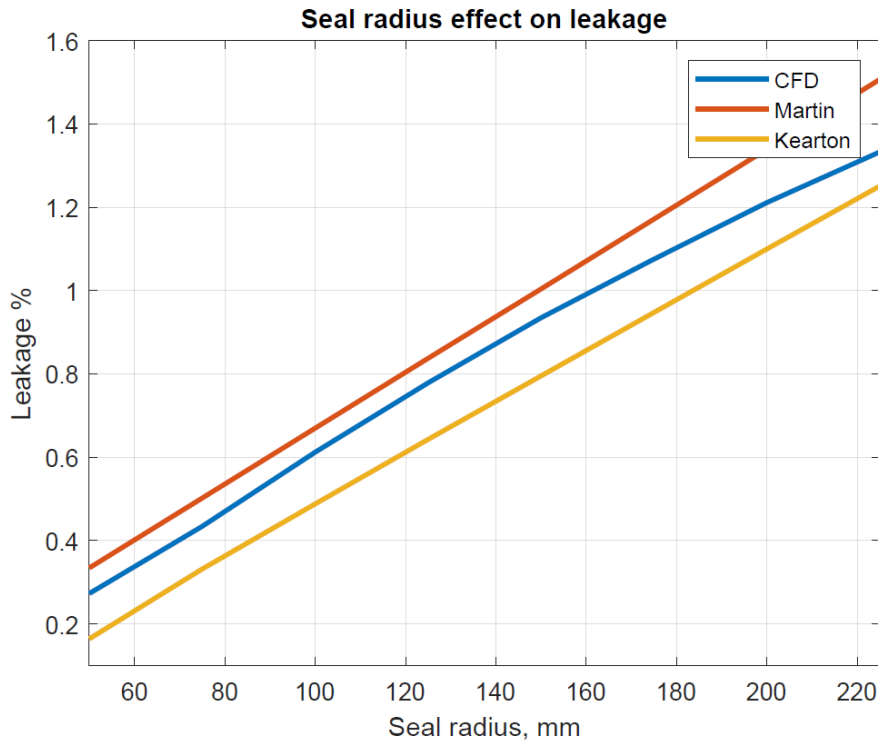


Figure 16. Seal radius effect on leakage for radial seal.

As can be seen from Figures 17 and 18 representing seal clearance effect on leakage with radial and axial seals, as the clearance increases, all methods in both radial and axial cases show linear or almost linear ascending lines. In Martin's and Kearton's methods, the lines are straight, because in their equations, the clearance exists only as a multiplier in discharge area, making the increase linear. In Egli's equation, in addition to that, clearance also affects indirectly the flow coefficient α , which is obtained from Figure 9 using relation of clearance and blade width and Reynolds number. In the results, about 1.4 times difference between methods can be seen in leakage when clearance is 0.3 mm. Despite the relatively large absolute difference between methods, the slopes of the lines are relatively close to each other. This means the significance of clearance can be estimated relatively well. When clearance increases by 0.2 mm, the leakage increases on average about 0.24% in radial case and about 0.17% in axial case. Between clearance of 0.3...0.7 mm the leakage varies on average between 0.36...0.85% in radial case and 0.16...0.49% in axial case, meaning the effect is major.

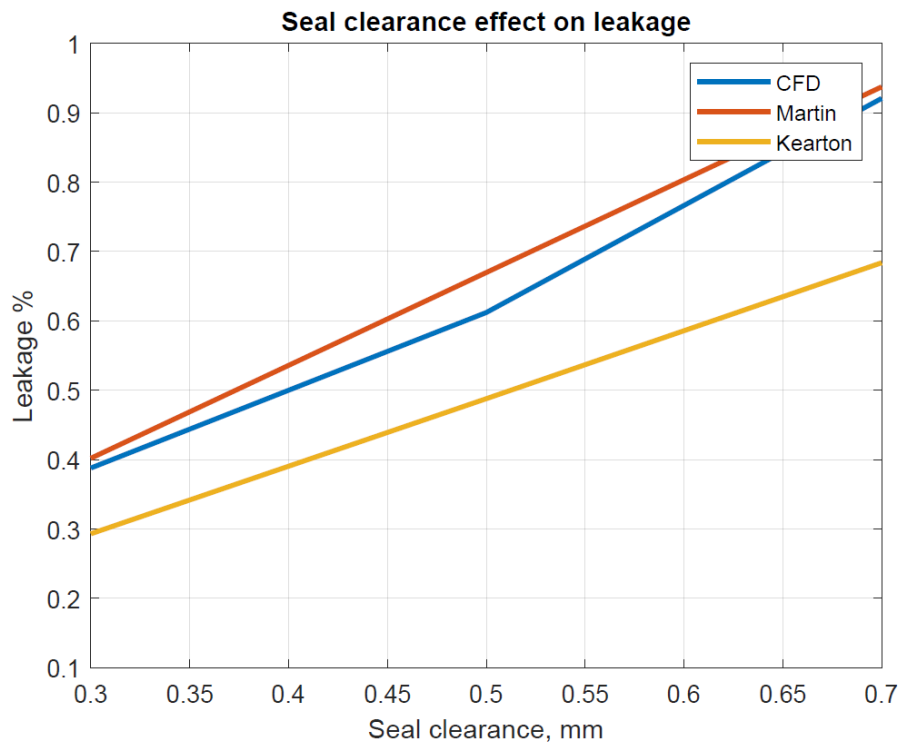


Figure 17. Seal clearance effect on leakage for radial seal.

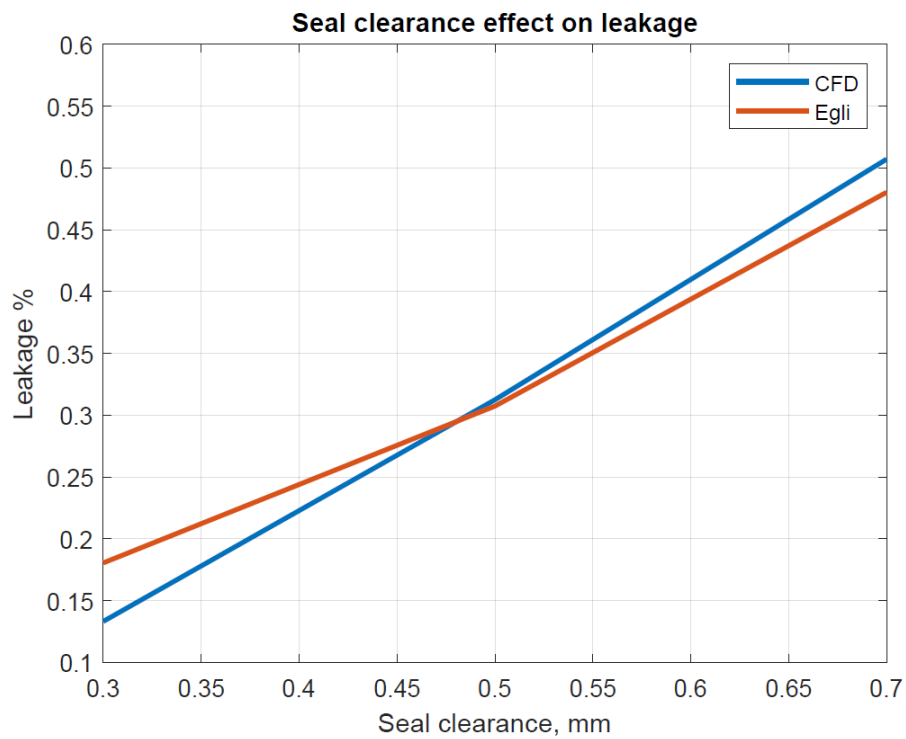


Figure 18. Clearance effect on leakage for axial seal.

As can be seen from Figures 19 and 20 representing blade width effect on leakage with radial and axial seals, the effect is only minor. This is probably because, increasing blade width

itself, increases efficiency, but when it takes the space from chamber width, it offsets the benefit. This assumption is not verified by calculation results and would require further studies to make a conclusion. In radial case, the lines from all methods are flat or close to flat. In axial case, Egli's line is slightly ascending and CFD line is slightly descending, meaning they are contradictory, but it is important to note that the effect is only minor. In axial case, when blade width is approximately doubled, leakage by Egli's method goes only from about 0.295 to 0.328%. With CFD, the effect is even smaller. By observing these results, it can be concluded that the effect of blade width, when it takes space from chamber width, is relatively small.

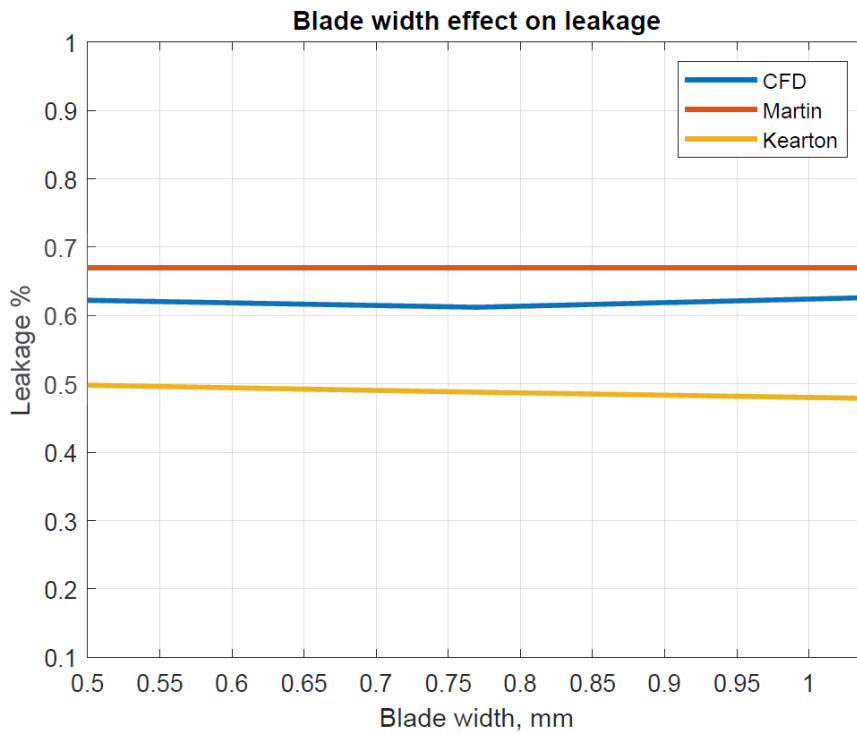


Figure 19. Blade width effect on leakage for radial seal.

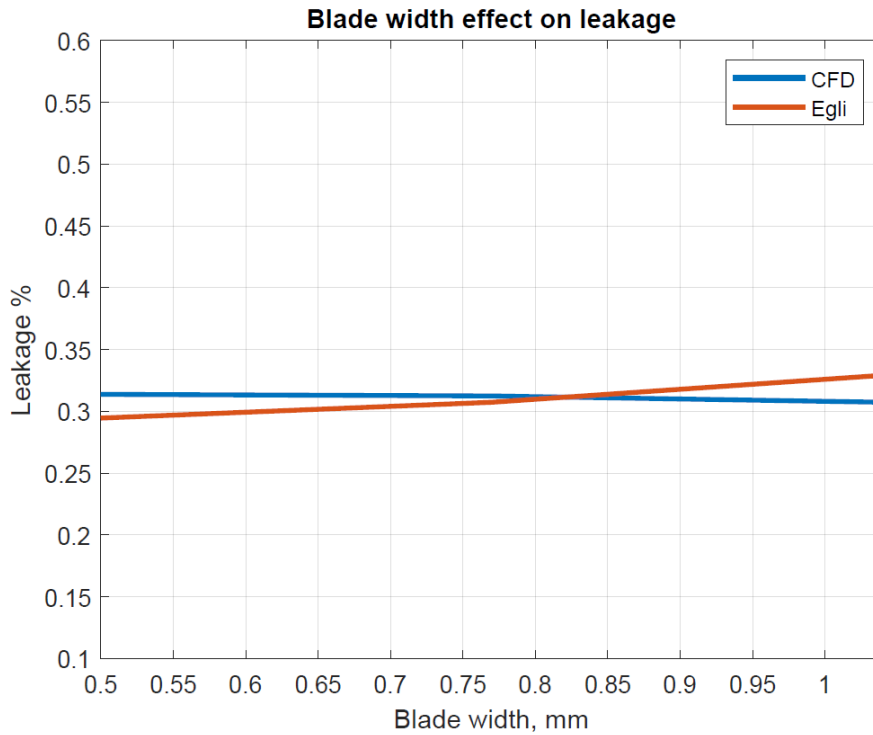


Figure 20. Blade width effect on leakage for axial seal.

As can be seen from Figures 21 and 22 representing chamber width effect on leakage with radial and axial seals, the effect is moderate. It is logical to assume that the effect is significant since it is known that some of the kinetic energy dissolves in each chamber because of pressure difference. Therefore, it can be assumed, that the larger the volume difference between the discharge location and the chamber, the more kinetic energy is dissolved in each chamber. Increasing chamber width increases this difference. The line representing Martin's method in radial case is flat, because in Martin's equation, chamber width is completely ignored. Kearton's method includes chamber width into the equation using total area factor ϕ_n resulting in a descending line. Egli includes chamber width in kinetic energy carryover coefficient ε , resulting also in a descending line as well as CFD. Because Martin ignores chamber width, it should be excluded from the review of this variable. Comparing Kearton's and CFD lines in a radial case, even though both correctly descend, the starting and ending values as well as the steepness of these lines are vastly different. Kearton's results should be interpreted with caution and CFD to be more accurate. In axial case, comparing Egli's and CFD lines, both have relatively similar steepness and starting and ending values, meaning they have some correlation. By doubling the chamber

width, leakage decreases on average from 0.83 to 0.56% in radial case and from 0.35 to 0.28% in axial case, meaning the effect is moderate.

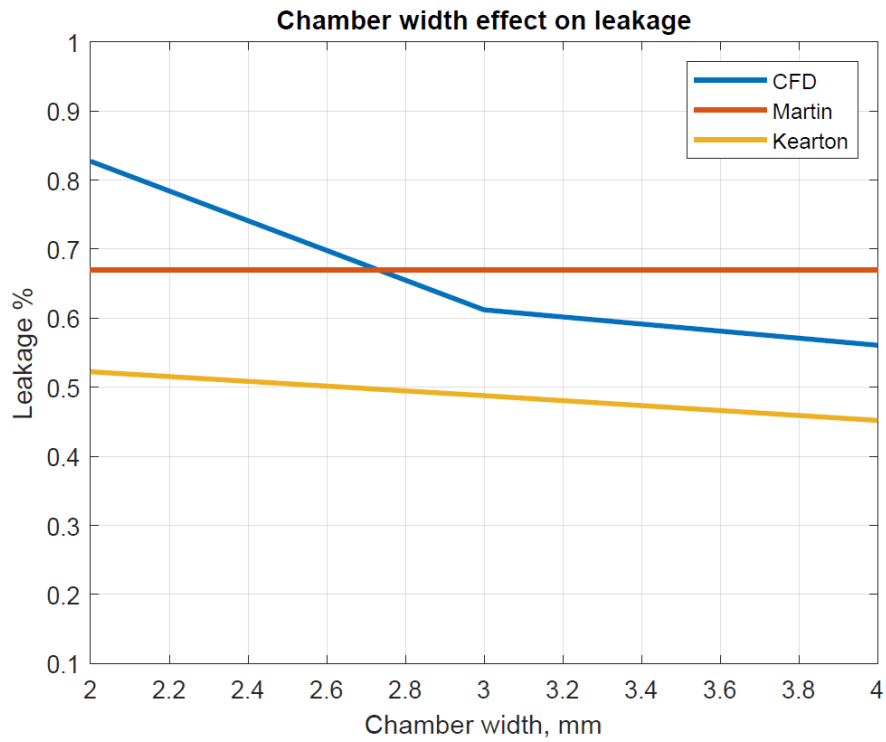


Figure 21. Chamber width effect on leakage for radial seal.

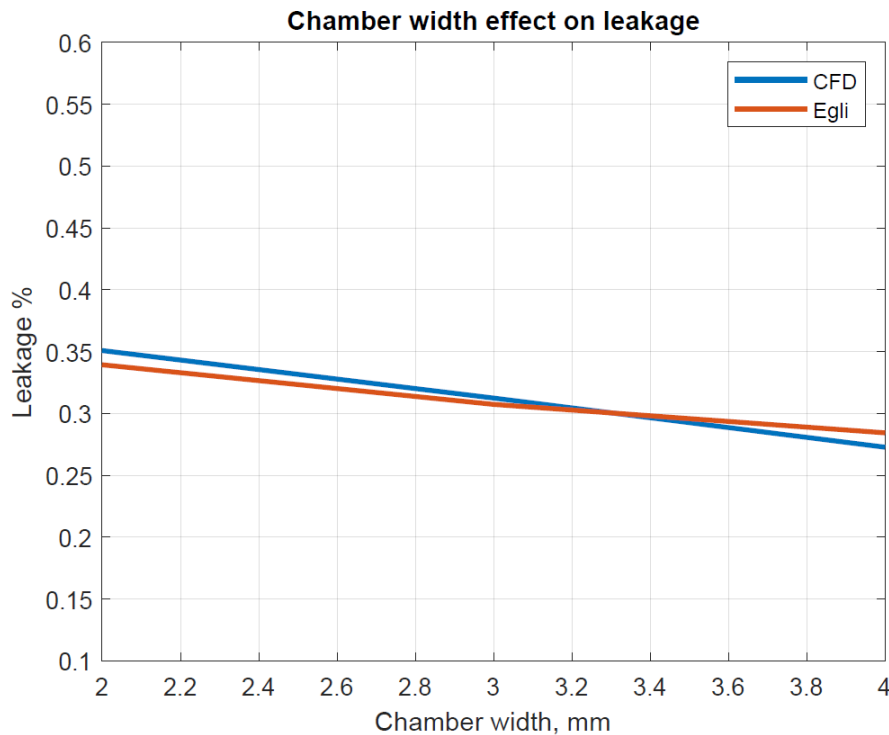


Figure 22. Chamber width effect on leakage for axial seal.

As can be seen from Figures 23 and 24 representing blade height effect on leakage with radial and axial seals, the effect is only minor. Lines from all three analytical methods stay flat, meaning they don't include blade height in their equations. CFD calculated leakage shows only 0.004% increase in radial case, and 0.010% increase in axial case, when blade height was increased from 1.7 mm to 2.7 mm, meaning the effect is minor. Chamber volume can be equally increased by either increasing blade height or chamber width, however increasing chamber width shows more effect on leakage. This might happen, because increasing chamber width means increasing the volume in the direction of the flow and increasing blade height increases volume perpendicular to the flow. It could be so that more kinetic energy dissolves in a chamber when the chamber has more width and depth, meaning more volume in flow direction.

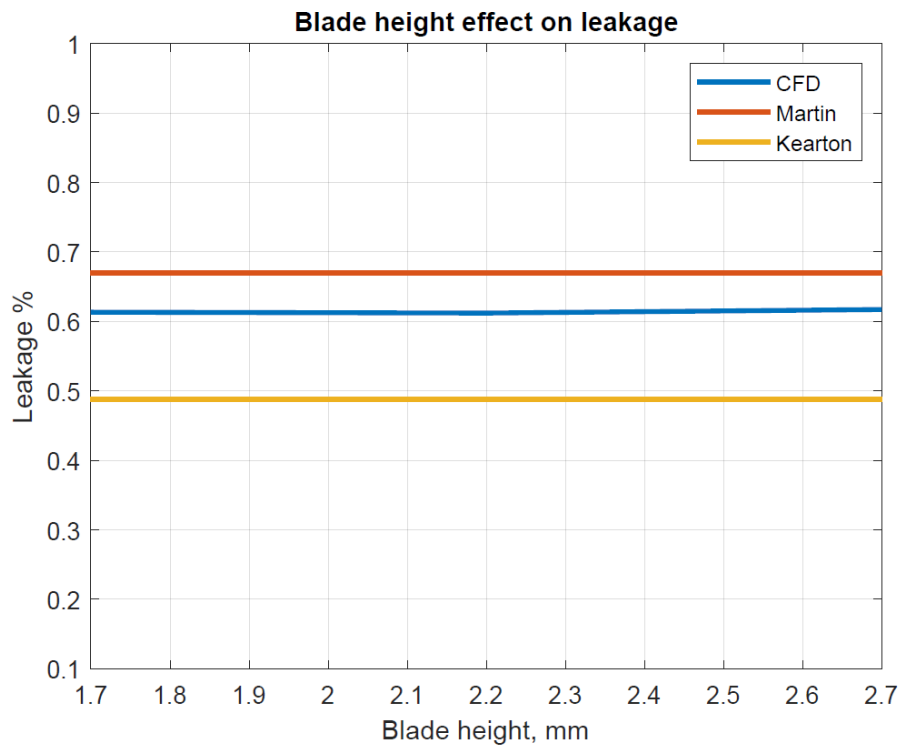


Figure 23. Blade height effect on leakage for radial seal.

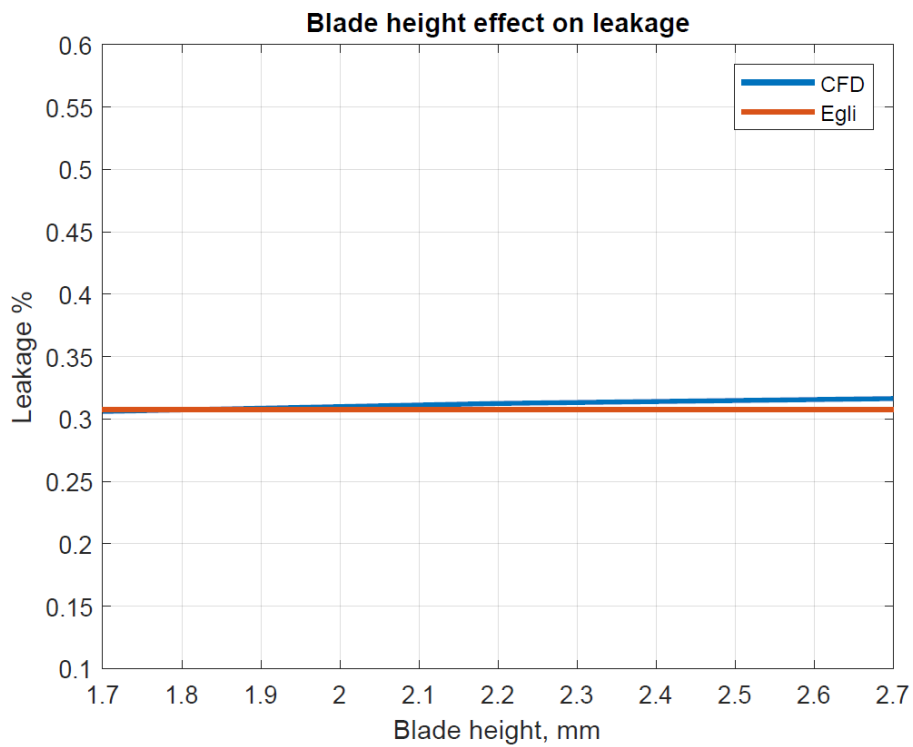


Figure 24. Blade height effect on leakage for axial seal.

As can be seen from Figures 25 and 26 representing blade number effect on leakage with radial and axial seals, the effect is moderate. All four methods take into account blade

number and all result decreasing leakage when number of blades is increased. This is because every consecutive discharge point with its following chamber reduces pressure and releases energy by expanding and compressing the flow. The more blades and chambers, the better efficiency. However, all lines are slightly curved meaning that, by increasing number of blades, efficiency does not increase linearly. This is because the first blades and chambers reduce more absolute pressure than the last ones, while the relative pressure reduction is approximately same. By increasing number of blades from 7 to 13, leakage reduces on average from 0.72 to 0.50% in radial case and from 0.35 to 0.28% in axial case, meaning the effect is moderate.

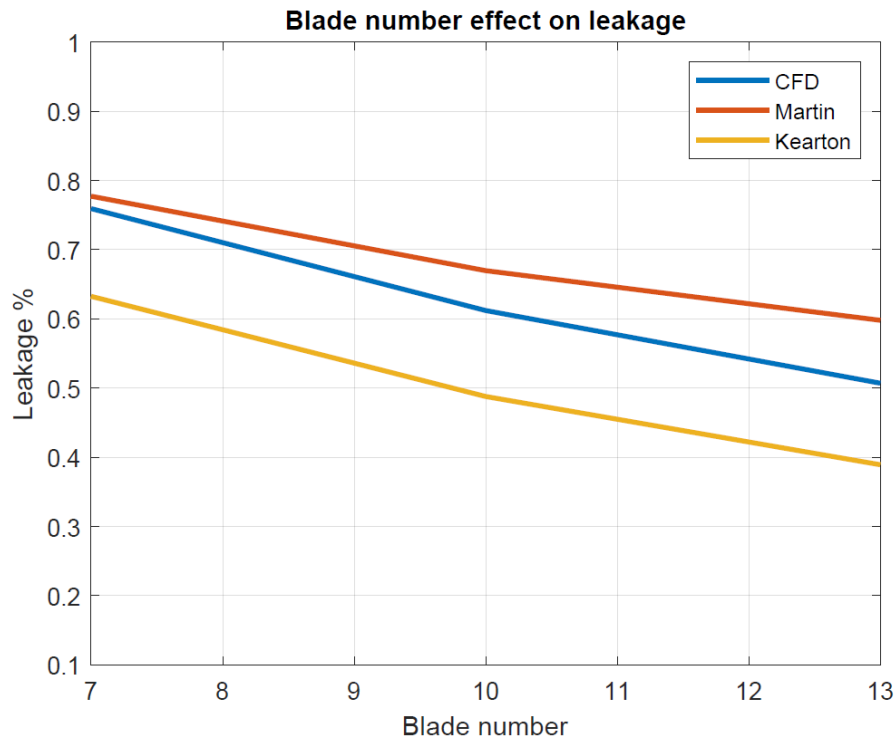


Figure 25. Blade number effect on leakage for radial seal.

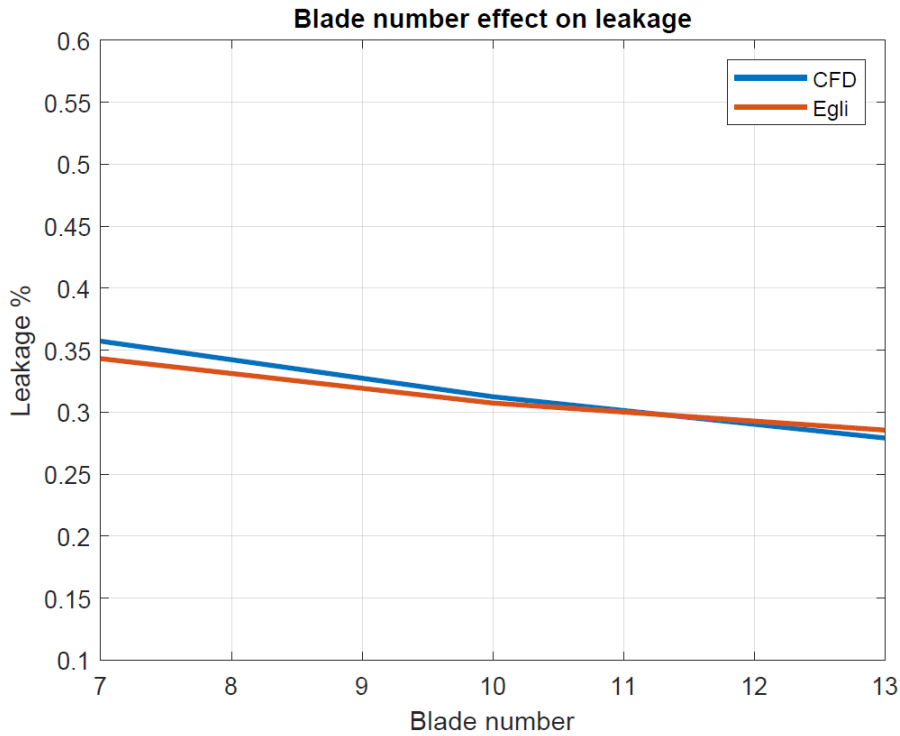


Figure 26. Blade number effect on leakage for axial seal.

Figures 27 and 28 show blade shape effect on leakage. Martin's and Kearton's methods do not include different shapes in their equations. These methods give the same leakage to full and half labyrinth seals. Because of this reason, only CFD results are shown in Figure 27. Egli's method takes into account kinetic energy carryover coefficient ε , which is estimated for each shape. Because of this, it can be concluded that also Egli's method is not accurate enough to evaluate different shapes, except the full labyrinth, which gets a $\varepsilon=1$, because full labyrinth is considered to be an ideal labyrinth seal, where all kinetic energy dissolves in seal chambers. In Egli's method, the kinetic energy carryover coefficient for different shapes is guessed, which is not an accurate approach.

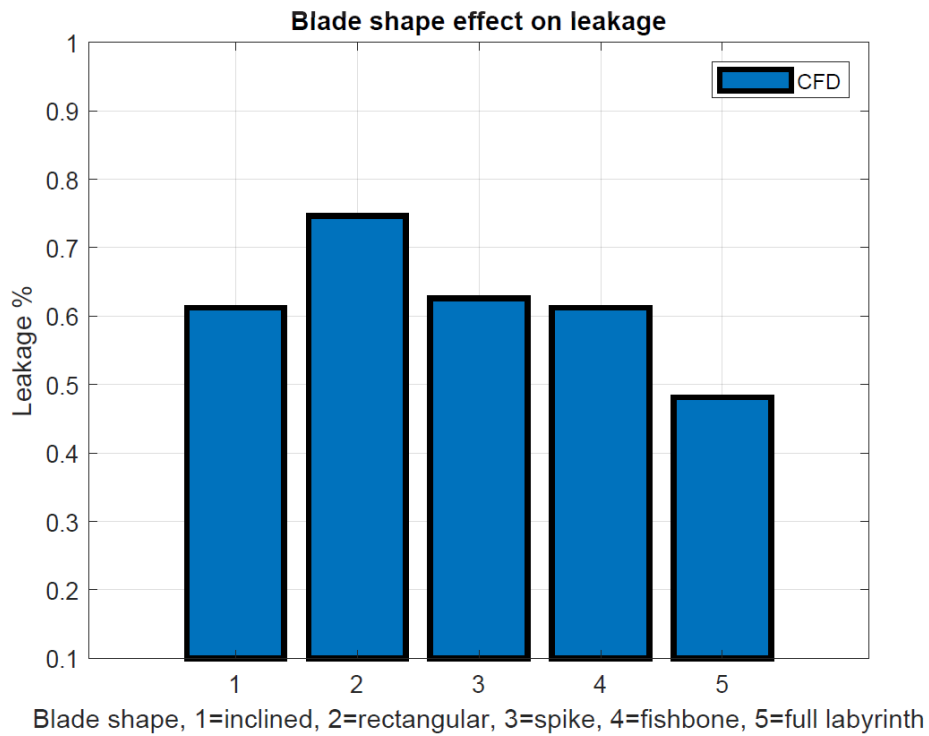


Figure 27. Blade shape effect on leakage for radial seal.

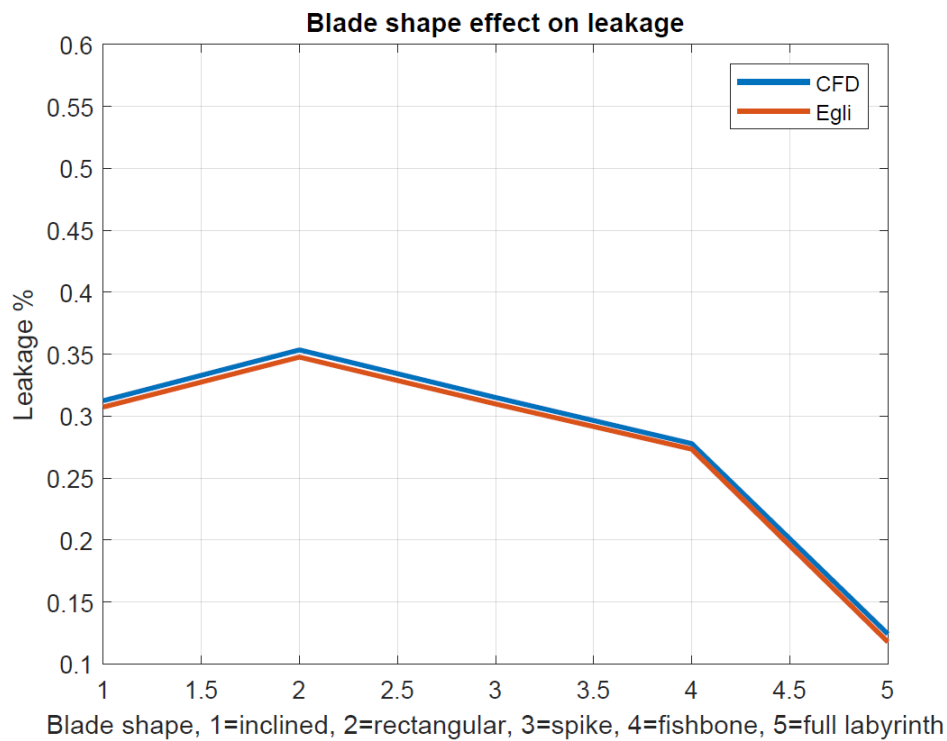


Figure 28. Blade shape effect on leakage for axial seal.

CFD results show that rectangular shape increases leakage from 0.61 to 0.75% in radial case and from 0.31 to 0.35% in axial case compared to the inclined one. Sharp edge works better

probably because it creates more turbulence when the flow passes by, whereas a rectangular shape gives the flow a smooth edge to travel by. If a sharp edge can be easily manufactured, there is no reason to choose a rectangular shape. Spike shape results virtually same result than inclined. This is probably because the angle of the spike is the same as in inclined shape. Spike edge is a suitable alternative for inclined shape.

Fishbone shape decreases leakage from 0.31 to 0.28% in axial case and stays the same in radial case. Slightly better efficiency with fishbone shape is achieved probably because some of the flow gets trapped inside a chamber since the blade is inclined to the opposite direction than the flow. Fishbone shape is more complicated to manufacture compared to inclined shape, and because it offers only a small improvement in efficiency, it is probably not the best option.

Full labyrinth reduces leakage from 0.61 to 0.48% in radial case and from 0.31 to 0.12% in axial case. Full labyrinth is more efficient compared to half labyrinth because it does not offer a straightforward path for the flow, forcing the fluid to dissolve more kinetic energy in the chambers. Full labyrinth is a good option since it offers a significant improvement to efficiency. The challenge with full labyrinth is to manufacture both sides of the seal to fit together with acceptable tolerances to avoid failures, but small enough clearance to be effective. This is a compromise between failure possibility and efficiency. In radial full labyrinth, the larger the seal radius, the more sensitive it is to failure.

Figures 29 and 30 present a broad perspective of how different variables affect leakage. In these figures, only two data points, the start and end values, are used instead of three. Therefore, it must be noted, that in reality, the lines are not linear. Only the start and end points are accurate.

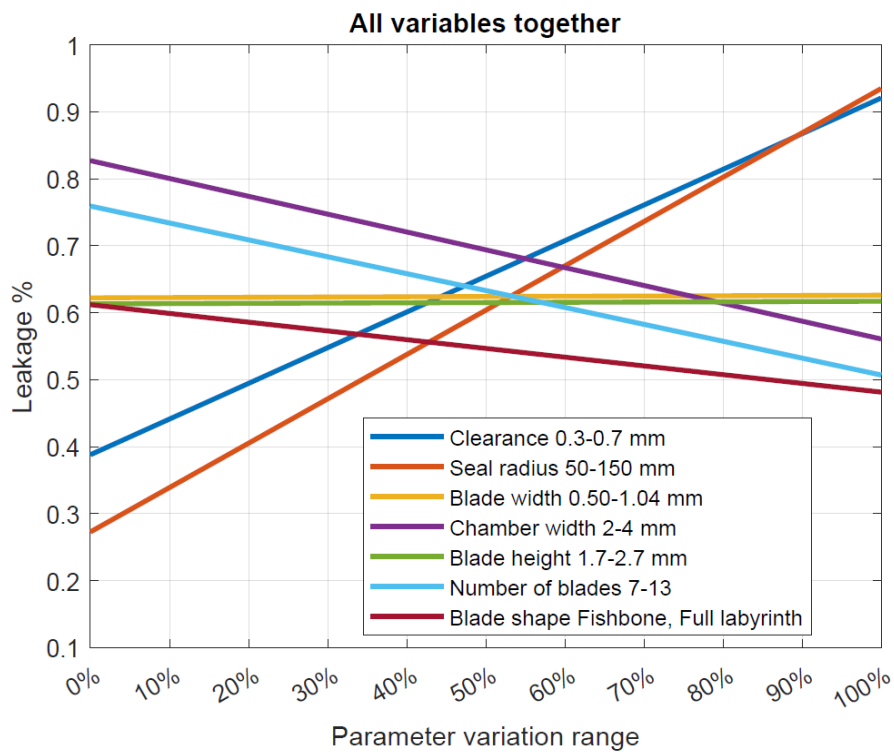


Figure 29. All variables and their effects on leakage for radial seal.

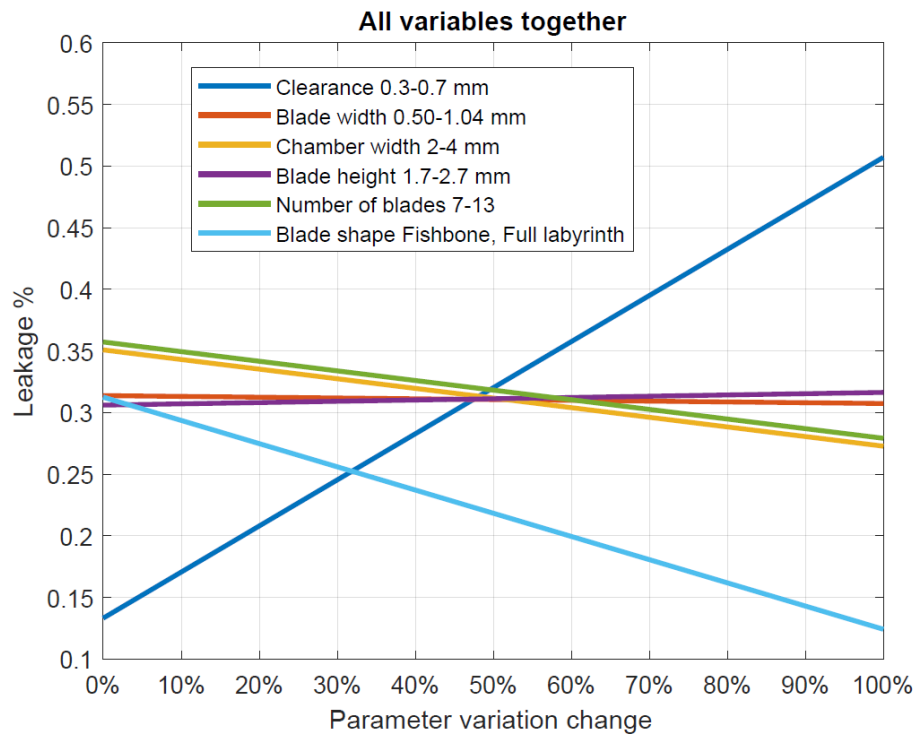


Figure 30. All variables and their effects of leakage for axial seal.

Based on results presented in preceding figures, it can be concluded that the relative magnitude of different variables to leakage can be expressed as minor, moderate, and major effects. These are presented in Table 7.

Table 7. Effect of each labyrinth seal design variable to leakage.

Variable	Value range	Radial case: leakage range	Axial case: leakage range	Effectiveness
Seal radius	50...225 mm	0.26...1.36%	-	major
Clearance	0.30...0.70 mm	0.36...0.85%	0.16...0.48%	major
Blade width	0.50...1.04 mm	0.56...0.55%	0.30...0.32%	minor
Chamber width	2.00...4.00 mm	0.67...0.51%	0.35...0.28%	moderate
Blade height	1.70...2.7 mm	0.61...0.62%	0.31...0.31%	minor
Number of blades	7...13	0.72...0.50%	0.35...0.28%	moderate
Blade shape	half labyrinth - full labyrinth	0.75...0.48%	0.35...0.12%	major

3.3 Dynamic coefficients for an axial seal

Rotor dynamic coefficients K_d – direct stiffness, k_c – cross-coupled stiffness, C_d – direct damping, c_c – cross-coupled damping, and m_d – direct mass are calculated using two different analytical methods: Black’s method (1970) and Child’s method (1983) as presented in chapter 2.3. Only two variables of the seal geometry affect the calculations of rotor dynamic coefficients: seal length L and clearance c . Results were obtained using 21 different combinations: 11 different seal lengths using a range of 15...45 mm with 3 mm increments and 10 different clearances using a range of 0,1...1,0 mm with 0,1 mm increments. The results for Black’s and Child’s methods are shown in Tables 8 and 9 below.

Table 8. Rotor dynamic coefficients using different seal variables using Black's method.

Setup number	Variable	K_d (N/m)	k_c (N/m)	C_d (Ns/m)	c_c (Ns/m)	m_d (kg)
1	$L = 15$ mm	30175	6399	10.94	-0.005	-4.54E-6
2	$L = 18$ mm	38140	8443	14.66	0.026	2.27E-05
3	$L = 21$ mm	45472	10693	18.57	0.087	7.54E-05
4	$L = 24$ mm	51944	12991	22.56	0.185	1.60E-04
5	$L = 27$ mm	57433	15299	26.56	0.326	2.83E-04
6	$L = 30$ mm	61916	17573	30.51	0.517	4.49E-04
7	$L = 33$ mm	65411	19788	34.36	0.762	6.61E-04
8	$L = 36$ mm	67987	21924	38.07	1.064	9.24E-04
9	$L = 39$ mm	69734	23969	41.62	1.426	1.20E-03
10	$L = 42$ mm	70753	25914	44.99	1.851	1.60E-03
11	$L = 45$ mm	71135	27756	48.19	2.338	2.00E-03
12	$c = 0.1$ mm	162010	84245	146.27	5.224	4.50E-03
13	$c = 0.2$ mm	138830	37680	65.42	2.476	2.10E-03
14	$c = 0.3$ mm	106450	25989	45.12	1.437	1.20E-03
15	$c = 0.4$ mm	80680	20704	35.95	0.868	7.53E-04
16	$c = 0.5$ mm	61916	17573	30.51	0.517	4.49E-04
17	$c = 0.6$ mm	48397	15420	26.77	0.289	2.51E-04
18	$c = 0.7$ mm	38550	13806	23.97	0.136	1.18E-04
19	$c = 0.8$ mm	31244	12529	21.75	0.031	2.72E-05
20	$c = 0.9$ mm	25723	11483	19.94	-0.041	-3.59E-5
21	$c = 1.0$ mm	21474	10605	18.41	-0.092	-8.02E-5

Table 9. Rotor dynamic coefficients using different seal variables using Child's method.

Setup number	Variable	K_d (N/m)	k_c (N/m)	C_d (Ns/m)	c_c (Ns/m)	m_d (kg)
1	$L = 15$ mm	42518	7527	13.07	0.478	4.15E-04
2	$L = 18$ mm	56161	10529	18.28	0.802	6.96E-04
3	$L = 21$ mm	70313	13951	24.22	1.237	1.10E-03
4	$L = 24$ mm	84698	17773	30.86	1.796	1.60E-03
5	$L = 27$ mm	99111	21980	38.16	2.491	2.20E-03
6	$L = 30$ mm	113390	26561	46.12	3.331	2.90E-03
7	$L = 33$ mm	127430	31505	54.70	4.327	3.80E-03
8	$L = 36$ mm	141130	36807	63.91	5.487	4.80E-03
9	$L = 39$ mm	154460	42464	73.73	6.822	5.90E-03
10	$L = 42$ mm	167340	48470	84.16	8.339	7.20E-03
11	$L = 45$ mm	179770	54827	95.19	10.047	8.70E-03
12	$c = 0.1$ mm	321470	107320	186.34	8.548	7.40E-03
13	$c = 0.2$ mm	267230	53384	92.69	5.781	5.00E-03
14	$c = 0.3$ mm	200560	38693	67.18	4.606	4.00E-03
15	$c = 0.4$ mm	149590	31296	54.34	3.863	3.40E-03
16	$c = 0.5$ mm	113390	26561	46.12	3.331	2.90E-03
17	$c = 0.6$ mm	87769	23164	40.22	2.926	2.50E-03
18	$c = 0.7$ mm	69667	20570	35.71	2.608	2.30E-03
19	$c = 0.8$ mm	55807	18510	32.14	2.351	2.00E-03
20	$c = 0.9$ mm	45665	16829	29.22	2.140	1.90E-03
21	$c = 10.0$ mm	37915	15429	26.79	1.962	1.70E-03

From Figures 31-32, it can be seen how *seal length* affects the dynamic coefficients, when seal clearance is set to be 0,5 mm. From Figure 31, it can be seen that direct stiffness and seal length are almost linearly correlated, when used Child's method. When Black's method is used, the stiffness increases more when seal length is increased from 15 to 30 mm, than when increased from 30 to 45 mm. When seal length is increased from 15 to 45 mm, the direct stiffness increases more than four times using Child's method and more than two times using Black's method.

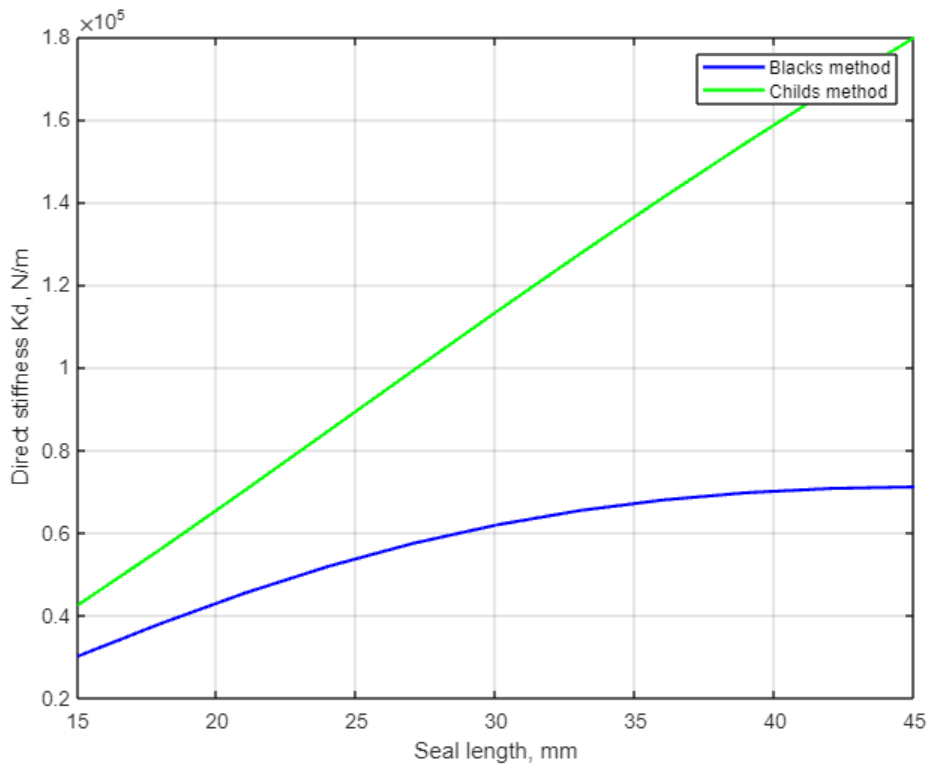


Figure 31. Seal length effect on direct stiffness.

Figures 32–34 show the relationship between seal length and cross-coupled stiffness, direct damping, and cross-coupled damping. From these figures, it can be seen that Child's method gives a larger result for every dynamic coefficient in every seal length. It can also be seen that the two methods correlate more, when the seal is short, and less when the seal is long. This is because Child's method uses a so-called short seal solution, whereas Black's method uses corrective coefficients for a finite length seal. (Chen 2005, p. 300-301). Generally, Black's method is more reliable with longer seal lengths as it uses finite seal length instead of assuming the seal to be short. When the seal is short, there is not a significant difference.

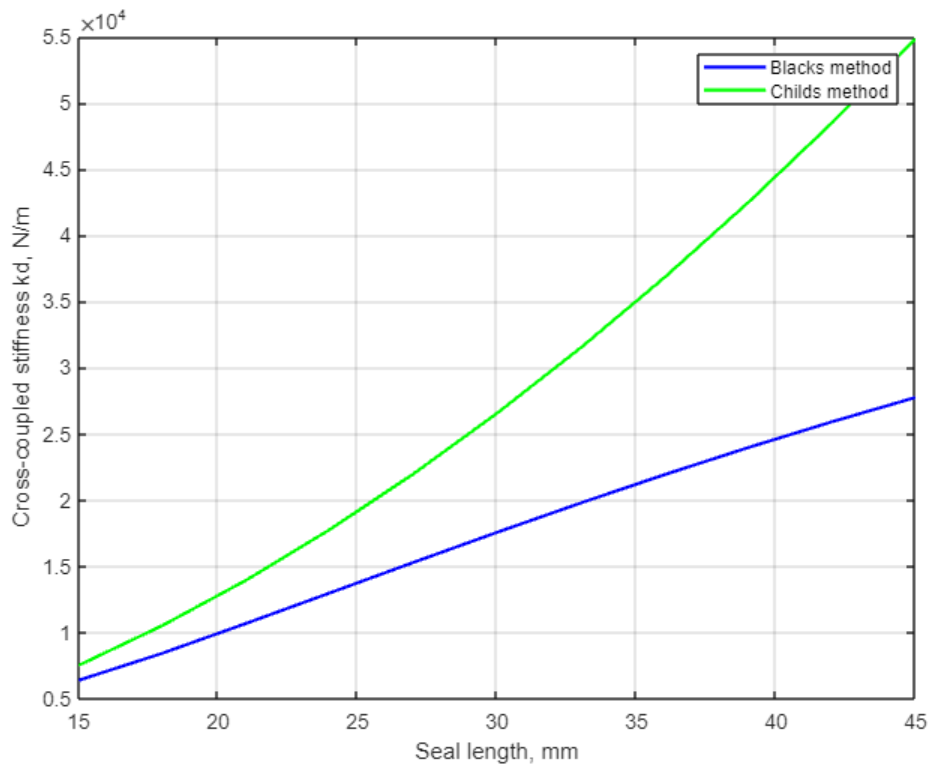


Figure 32. Seal length effect on cross-coupled stiffness.

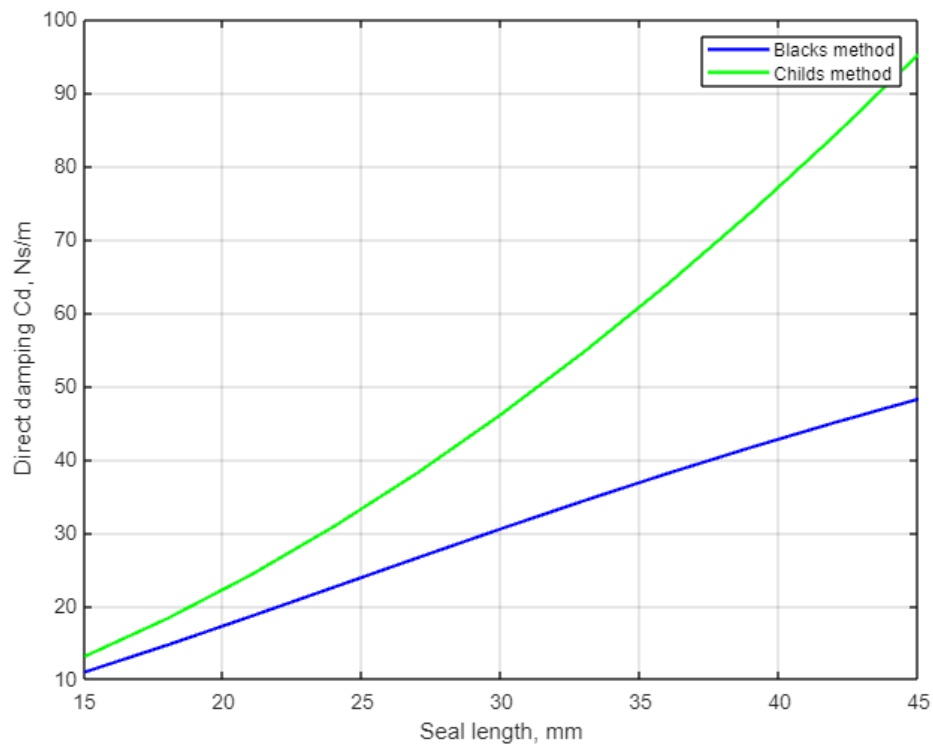


Figure 33. Seal length effect on direct damping.

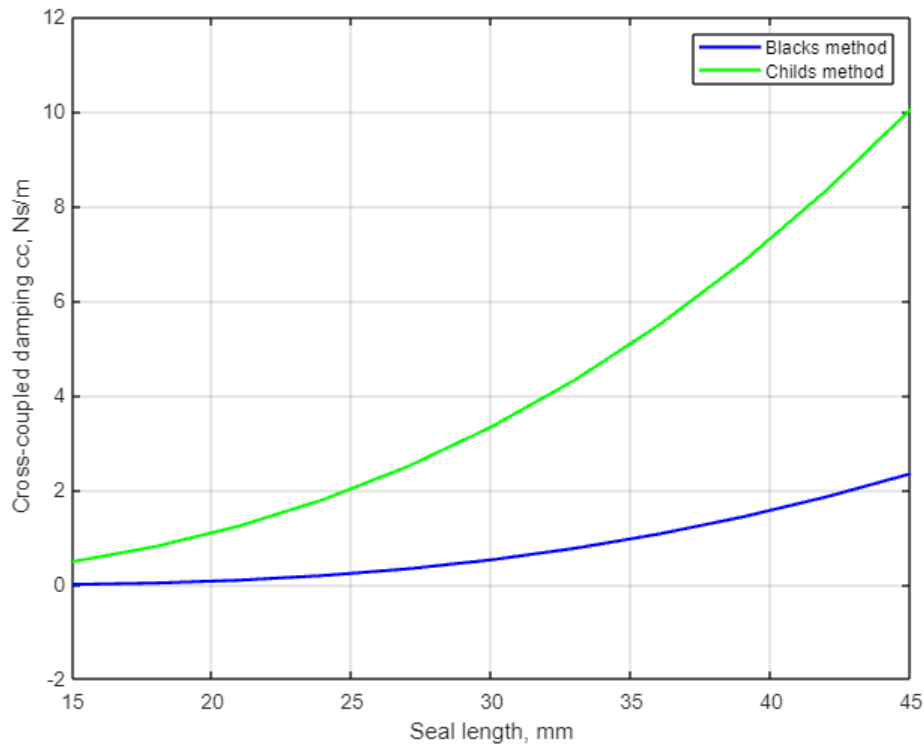


Figure 34. Seal length effect on cross-coupled damping.

From Figures 35–38, it can be seen how *seal clearance* affects the dynamic coefficients, when seal length is set to be 30 mm. From these figures, it can be seen, that the two methods are more uniform, when the clearance changes, compared to change in seal length. This is also, because of the short seal solution used by the Child's method. From Figures 35–38, it can be seen that Child's method gives a larger result for every dynamic coefficient in every seal clearance, but the shapes of the lines are relatively uniform. When calculating direct stiffness, Child's method gives approximately twice as large result compared to Black's as shown in Figure 35.

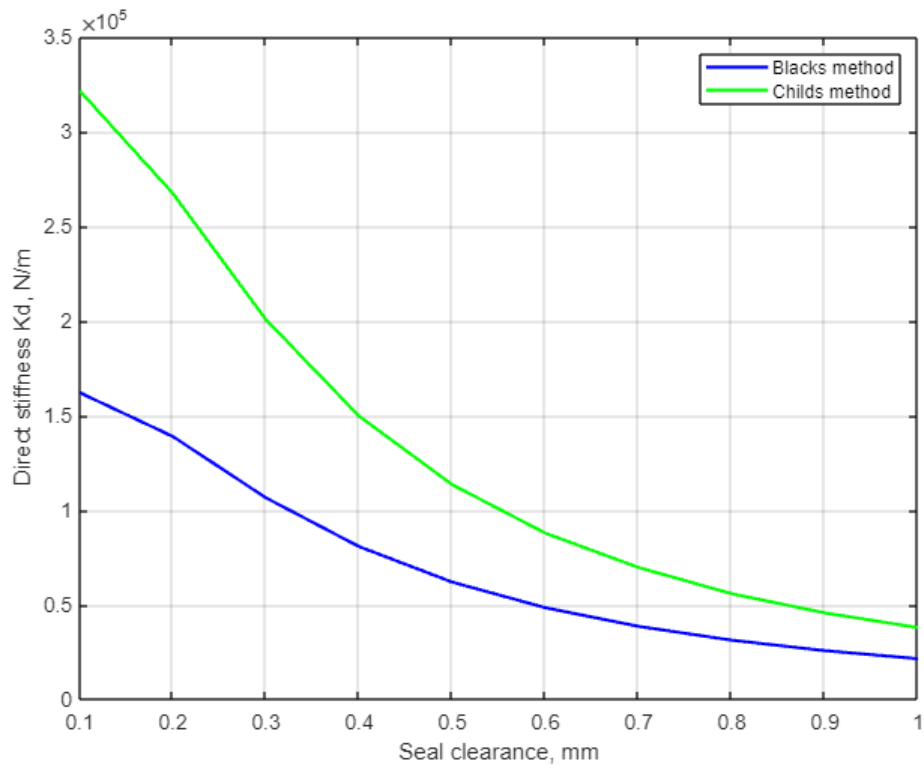


Figure 35. Seal clearance effect on direct stiffness.

For cross-coupled damping, it makes even larger difference as shown in figure 36.

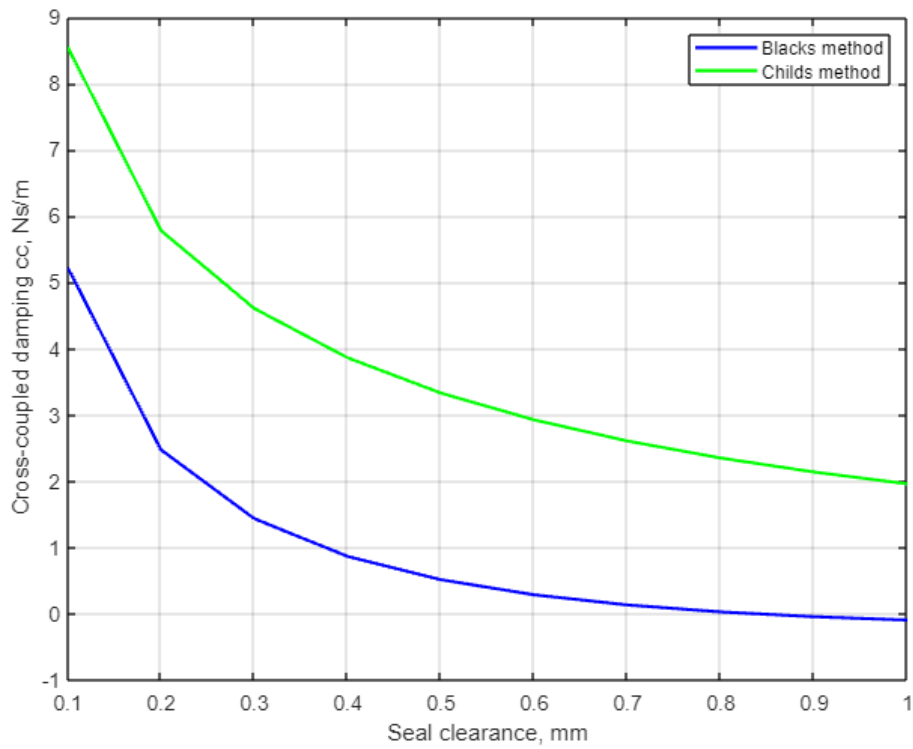


Figure 36. Seal clearance effect on cross-coupled damping.

With cross-coupled stiffness and direct damping, the difference is smaller as shown in Figures 37 and 38.

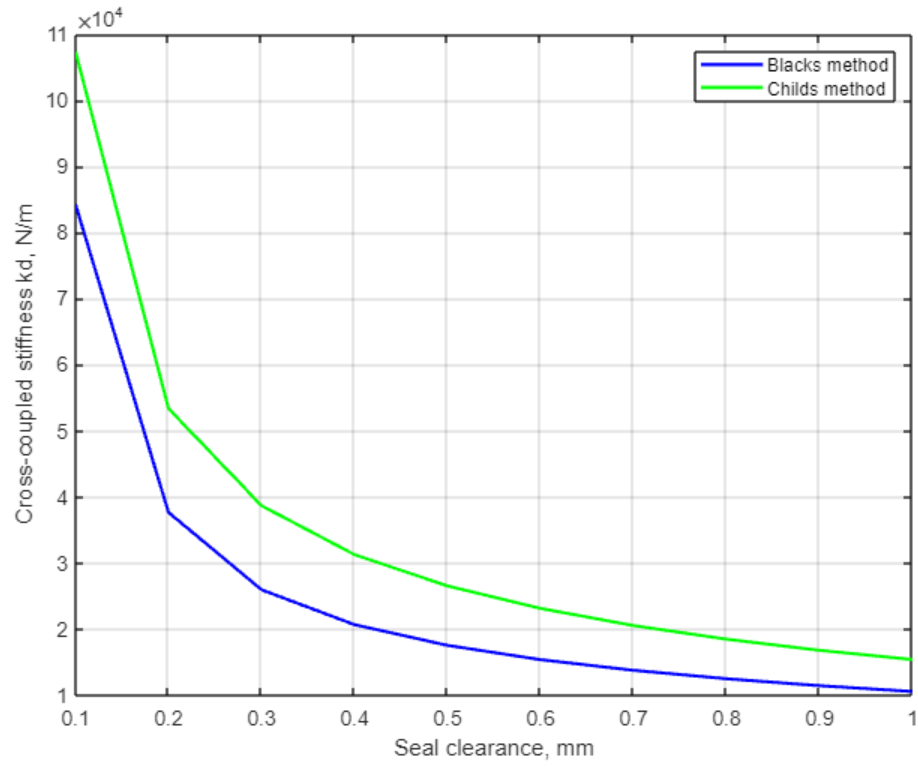


Figure 37. Seal clearance effect on cross-coupled stiffness.

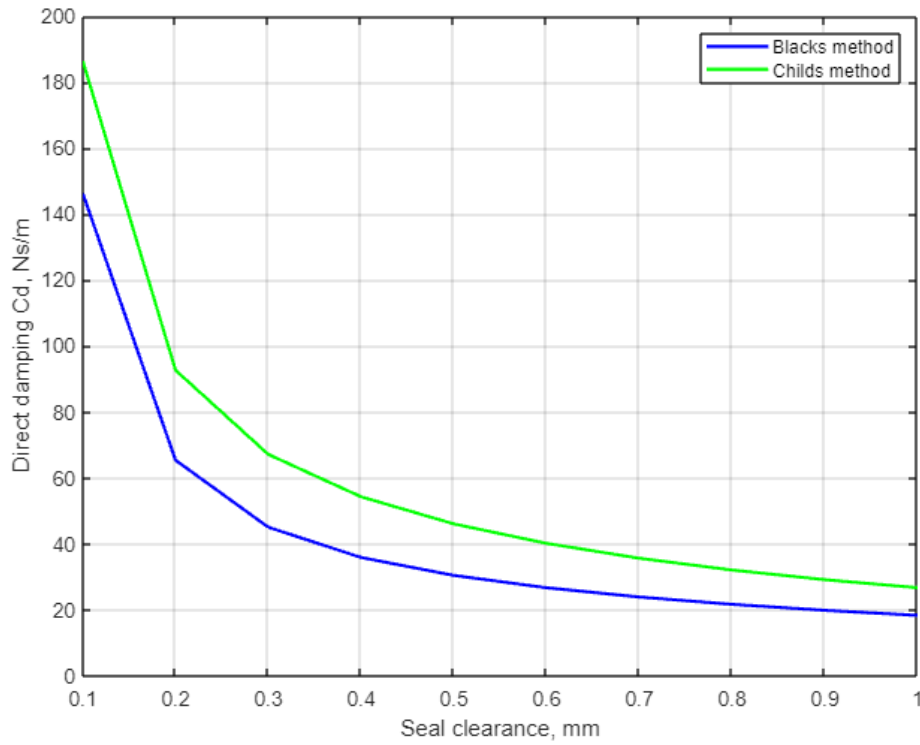


Figure 38. Seal clearance effect on direct damping.

This difference comes from fundamental differences in equations of these methods. Child's method is based on Gerard Hirs' lubrication equation, where the fluid inertia terms are included in the equations. Also in Child's method, the inlet swirl is not a constant, but changes as a function of mean axial velocity. In Black's method, the inlet swirl is always 0.5, which is a typical value. The inlet swirl is the fluid's circumferential velocity entering the seal in proportion to the shaft surface speed. It does not have a significant effect on direct stiffness or damping, but significantly affects the cross-coupled terms. (Chen 2005, p. 298–301)

Apart from the rotor dynamic effect of the seals, the impeller also adds stiffness into the system. The clearance between the impeller and the stator varies as the rotor vibrates, creating aerodynamic excitation and a destabilizing cross-coupled force. For this reason, the impeller aerodynamic stiffness is added as a variable into the analysis in this thesis work. Calculation of impeller aerodynamic cross-coupled stiffness is presented in the following chapter 3.1. The rotor dynamic analysis based on the results presented in this chapter are presented in chapter 3.5.

3.4 Aerodynamic cross-coupled stiffness caused by an impeller

Two most common methods, Alford's equation, and Wachel's equation, for obtaining the aerodynamic cross-coupled stiffness caused by an impeller are presented in chapter 2.4. Therefore, two different results are obtained for each impeller. Generally, the result from Alford's equation is used as a lower limit and the result from Wachel's equation is used as an upper limit. (Chen 2005, p. 305) The configuration of an isolated rotor shaft and both impellers are shown in Figure 39.



Figure 39. Rotor shaft with attached impellers in both ends.

Following parameters are used:

- Rotational speed 11000 rpm
- Power 1000 W
- Efficiency factor 2.5
- Blade pitch mean diameter
 - 422.01 mm for LPC
 - 394.00 mm for HPC
- Blade height
 - 80.71 mm for LPC
 - 55.06 mm for HPC

After these parameters are applied to the equations, results for cross-coupled stiffnesses as follows:

- For LPC using Alford's equation 63716 N/m
- For LPC using Wachel's equation 121436 N/m
- For HPC using Alford's equation 100038 N/m
- For HPC using Wachel's equation 270104 N/m

According to these results, it can be estimated that the real cross-coupled stiffness for LPC is between 63716...121436 N/m and for HPC between 100038...270104 N/m for 11000 rpm.

3.5 Rotor dynamic analysis

This chapter presents results of rotor dynamic analysis after including both labyrinth seals and aerodynamic stiffness from both impellers into the rotor dynamic model. The modelling and analysis are made using MATLAB coded Rotor-Bearing Dynamics toolbox presented in chapter 3.6. The results of the model with seal and impeller aerodynamic stiffness are compared to the results of the respective model without them. This way, the effect of seals and impeller aerodynamic stiffness can be analysed. The input parameters used in modelling of the system are presented in Table 10.

Table 10. Input parameters for constructing the rotor-bearing system in Rotor-Bearing Dynamics toolbox.

Rotor properties	
Material	Steel
Elastic modulus	$E = 1.995 \cdot 10^{11}$ Pa
Density	$\rho = 7874$ kg/m ³
Polar moment of inertia	$I_{xx} = 2.1442$ kgm ²
Diameter moments of inertia	$I_{yy} = I_{zz} = 35.1918$ kgm ²
LPC Impeller properties	
Material	Aluminium

Density	$\rho = 2700 \text{ kg/m}^3$
Mass	$m = 9.31 \text{ kg}$
Polar moment of inertia	$I_{xx} = 0.1447 \text{ kgm}^2$
Diameter moments of inertia	$I_{yy} = I_{zz} = 0.0908 \text{ kgm}^2$
Width	0.231 m
Outside diameter	$d_{out} = 0.468 \text{ m}$
Inside diameter	$d_{in} = 0.070 \text{ m}$
HPC Impeller properties	
Material	Aluminium
Density	$\rho = 2700 \text{ kg/m}^3$
Mass	$m = 3.38 \text{ kg}$
Polar moment of inertia	$I_{xx} = 0.0310 \text{ kgm}^2$
Diameter moments of inertia	$I_{yy} = I_{zz} = 0.0195 \text{ kgm}^2$
Width	0.154 m
Outside diameter	$d_{out} = 0.340 \text{ m}$
Inside diameter	$d_{in} = 0.060 \text{ m}$
Bearing properties	
Stiffness	$6.8 \cdot 10^7 \text{ N/m}$
Damping	$1.4 \cdot 10^5 \text{ Ns/m}$
Unbalance masses	
Unbalance at both impellers	0.0001 kgm

A wireframe model of the HT COMP compressor is shown in Figure 40. The system is divided into 35 elements using 36 nodes. In the figure, the dark blue line represents the centre line, the light blue lines represent the outlines, the dotted dark blue lines represent the magnetic bearings, and the red rectangles at both ends represent the impellers. The mass points of the impellers are set to be at nodes 1 and 36. The seals are set to be at nodes 4 and 33. The axial locations of the components can be seen from the figure.

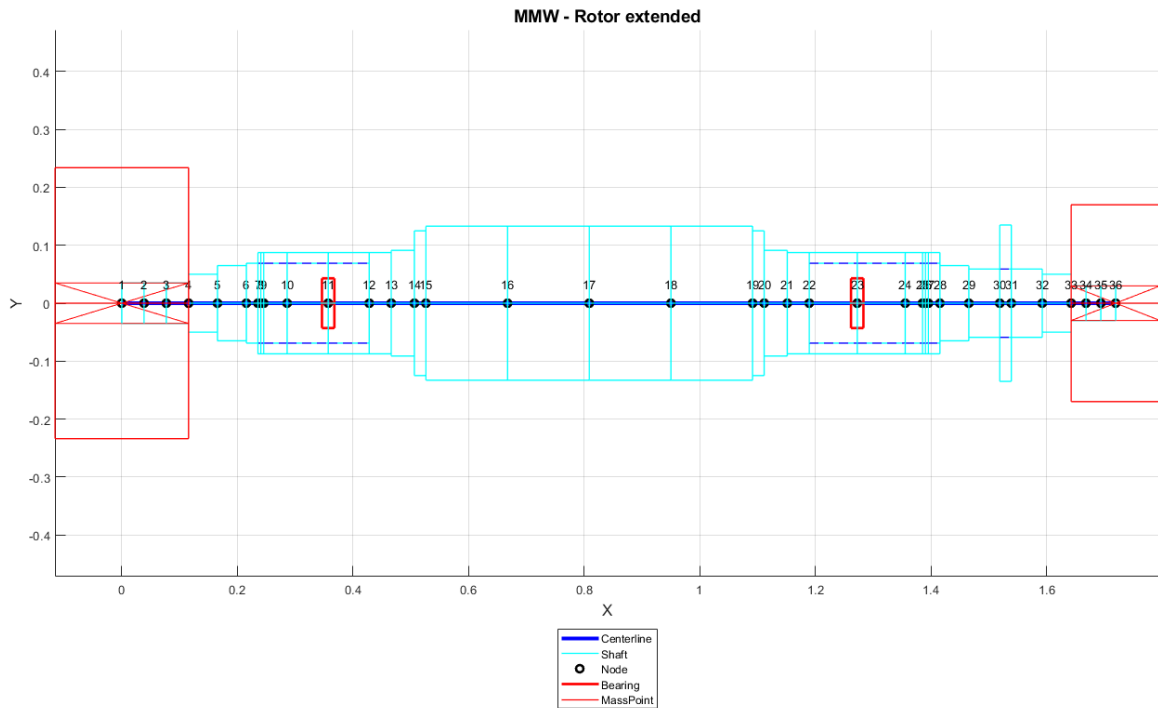


Figure 40. Wireframe model of the HT COMP compressor modelled by the Rotor-Bearing Dynamics tool.

This thesis work focuses on seal effect on rotor dynamics at operational speed of 11,000 rpm using the base values for an axial labyrinth seal presented in chapter 3.1. Therefore, the objects of examination are the natural frequencies and damping ratios at operational speed before and after adding damping and stiffness from seals, and impeller aerodynamic stiffness. Results at any other speed, are not valid results. In this analysis, dynamic coefficients for seals are calculated using Black's method, because it is more accurate with relatively long seals compared to Child's method. Aerodynamic stiffnesses from impellers are calculated using the average number of results from Alford's and Wachel's. These calculations are presented in chapters 3.3 and 3.4.

Figure 41 presents Campbell diagram before adding the new variables, Figure 42 presents Campbell diagram after adding impeller cross-coupled stiffness, and Figure 43 presents Campbell diagram after adding the seals. The light blue and green lines represent the forward and backward whirling modes of the first bending mode. The dark blue and purple lines represent the forward and backward whirling modes of the second bending mode.

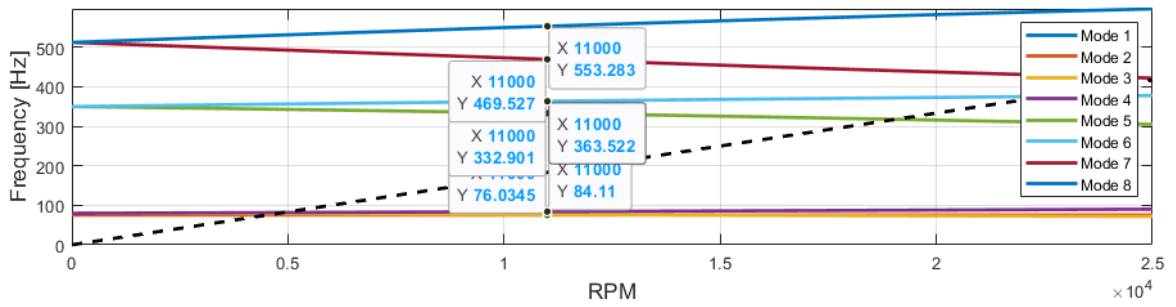


Figure 41. Campbell diagram before adding impeller cross-coupled stiffness and seals.

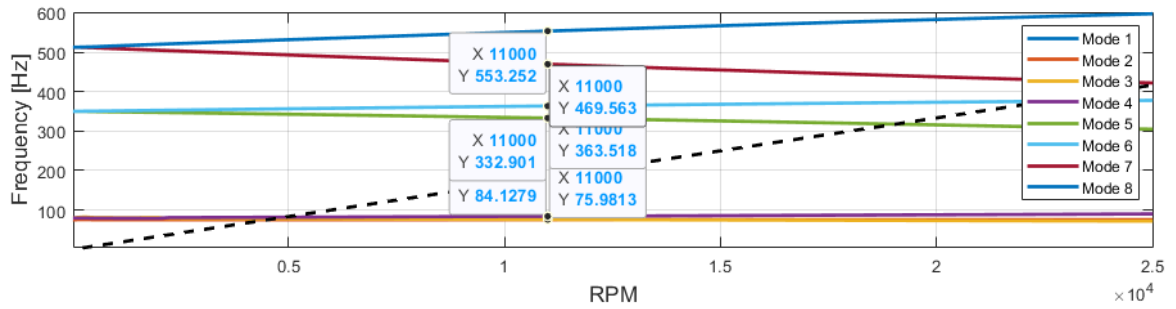


Figure 42. Campbell diagram after adding only impeller cross-coupled stiffness.

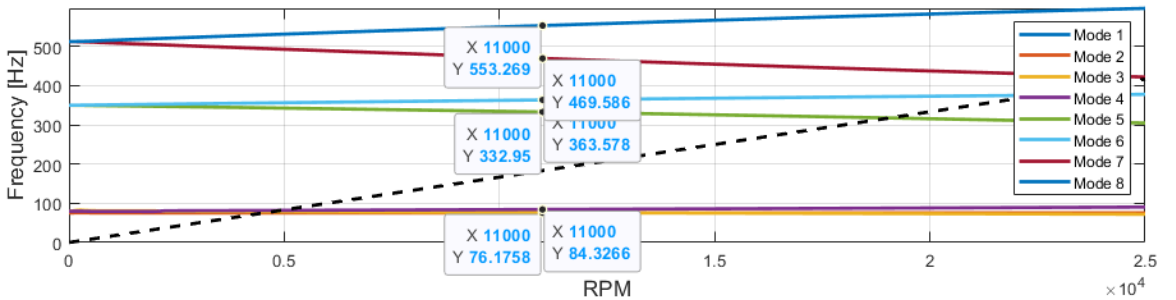


Figure 43. Campbell diagram after adding impeller cross-coupled stiffness and seals.

When compared the Campbell diagram before (Figure 41) and after (Figure 42) the impeller cross-coupled stiffness, the effect of impeller aerodynamic stiffness can be isolated. The natural frequencies of the first bending mode decreased only from 363.522 to 363.518 Hz in its forward whirling mode and stayed the same in its backward whirling mode. In the second bending more, the forward mode decreased from 553.283 to 553.252 Hz and the backward mode increased from 469.527 to 429.563 Hz. The change is approximately between 0....0.001%.

When compared the Campbell diagram after the seals (Figure 43) to the one before the seals (Figure 42), the effect of seals can be isolated. The natural frequencies of the first bending mode increased from 363.518 to 363.578 Hz in its forward whirling mode, and from 332.901

to 332.950 Hz in its backward whirling mode. In the second bending mode, the forward mode increased from 553.252 to 553.269 Hz and the backward mode from 469.563 to 469.586 Hz. The change is approximately between 0.003...0.020%.

The effects of the new variables to damping ratios are presented in Figures 44, 45, and 46. Figure 44 presents damping ratios before the new variables, Figure 45 presents damping ratios after adding the impeller aerodynamic stiffness, and Figure 46 presents damping ratios after adding seals.

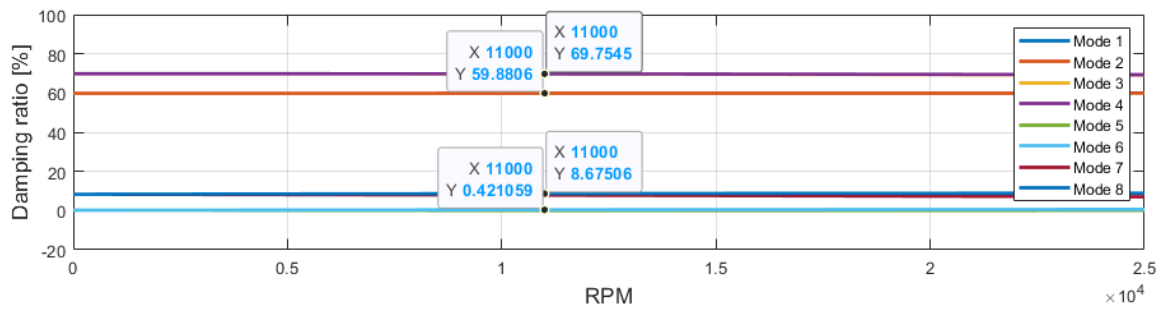


Figure 44. Damping ratios before adding before adding impeller cross-coupled stiffness and seals.

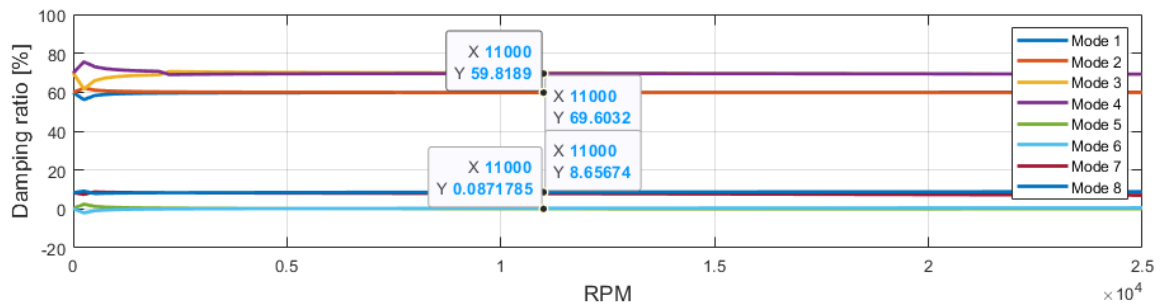


Figure 45. Damping ratios after adding only impeller cross-coupled stiffness.

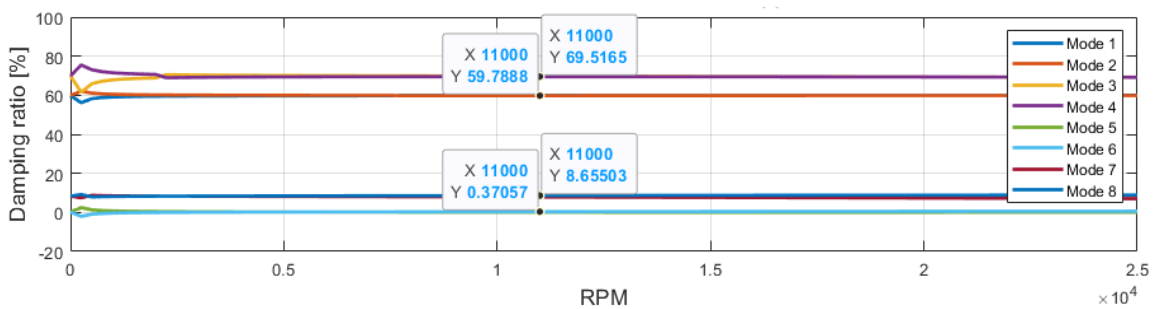


Figure 46. Damping ratios after adding both impeller cross-coupled stiffness and seals.

From figures 44 and 45 it can be seen that the damping ratios decrease by approximately 0.1...0.2% after the impeller aerodynamic stiffnesses are added. From figures 46 and 45 it can be seen that the damping ratios decrease by approximately 0.02...0.12% after the seals are added.

Figure 47 presents Campbell diagram and damping ratios for a scenario, where the maximum aerodynamic stiffness is calculated using Wachel's method as presented in chapter 3.4. Comparing figure 47 to figure 44, the change in natural frequencies and damping ratios can be seen, when impeller aerodynamic stiffness is increased about 40%. The change in natural frequencies in the forward whirling modes is approximately 0.01% and for the backward whirling modes, 0.02%. The change in damping ratios is approximately 0.67% in the forward whirling mode the second bending mode, and between 0.31...0.34% in the rest of the bending modes.

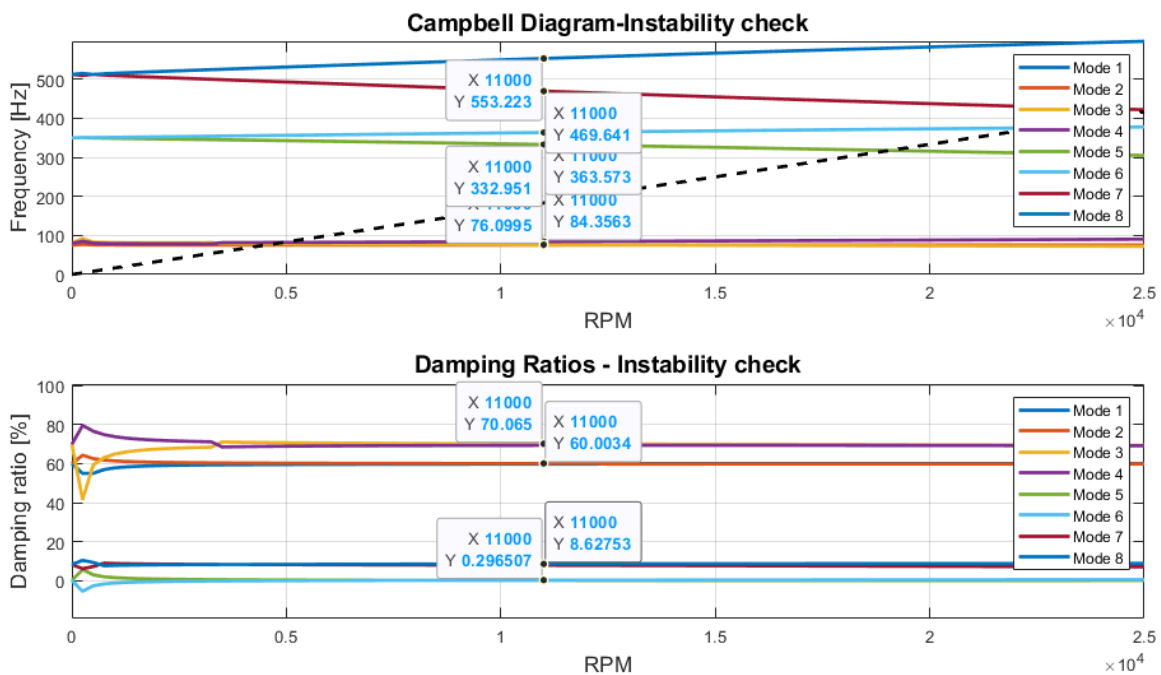


Figure 47. Campbell diagram and damping ratios calculated with maximum impeller aerodynamic stiffness.

Figure 48 presents Campbell diagram and damping ratios using the minimum values for dynamic coefficients for the seals from tables 8 and 9, and figure 49 presents the same results using the maximum values. Comparing these figures, the change in natural frequencies and damping ratios can be seen, when seal length is changed from 15...45 mm and seal clearance from 0.1...1.0 mm. The changes in natural frequencies in the first bending mode is

approximately 0.04%, and 0.01% in the second bending mode. The changes in damping ratios are approximately between 0.1...0.3%.

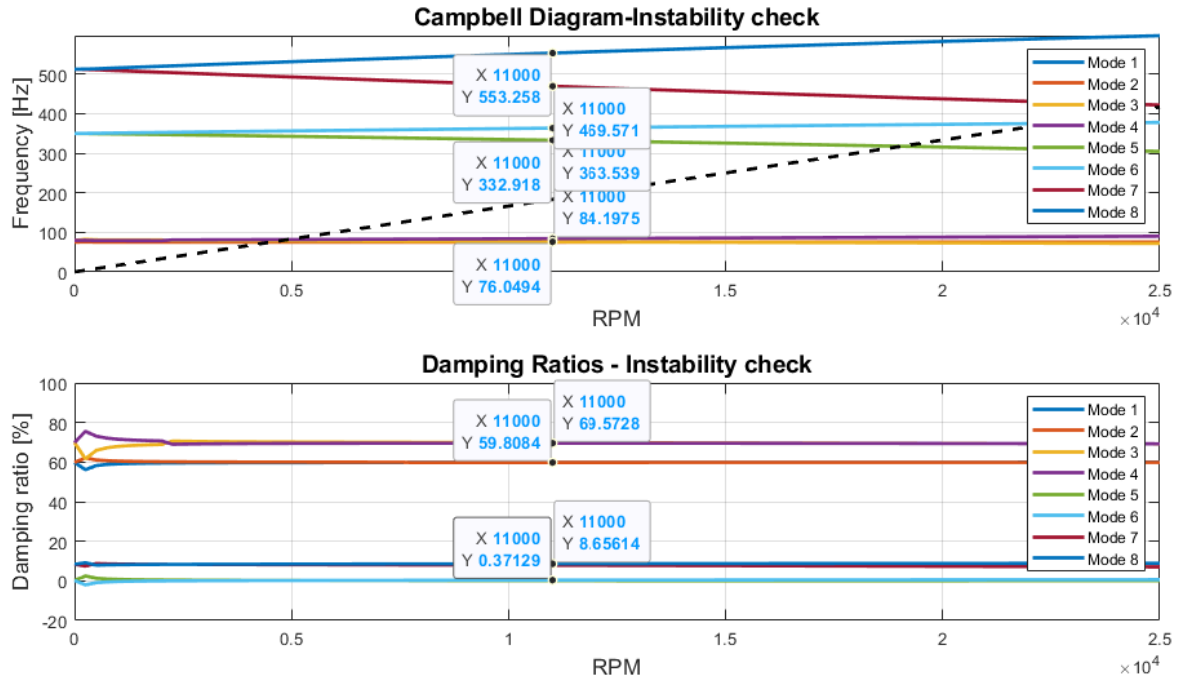


Figure 48. Campbell diagram and damping ratios calculated with minimal seal coefficients.

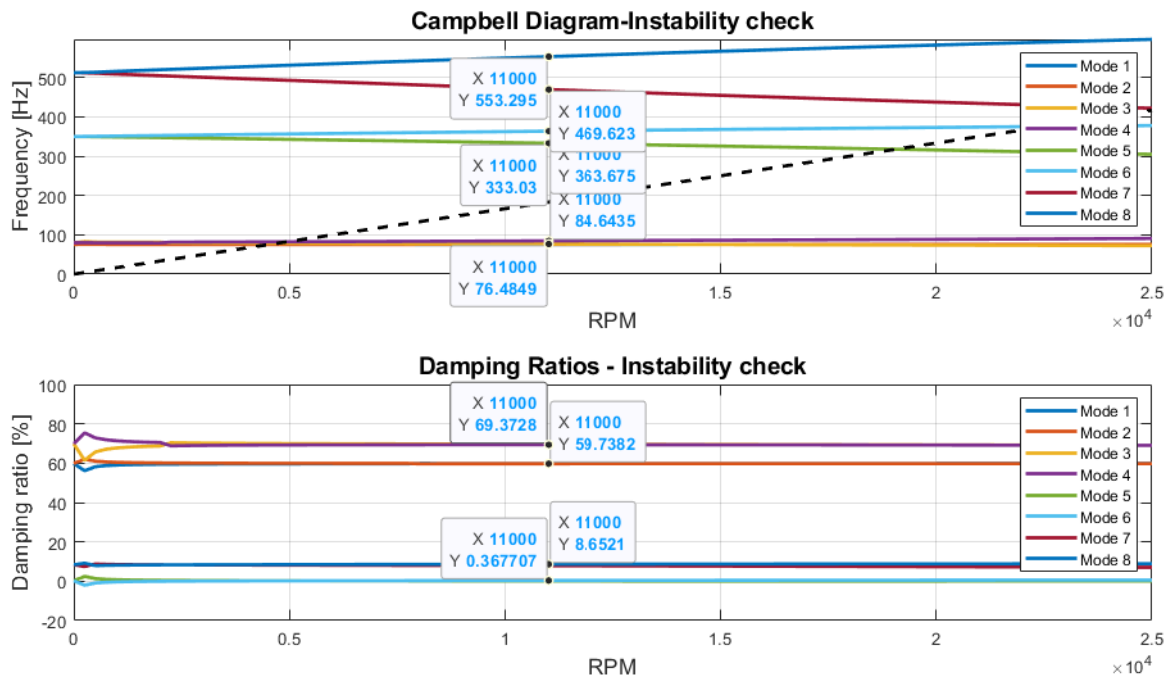


Figure 49. Campbell diagram and damping ratios calculated with maximum seal coefficients.

It can be concluded that the effect of aerodynamic stiffness in this example case, is small. Even though the different calculation methods give results, which differ considerably, the

value is not overly sensitive to the outcome in rotor dynamic analysis. When the value of impeller aerodynamic stiffness was increased by 40%, the natural frequencies changed only for 0.01...0.02% and damping ratios for 0.31...0.67%, approximately. The effect of seals in this example case can also be concluded as small. According to calculation methods presented in chapter 2.3, the only seal parameters which affect to its dynamic coefficients are its length and clearance. When used the minimum and maximum values of dynamic coefficients for seals, when the seal length varied from 15...45 mm and clearance from 0.1...1.0 mm, the natural frequencies changed only for 0.01...0.04% and damping ratios for 0.1...0.3%, approximately.

3.6 Effect of radial seal placement on axial forces

Axial thrust forces are calculated using the methods presented in chapter 2.6. The forces are calculated using seven different radii for the seal for both LPC and HPC. Base values for the seal are presented in chapter 3.1 and only those values are used in this calculation, therefore only the seal radius is a changing variable. Different radii for the seal are 50, 75, 100, 125, 150, 175 and 200 mm for both LPC and HPC. These radii approximately cover the space between the shaft and the impeller outlet radius.

First the axial thrust forces caused by the shroud, the back disc and impulse are calculated. Then the total axial thrust force is calculated by subtracting the back disc force from the sum of shroud and impulse forces. Then, the total axial thrust forces caused by LPC and HPC are summed together to obtain the *net* axial force of the whole compressor. Since the impellers are facing opposite directions, they also create opposing axial forces balancing the net axial force as shown in Figure 50.

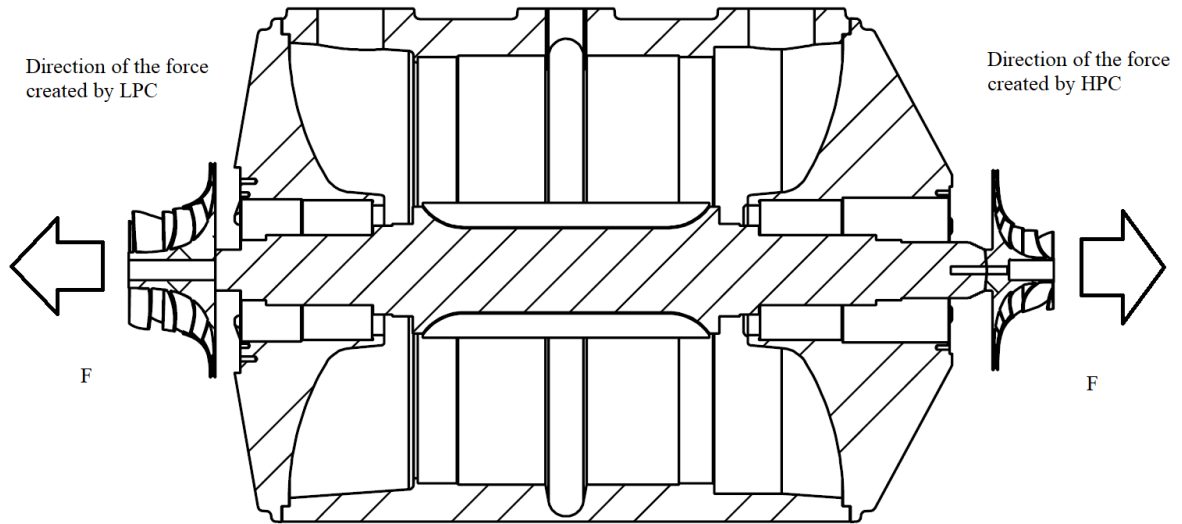


Figure 50. Cross-section view of the motor-compressor configuration with two impellers.

In HT COMP project, the net axial force is the interesting value. Net axial force cannot exceed the amount of axial force, which the axial support bearing can withstand. The net axial force is then plotted against the amount of leakage using the same variables of seal radii to compare seal radius' effect on net axial thrust and leakage. The results for HPC and LPC are presented in Tables 11 and 12.

Table 11. Axial forces for HPC.

Seal radius (mm)	Net axial thrust (N)	Axial thrust on shroud side (N)	Axial thrust at back disc side (N)	Impulse force (N)
No seal	-15280	54193	-69900	427
50	-14958	54193	-69578	427
75	-13721	54193	-68341	427
100	-11979	54193	-66598	427
125	-9934	54193	-64554	427
150	-7277	54193	-61897	427
175	-4223	54193	-58843	427
200	-1413	54193	-56033	427

Table 12. Axial forces for LPC.

Seal radius (mm)	Net axial thrust (N)	Axial thrust on shroud side (N)	Axial thrust at back disc side (N)	Impulse force (N)
No seal	-4070	11766	-16352	517
50	-4086	11766	-16368	517
75	-4139	11766	-16421	517
100	-4207	11766	-16490	517
125	-4308	11766	-16590	517
150	-4458	11766	-16741	517
175	-4637	11766	-16920	517
200	-4922	11766	-17204	517

The following four figures show the results for HPC and LPC in a visual form. From Figures 51 and 52, it can be observed that the leakage increases linearly as the seal radius increases. This is because in equation 6 by Kearton, the cross-section area A_l is a multiplying factor for the mass flow q_m and r is a multiplying factor for the cross-section area. Therefore, by doubling or halving the radius, the leakage mass flow doubles, or halves respectively. It is important to note, that this is a simplified model, in respect that the rotation speed is not taken into account. The surface speed increases as the radius increases, meaning that the flow would have more rotational speed as the seal radius increases. The effect of rotation speed is thought to be negligible, but it does have some effect. It is generally thought that high speed makes the flow more turbulent, and therefore reduces the leakage flow.

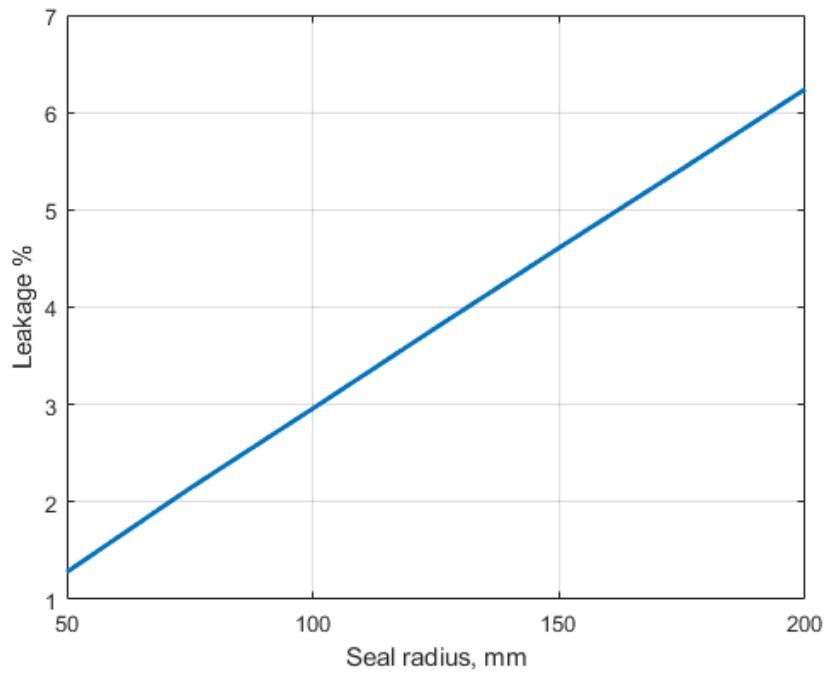


Figure 51. Seal radius effect on leakage in HPC.

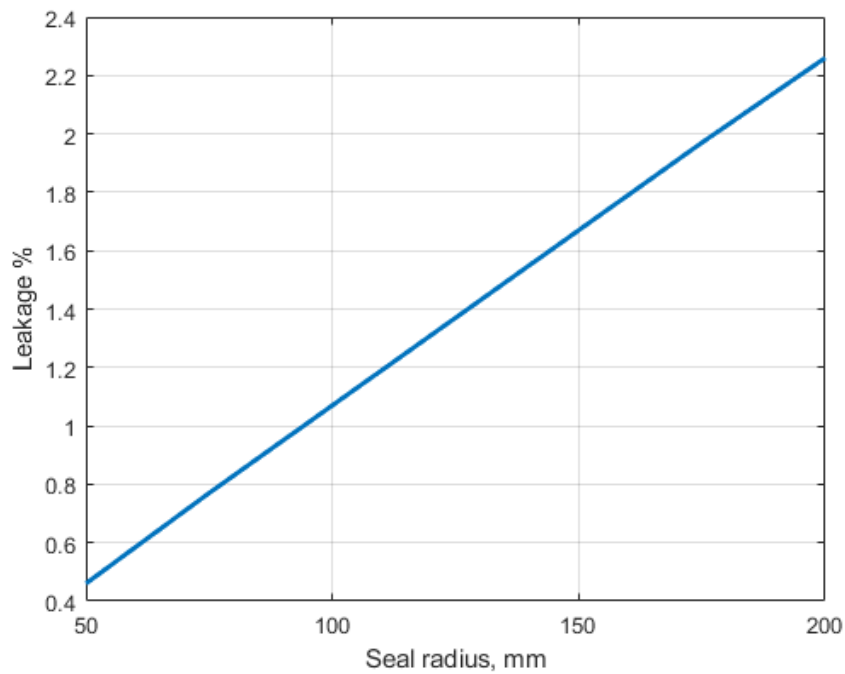


Figure 52. Seal radius effect on leakage in LPC.

The impellers at the opposite ends of the rotor shaft are faced the opposite ways, creating axial forces, which compensate for each other. Figure 53 shows the net axial forces of the whole compressor system, where the two forces created by individual impellers are added

together. From the figure it can be seen, that as the seal radius of both impellers simultaneously increases, the total net axial force decreases. The behaviour of the line is closer to linear than exponential, but it is clearly not linear either. The reason, why the total net axial force decreases as the seal radius increases, is the following: the larger the high-pressure volume between the impeller and the back disc, the more it creates push in axial direction. The radial seal divides the volume between the back side of the impeller and back disc to a low-pressure section and a high-pressure section. The closer the seal is to the shaft, the smaller is the low-pressure section, and the larger is the high-pressure section.

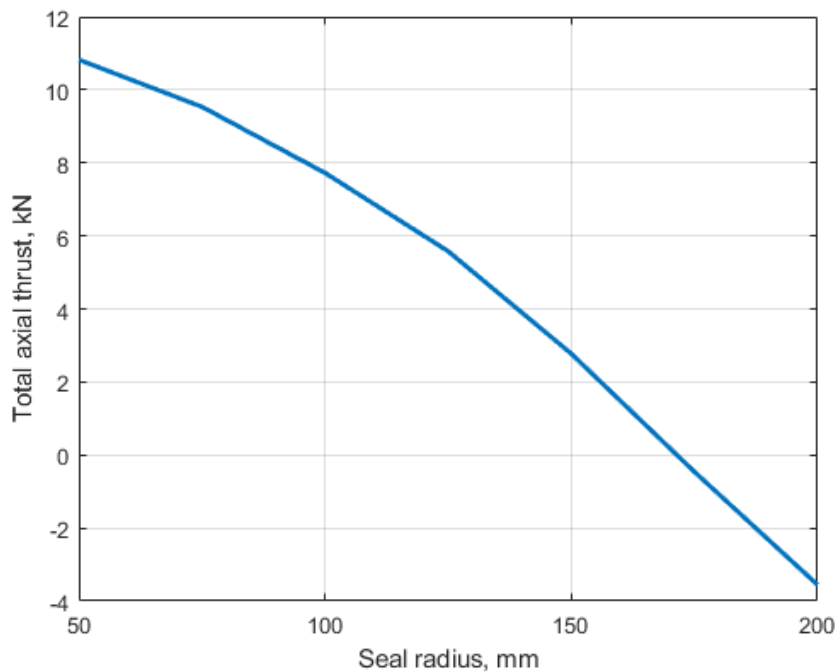


Figure 53. Seal radius effect on net axial thrust of the whole compressor.

There are also other axial forces in the system in addition to the force created in between the impeller and the back disc. The impellers themselves create axial forces. This is why, the total net axial force goes to negative value instead of zero, when the seal radius goes to maximum value. In this case, by having some high-pressure volume between the impeller and the back disc, meaning the seal is not completely at the outer edge, the total net axial force is actually closer to zero. From Figure 53, it can be observed, that in order to achieve 0 total net axial force, the radial seal should have approximately 170 mm radius, instead of 200 mm.

From Figure 54, the seal radius effect on leakage and net axial forces can be observed simultaneously. The decision regarding the use of a radial seal in the project, should be made by analysing this figure. From the figure, it can be observed that the leakage of HPC ranges approximately between 1.3...6.1%, the leakage of LPC ranges approximately between 0.5...2.3%, and the net axial force ranges between 11...-3.5 kN. The leakage numbers seem relatively high, as the leakage is directly affected to the overall efficiency of the system. In order to maximize efficiency, as small radius as possible should be considered. The downside for smallest possible radius is an axial force of 11 kN, which then needs to be supported by an axial bearing.

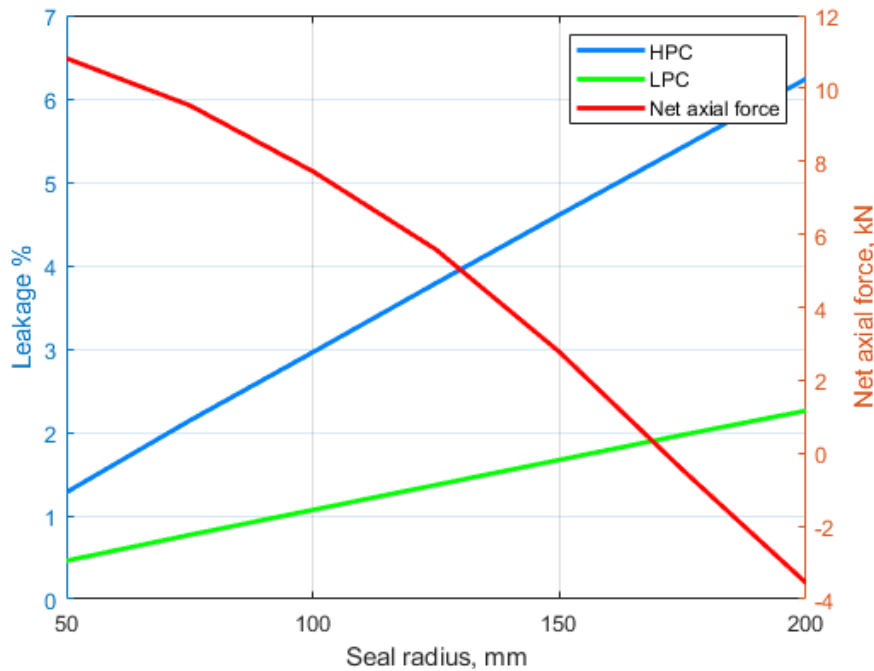


Figure 54. Seal radius effect on axial thrust and leakage.

As a conclusion, if a radial seal is selected to be used, it should be placed as close as possible to the shaft for minimizing leakage, and a strong enough axial support bearing should be selected to withstand an axial force of 11 kN together with an appropriate safety margin.

4 Discussion

This chapter is focused on analysing results presented in previous chapter. Seal leakage can be obtained by analytical, computational, or empirical methods. In this thesis work, results are obtained using computational and analytical methods. In a machine design process, it is natural to use analytical and computational methods before creating the actual physical machine, but only after physical empirical tests, computational and analytical methods can be completely verified.

4.1 Leakage optimization

When analytical methods are compared, certain weaknesses are found in them. As presented in equation 1, Martin's equation assumes that the theoretical discharge area is the same as the actual discharge area and that all kinetic energy dissolves in each labyrinth chamber before moving on to the next chamber. Because of these assumptions, Martin's method tends to overestimate the leakage flow. It can be seen that in every calculation, leakage flow obtained by Martin's method is the highest, and therefore probably also higher than in reality.

Unlike Martin's method, Kearton's equation, as presented in equation 6, considers that the actual discharge area is smaller than the theoretical discharge area and therefore uses a discharge coefficient C_d , which is always < 1 . Unlike Egli, Kearton also assumes that all kinetic energy dissolves in each labyrinth chamber before moving on to the next chamber, whereas in reality, only a fraction of the kinetic energy dissolves in a single chamber. For this correction, Egli uses a kinetic energy carryover coefficient ε , which is always ≥ 1 . It seems that for this reason, Kearton's equation tends to underestimate the leakage flow, as can be seen from the results. In every calculation, leakage flow obtained by Kearton's equation is significantly lower than those of CFD or Martin's equation.

In radial seal results, it can be observed that Martin's method showed same leakage with all three different values for blade height, chamber width, blade width, and blade shape, meaning it does not take these variables into account in its equation. It only gave different results when calculated with varying blade number, seal radius and seal clearance. For this

reason, Martin's method is not a reliable tool when optimizing geometry of a labyrinth seal. Because of its lack of kinetic energy carryover coefficient, it gives the same leakage result for a half labyrinth and full labyrinth with otherwise identical geometries and values.

Kearnton's method resulted same leakage with all different values for blade height and blade shape. Compared to Martin's method, Kearnton's method takes more factors into account, but it does not include some particularly crucial factors such as the kinetic energy carryover coefficient. Because of this reason, it should not be used alone as an optimizing tool for labyrinth seal geometries and values. As radial seal results, CFD includes most factors and by observing that for each variable, it gives different results for different values.

Egli's method takes into account both, kinetic energy carryover and actual discharge area. Because of this, results by Egli's methods vary between different blade shapes, such as the full labyrinth and half labyrinth. Full labyrinth is considered as an ideal seal, where kinetic energy completely dissipates in labyrinth cavities, giving the full labyrinth a kinetic energy carryover coefficient of 1. For rectangular, spike and fishbone shapes, the coefficient is estimated, making in prone to human estimation error.

Egli's method in axial case gave varying results for all variables for every three different values, except for blade height, where the results were the same for every three values. This is because blade height is not taken into account in Egli's method. However, the effect is relatively small when results are observed by CFD, from 0.316...0.306%. When reviewed blade width's effect on leakage, Egli's method and CFD gave contradictory results. This is because in Egli's method, flow coefficient α slightly increases as blade width increases, and when chamber remains the same, it assumes the blade takes space from the chamber making it smaller, resulting in slightly more leakage. This is probably true in real life with a rectangular shape, but with inclined blade shape, the increased blade width does not effectively take space from the chamber. Egli's equation does not take into account blade shape. CFD results gave virtually no change in leakage when blade width is changed, when inclined shape is used. Overall Egli's method seems to be relatively accurate, at least compared to Martin's or Kearnton's methods, since it takes into account the most important factors.

For a labyrinth seal designer, these results mean the focus should be optimizing the major and moderate effects and ignoring the minor effects. For axial seal, full labyrinth is not

usually an option since it is extremely complicated to assemble. In axial seal case, the focus should therefore be in optimizing clearance, chamber width and number of blades. Clearance should be set as low as possible while preventing collision between seal counterparts. The worst-case scenario should be calculated from tolerances and added with a reasonable safety margin. Chamber width and number of blades both increase the axial length of the shaft. They should be reviewed together with a rotor dynamic stability review.

For a radial seal, the designer should first decide whether to design a full or a half labyrinth seal, what is the radial placement and how small clearance can be achieved safely using worst-case tolerances and a safety margin. These factors will largely dictate the leakage in a radial seal case. In a radial seal, increasing chamber width and number of blades may be easier than in axial, since the increase does not necessarily require longer shaft or larger rotating part.

The seal fails if the counterparts collide. The worst-case position means the position where the counterparts would theoretically be as close to each other as possible, according to tolerances. This can be complicated to calculate. The tolerance chain between the counterparts may include the rotating part, the shaft, bearings, and the stationary part. Also, the connection of these parts should be considered. For a radial seal, the further away the seal is from the shaft, the longer the tolerance chain is.

A crucial factor to consider is the axial thermal expansion of the shaft. In a centrifugal compressor, the axial bearing, which acts as an axial support, is located at one side of the motor. For this reason, the axial thermal expansion is multiple times larger in one compressor side. For steel, the thermal expansion is about $12\text{ }\mu\text{m}$ per meter for every degree $^{\circ}\text{C}$. For example, if the distance between the axial bearing and the seal located at the opposite side of the motor is 1 meter and the temperature range is $100\text{ }^{\circ}\text{C}$, the axial thermal expansion would be approximately 1.2 mm. Considering how sensitive the clearance is to the leakage, a clearance variation of 1.2 mm is not acceptable. This example is simplified so that the thermal expansion of the stationary counterpart is not taken into account. The stationary parts also have thermal expansion, which decreases the total effect in clearance variation. This only applies to axial clearance, which is only the case of a radial seal. In axial or stepped seal, the thermal expansion effect to leakage is only a fraction of the radial seal, because the clearance is in radial direction, and it varies as a function of shaft diameter, which is only a fraction of the shaft length. In axial or stepped seal, the most variation

happens therefore in the chamber length and blade width, if these are machined to the shaft, and not to the stationary part. As concluded in results chapter, these two variables are not as critical to leakage as clearance. Therefore, considering axial thermal expansion of the shaft, axial and stepped seals are much safer than a radial seal.

One popular labyrinth seal design option is a stepped labyrinth seal. This thesis work did not include stepped labyrinth seals into calculations, but rather used half and full labyrinth seals and different blade shapes. A problem with a radial seal is the thermal expansion effect to clearance as explained chapter 4.2, and a full labyrinth seal is usually used only in radial direction, because of its difficulty to assemble in axial case. The efficiency of a stepped labyrinth seal is considered to be somewhere between the half and full labyrinth seals. It makes the fluid flow path more complicated compared to half labyrinth seal, but less complicated than full labyrinth seal. A stepped labyrinth seal does not have the axial thermal expansion problem as does a radial seal. The clearance in a stepped labyrinth seal is in radial direction, which makes the thermal expansion effect small, but at the same time it is more efficient than half labyrinth seal, and it is possible to assemble axially, unlike a full labyrinth seal. Therefore, a stepped labyrinth may be a superior option in some cases.

The reliability and sensitivity of the results depend on what is examined. The absolute leakage values obtained using different methods vary relatively much. For example, the leakage calculated with Egli's method for an axial seal using base values was 0.019 kg/s, while using CFD, the result was 0.024 kg/s. The difference is approximately 20%. But when examining the effect of change in different variables, the slope is relatively constant. For example, using the previous case, when changing the number of blades from 7 to 13, the leakage reduces to 86% of the original using Egli's method, and to 79% using CFD. Therefore, the reliability and sensitivity of the relative effect to leakage of different variables is good, while the reliability and sensitivity of absolute leakage values is not.

When estimating the accuracy of the study, it is important to note all the assumptions made in calculations. The results are obtained using calculations, which assume for example, that there is no rotation of shaft, the pressure difference between the labyrinth chambers is exactly 0.8, and the speed of the flow inside the seal never exceeds the speed of sound. Also, some coefficients are obtained not by accurate calculations, but by estimating a cross-section of a chart with a human eye, which creates margin for error. For these reasons, the accuracy of the obtained absolute leakage values is not highly accurate. The results could be verified

using empirical measurement, but it is not inside the scope of this study. Empirical measurements could then be compared to all methods and find the most accurate ones for future use. The validity of the study is relatively good, since in both axial and radial cases, three independent methods were used to obtain results.

4.2 Rotor dynamic analysis

There are many parameters, which affect the efficiency of an axial labyrinth seal, but only seal length and seal clearance are considered, when calculating rotor dynamic coefficients using Black's and Child's methods. From the results presented in chapter 3.3, it can be seen that the smaller the clearance and the longer the seal, the more it stiffens and dampens the system. In other words, the more efficient the seal, the higher stiffness and damping it gives. As can be seen from table 7 in chapter 3.2.2, the most important variables to affect leakage in an axial seal are its clearance, blade shape and the number of blades. Increasing the number of blades increases the length of the seal, therefore seal length is a valid variable when calculating rotor dynamic coefficients. Seal clearance and length are important parameters in defining seal efficiency, but there are also other moderately effecting variables such as blade shape and chamber width, which are excluded in Black's and Child's methods. To get more accurate results, these variables should be included as well, as they moderately affect seal efficiency, and seal efficiency directly affects the values of dynamic coefficients.

The effect of change in seal length and clearance is not linear with all dynamic coefficients. As can be seen from table 8 in chapter 3.3 for example, when seal clearance is decreased from 0.2 to 0.1 mm, cross-coupled stiffness, and direct damping from more than double. When the clearance is decreased the same amount of 0.1 mm, but from 1.0 to 0.9 mm, cross-coupled stiffness, and direct damping increase only for 8% approximately. The leakage, which correlates with efficiency, linearly changes as the clearance changes as can be seen in figure 18 in chapter 3.2.2. This finding of seal clearance affecting certain rotor dynamic coefficient exponentially, but efficiency only linearly at low clearances, is important. When designing a system, where the rotor dynamic effect of seals is considerable, it would be important to note that when minimizing clearance for maximum efficiency, only a small efficiency increase might multiply the rotor dynamic effect. Therefore, a compromise should be found between optimal seal efficiency and rotor dynamic effect.

When seal length is increased from 15 to 18 mm, direct stiffness increases from 30175 to 38140 N/m, and when seal length is increased from 42 to 45 mm, direct stiffness increases only from 70753 to 71135 N/m. Also with seal length, the effect is not linear, but not as exponential as with seal clearance. It is also important to note, that clearance increase from 0.1 to 0.2 doubles it, whereas seal length increase from 15 to 18 mm, increases it only by a fifth.

To obtain a broader perspective of the seal and impeller aerodynamic stiffness effect on rotor dynamics, the seal dynamic coefficients and impeller aerodynamic stiffness should be calculated as a function of rotation speed. All seal dynamic coefficients and impeller aerodynamic stiffnesses change as the rotational speed changes. Campbell figures presented in chapter 3.5 show accurate results only at operational speed of 11,000 rpm. Therefore, the Campbell diagrams cannot be interpreted by analysing behaviour at different speeds. The Campbell figures in chapter 3.5 show accurate change in natural frequencies and damping ratios at operational speed, but it does not show how added variables affect critical speeds. Therefore, in order to obtain a broader rotor dynamic picture, including changes in critical speeds, rotational speed change should be applied to calculations.

The comparison between the Black's and Child's methods, and their effect on the shapes of the curves and lines are analysed in depth in chapter 3.3 with visual charts. Child's method assumes that the seal is short, which means that the results are accurate only at low seal lengths. Black's method takes into account seal length and is therefore more accurate as seal length increases. Child's method is based in Gerald Hirs' lubrication equation, where fluid inertia terms are included in the equation. Also in Child's method, the inlet swirl changes as a function of axial velocity, whereas in Black's method, the inlet swirl is always 0.5. The differences between the methods are considerable. The results obtained by Black's and Child's methods vary considerably in absolute values and also in relative changes. Therefore, the reliability and sensitivity of the absolute values are not highly accurate. Calculating seal dynamic coefficients, a large safety margin should be used, or calculate minimum and maximum values and conduct two different rotor dynamic reviews using two different scenarios.

Impeller aerodynamic cross-coupled stiffness is calculated using Alford's method as a minimum value and Wachel's method as a maximum value, as presented in Chen 2005, p. 305. Using the average value of these methods is not a very scientific approach. There are

several main differences between these methods. Alford's method uses an efficiency factor β which is user-defined based on whether the impeller is axial, radial, shrouded, unshrouded, or over-hung. Wachel's method does not use an efficiency factor, but instead takes into account fluid molecular weight and fluid density difference at suction and discharge. Because of these differences, Alford's method is more sensitive to change of machine type or setup, whereas Wachel's method is more sensitive to change in fluid properties. A designer should consider these changes and perhaps rely more on the method, which shows sensitivity to the uniqueness of the system. For example, if the system has an overhung unshrouded impeller, it would be smart to pay more attention to Alford's method. If the fluid of the system is rare or special and its properties deviate from typical fluids used in these kinds of systems, Wachel's method should be preferred. Since there is a significant difference between the results obtained by Alford's and Wachel's methods, the reliability and sensitivity of the absolute values of the results are not highly accurate. Maximum and minimum possibilities should be calculated, and two different rotor dynamic reviews should be conducted, for worst-case and best-case scenarios.

Even though the reliability and sensitivity of the methods, meaning the correctness of the absolute values of the rotor dynamic results, is not highly accurate, the validity, meaning whether or not the methods measure the correct underlying phenomenon, is relatively good. Seal dynamic coefficients and impeller aerodynamic stiffnesses are calculated using more than one method to increase the validity of the results. The results could be verified using empirical measurement, but it is not inside the scope of this study. In empiric testing, two or more different seals and impellers could be used with otherwise identical setup. The change between the results could be compared to calculated results to verify them.

4.3 Effect of radial seal placement on axial forces

When considering a radial labyrinth seal, the calculation of axial forces is important for choosing an axial bearing of a correct size. Using an axial bearing which cannot withstand the forces, results in failure. On the other hand, over-dimensioning an axial bearing increases the costs and possibly size of the system without any benefits.

For a designer designing a radial labyrinth seal, an important consideration is whether to minimize the leakage to absolute minimum at a cost of maximizing axial forces or find a

compromise between these two contradictory properties. As the leakage is closely and inversely correlated with the overall efficiency of the machine, minimizing leakage saves operational costs, but might increase the one-time production cost of the system, because a stronger axial bearing is needed. Depending on customer values, maximizing efficiency might be a smarter option.

5 Conclusions

This thesis work has studied the effect of different labyrinth seal geometries and properties to leakage and rotor dynamics. In addition, the effect of impeller aerodynamic cross-coupled stiffness to rotor dynamics, and the relationship between axial forces and leakage in a radial labyrinth seal case, have been studied.

To obtain the relationship between different seal geometries and leakage, a number of calculations were made. Seal calculations were made using four different methods: CFD, Martin's, Kearton's, and Egli's methods. Seven different seal variables were used: seal radius, seal clearance, blade width, chamber width, blade height, blade number, and blade shape. All variables were given 3...8 different values and leakage was calculated for every setup by changing one variable at a time. Different results were obtained for total of 22 different setups for a radial seal and for 15 different setups for an axial seal. The results were presented so, that the effect of change in a particular variable was plotted against leakage. The results obtained using all methods were presented in a single chart.

From the results, it was concluded that seal clearance and blade shape have a major effect, chamber width and number of blades have a moderate effect, and blade width and blade height have only a minor effect. For a radial seal, also seal radius has a major effect. The results confirmed the second hypotheses from the leakage point of view: "Seal design variables, such as clearance and seal length, have greater impact on leakage and rotor instability than variables, such as blade width, blade height and chamber width. The impact of the least effective variables is negligible."

To obtain the relationship between different seal geometries and rotor dynamics, first the seal dynamic coefficients were calculated. Four rotor dynamic coefficients were calculated: direct stiffness, direct damping, cross-coupled stiffness, and cross-coupled damping. Calculations of rotor dynamic coefficients were done using two different methods: Black's and Child's methods. Two different seal variables were used: seal length and seal clearance. Seal length was given values between 15...45 mm using a 3 mm increment. Seal clearance was given values between 0.1...1.0 mm using 0.1 increment. This resulted in total of 21 different setups, when one variable was changed at a time. The results were presented so,

that the effect of change of a variable was plotted against the change in a specific dynamic coefficient. The charts presented results obtained using both methods in a single chart.

It was concluded that stiffness and damping increase as the efficiency of the seal increases. This confirms the first hypotheses from axial labyrinth seal point of view: “In a labyrinth seal, leakage optimization is contradictory to rotor instability (in axial seal case) and to axial forces (in radial seal case), meaning that the final design is a compromise between these factors.” An important observation was that the change of some dynamic coefficients is exponential, so that the change is larger at short seal lengths and small clearances compared to long seal lengths and large clearances.

After calculating the seal dynamic coefficients, they were implemented in a rotor-bearing dynamic model using. In the model, natural frequencies and damping ratios were calculated before and after implementing the seals and the impeller aerodynamic cross-coupled stiffnesses. It was concluded that the effect of an axial labyrinth seal to natural frequencies and damping ratios is small. When dynamic seal coefficients were calculated using minimum and maximum values, with seal length between 15...45 mm and seal clearance between 0.1...1.0 mm, the difference in natural frequencies was only between 0.01...0.04%, and the difference in damping ratios was between 0.1...0.3% approximately. The effect of impeller aerodynamic cross-coupled stiffness to natural frequencies and damping ratios was also small. When the value of impeller aerodynamic cross-coupled stiffness was increased by 40%, the natural frequencies changed only for 0.01...0.02% and damping ratios for 0.31...0.67% approximately.

The axial forces created by impellers were calculated for both impellers HPC and LPC using seven different seal radii: 50, 75, 100, 125, 150, 175, and 200 mm. First the axial thrust forces caused by the shroud, the back disc and impulse were calculated. Then the total axial thrust force was calculated by subtracting the back disc force from the sum of shroud and impulse forces. Then, the total opposing axial thrust forces caused by LPC and HPC were summed together to obtain the net axial force of the whole compressor.

Results were presented in a visual chart by plotting seven different radii against the net axial forces of the whole compressor. Then, the already obtained leakage results for different radii were added into the same chart for both LPC and HPC. From the results, it was concluded that as the seal radius increases, axial forces decrease and leakage increase. The opposite

happens as the seal radius decreases. This confirms the first hypotheses from the radial seal point of view. As a conclusion, if a radial seal is selected to be used, it should be placed as close as possible to the shaft for minimizing leakage, and a strong enough axial support bearing should be selected to withstand the axial force together with an appropriate safety margin.

The objectives of the thesis were well achieved. This thesis work gives practical information for a seal designer, which was not well available before: which seal parameters to focus on and how to minimize leakage while paying attention to rotor dynamic effect or axial forces depending on whether the seal is radial or axial. The results of the study were an addition to already studied subjects.

Existing literature presents shortly the impact of different seal variables to leakage. However, it does not present them by examples and results accurately for different data points. It also does not specify whether the change is linear, exponential, or something else. Existing literature also presents methods for calculating seal dynamic coefficients, but it does not present examples of how much different dynamic coefficient change as a function of seal length and clearance, which is presented in this thesis work. The effect of leakage and rotor dynamic coefficients as a function of different seal parameters are a contribution of this work to mechanical engineering and machine dynamics fields.

The limitations of this thesis work are also important to note. First, it is important to note that the results are obtained in the framework of the HT COMP project. The dimensions and input values are unique. The results may change drastically for a different system. The leakage calculations are done using several simplifications.

Further research could be done about calculation of leakage including rotation of the rotor, calculation of dynamic coefficients as a function of rotational speed, empirical tests to verify calculated results, experimenting with different blade shapes for better efficiency, or studying creative ways to increase complexity of the labyrinth seal (for example from half labyrinth to full labyrinth) without making it vulnerable to thermal expansion. Additionally, it would be interesting to study the relationship between leakage of labyrinth seals to overall efficiency of the machine to see whether they are linearly, or some other way correlated.

References

Baha, V., Lishchenko, N., Vanyeyev, S., Mižáková, J., Rodymchenko, T. & Pitel' Ján. 2021. Numerical Simulation of Gas Flow Passing through Slots of Various Shapes in Labyrinth Seals. Frontier, 2021

Tisarev, A., Falaleev S. & Alexandr Vinogradov. 2014. Calculation of Labyrinth Seals in the Secondary Air System of Aircraft Engine. The Open Mechanical Engineering Journal, 2014, no 8, p. 424–430.

Inman, D. J. 2014. Engineering Vibration. Fourth Edition. Pearson Education, Inc. Upper Saddle River, New Jersey, USA.

Ivanova, A. & Moskvicvb, A. 2015. Influence of Geometry on Vortex Configuration and Dimension in LRE Turbopump Labyrinth Seal. Procedia Engineering 106, 2015, p. 126–131.

Cao, L., Si, H., Li, P. & Li, Y. 2017. Labyrinth Seal Design Optimization Based on Quadratic Regression Orthogonal Experiment. Energy and Power Engineering, 2017, no 9, p. 204–215.

Reunanen, A. 1995. Labyrinttitiivistet. Lappeenrannan teknillinen korkeakoulu. Energiatekniikan osasto. Lämpö- ja ympäristötekniikan laitos. Turbokonetekniikan seminaari 1995.

Flitney, R. 2014. Seals and sealing handbook. p. 237 – 267. Elsevier Ltd. Butterworth-Heinemann.

Li, X., Yang, J., Xu, W. 2015. Research and comparison on the leakage and fluid force between the axial and the radial labyrinth seal. *Journal of Mechanical Science and Technology* 29, 2015 p. 4611–4620, National Engineering Research Center of Turbo-generator Vibration, Southeast University, Nanjing, China.

Enomoto, Y. 2017. Steam turbine retrofitting for the life extension of power plants. *Advances in Steam Turbines for Modern Power Plants*. 2017, p. 397–436.

Szymanski, A., Dykas, S. 2019. Evaluation of leakage through labyrinth seals with analytical models. *Scientific Bulletin of the Centre of Informatics - Tricity Academic Supercomputer & Network*, 2019, vol 23, issue 1.

Childs, P. 2014. *Mechanical Design Engineering Handbook*. Elsevier Ltd. Butterworth-Heinemann.

Aslan-zada, F, E., Mammadov, V, A., Dohnal, F. 2013. Brush seals and labyrinth seals in gas turbine applications. *Proceedings of the Institution of Mechanical Engineers, Part A: Journal of Power and Energy*, 2013, volume 227, issue 2, p. 216–230.

Zoll, J. 2009. *Modeling Fluid Flow Using Fluent*. Faculty of the Worcester Polytechnic Institute.

Chen, W., Gunter, E. 2005. *Introduction to Rotor-Bearing Systems*. Trafford Publishing. Victoria, BC, Canada.

Dick, E. 2022. *Fundamentals of Turbomachines*. Second Edition. Fluid Mechanics and Its Applications. Springer.

Prasad, K., Narayanan, G. 2021. Electromagnetic Bearings with Power Electronic Control for High-Speed Rotating Machines: Review, Analysis, and Design Example. Institute of Electrical and Electronics Engineers.

Rosu, A. 2021. Rotor balancing and aligning with active magnetic bearings: a case study of MUSK drivetrain simulator. LUT University.

Uzhegov, N. 2016. Design and Material Selection of High-Speed Rotating Electrical Machines. LUT University.

Wróblewski, W., Fraczek, D., Marugi, K. 2018. Leakage reduction by optimisation of the straight-through labyrinth seal with a honeycomb and alternative land configurations. International Journal of Heat and Mass Transfer.

Dimarogonas, A. D., Paipetis, S. A., Chondros, T. G. 2013. Analytical Methods in Rotor Dynamics. Second edition.

Nayek, B., Das, A. S., Dutt, J. K. 2020. Estimation of Inertial Parameters of a Rigid Rotor Having Dynamic Unbalance on Active Magnetic Bearing.

Williamson, M. 2002. Controlling Gearbox Contamination. Machinery Lubrication. [Referred 3.3.2023]. Available at: <https://www.machinerylubrication.com/Read/273/gearbox-contamination>.

Williams, B. P., Flack, R. D. 1998. Calculation of Rotor Dynamic Coefficients for Labyrinth Seals. Mechanical, Aerospace, and Nuclear Engineering, Rotating Machinery and Controls Laboratory, University of Virginia, Charlottesville.

Tiainen, J., Jaatinen-Värri, A., Grönman, A., Sallinen, P., Honkatukia, J., Hartikainen, T. 2021. Validation of the Axial Thrust Estimation Method for Radial Turbomachines.

LUT internal HT COMP presentation.

Subbarao, P. 2019. Leakage Flows in Turbine Cascades. PowerPoint presentation. [Referred 6.4.2023]. Available at: <https://slideplayer.com/slide/14759947/>.

Sopanen, J. 2019. RoBeDyn v2.2 Theory Manual. LUT Machine Dynamics. May 2019. Lappeenranta, Finland.

Woo, J. 2011. Analysis of Compressible and Incompressible Flows Through See-through Labyrinth Seals. Texas A&M University, p. 2.

Subramanian, S., Prasad, B. 2018. Assessment of Analytical Predictions for Radial Growth of Rotating Labyrinth Seals. Article in International Journal of Turbo and Jet Engine, page 267.

Wang, X. 2010. Vehicle noise and vibration refinement. Woodhead Publishing Limited, p. 180–181.

Usabamatov, R., Bergander, M. 2020. The Fundamental Principles of Gyroscope Theory. Journal of Applied & Computational Mathematics. Research Article, 2020, vol 9:1, 2020, p 1–2.

Appendix 1. Matlab code for leakage of axial seal with Egli's equation

```
% Axial half labyrinth seal leakage mass flow using Egli's equation
% Code by Lauri Rauhala

% 1. Input values

p0=190000; % compressor pressure, Pa
p1=35000; % motor space pressure, Pa
gamma=1.4; % ideal gas Cp/Cv
r=0.025; % seal radius
h=0.0005; % clearance, m
b=0.00077; % blade width
B=0.003; % chamber width
n=10; % number of blades
nyy=2.306*10^-5; % kinematic viscosity of air in 102 celsius temperature, m2/s
d=1.764; % air density with 1.9 bar pressure and 102°C, kg/m3
v=5; % velocity of flow (estimated for initial calculation), m/s
nr=11000; % rotational speed, rpm

% 2. Calculations

A=pi*(r+h)^2-pi*r^2; % total clearance area
v0=1/d; % specific gravity 1/d
d_outer=r*2+h*2; % outside diameter of flow area
d_inner=r*2; % inner diameter of flow area
Dh=(4*(pi*(d_outer^2-d_inner^2))/4)/(pi*(d_outer+d_inner)); % hydraulic
diameter, m
Re=v*Dh/nyy % Reynolds number, unitless
fii=sqrt((1-(p1/p0)^2)/(n+log(p0/p1))); % total expansion factor

% 3. Corrective coefficient from tables

alfa=0.55 % flow coefficient 0.34, from table based h/b and Re
epsilon=sqrt((n/(n-1))/((n/(n-1))-((h/B)/((h/B)+0.02)))); % kinetic energy
transfer coefficient

% 4. Initial mass flow calculation

Qm=epsilon*alfa*A*fii*sqrt(p0/v0) % initial mass flow kg/s

% 5. First iteration

IRE=(2*Qm)/(nyy*pi*2*r) % once iterated Reynolds number
Ialfa=0.63 % once iterated flow coefficient from table with iterated Reynolds
number
IQm=Qm/alfa*Ialfa % once iterated new mass flow, kg/s

% 6. Second iteration

IIRE=(2*IQm)/(nyy*pi*2*r) % second iterated Reynolds number
```

```

IIalfa=0.65 % twice iterated flow coefficient from table with iterated Reynolds
number
IIQm=IQm/Ialfa*IIalfa

% 7. Third iteration

IIIRe=(2*IIQm)/(nyy*pi*2*r) % three times iterated Reynolds number
IIIalfa=0.65 % three times iterated flow coefficient from table with iterated
Reynolds number
IIIQm=IIQm/IIalfa*IIIalfa

% No more accurate alfa found from table so last iteration is accurate

IIIQm=0.0194

```

Appendix 2. Matlab code for leakage of radial seal with Kearton's equation

```
% Radial labyrinth seal leakage mass flow using Kearton's equation
% Code by Lauri Rauhala

% 1. Input values

p0=190000; % compressor side pressure, Pa
p1=35000; % motor side pressure, Pa
n=10; % number of blades
B=0.003; % chamber width, m
b=0.00077; % blade thickness, m
r1=0.1; % from centerline to most outside blade, m
h=0.0005; % clearance, m
R=287.06; % gas constant for air, J/(kg K)
T0=102+273; % temperature, K

% 2. Corrective coefficients from tables

F=0.85872; % estimated from table
Cd=0.9; % total leakage coefficient, estimated from table

% 3. Calculations

A1=2*pi*r1*h; % flow area, m2
fii=n+(2*(B+b)*n*(n-1))/(2*r1-(B+b)*(2*n-1)); % total area coefficient
Qm=Cd*A1*sqrt((F*(p0^2-p1^2))/(R*T0*fii)) % leakage mass flow

Qm=0.0381
```


Appendix 3. Matlab code for leakage of radial seal with Martin's equation

```
% Radial labyrinth seal leakage mass flow using Martin's equation
% (Mechanical Design Engineering Handbook)
% Code by Lauri Rauhala

% 1. Input values

p0=190000; % compressor side pressure, Pa
p1=35000; % motor side pressure, Pa
n=10; % number of blades
B=0.003; % chamber width, m
b=0.00077; % blade thickness, m
r1=0.1; % from centerline to most outside blade, m
h=0.0005; % clearance, m
R=287.06; % gas constant for air, J/(kg K)
T0=102+273; % temperature, K

% 2. Corrective coefficients from tables

F=0.85872; % estimated from table
Cd=0.9; % total leakage coefficient, estimated from table

% 3. Calculations

A1=2*pi*r1*h; % flow area, m2
Qm=A1*p0*sqrt(((1-(p1/p0)^2)/(R*T0*(n-log(p1/p0)))))

Qm=0.0523
```

Appendix 4. Matlab code for axial thrust created by an impeller

```
% CC BY-SA 4.0
% Jonna Tiainen
% Lappeenranta-Lahti University of Technology LUT, Finland
% March 1, 2021

% The hybrid method estimates the net axial thrust of the radial
% turbomachine. Only the data available in the preliminary design stage is
% required as input data. The hybrid method combines the axial thrust
% estimation methods of Japikse (1996) and Larjola (1988), and includes
% improvements to them.

% The hybrid method is validated against the experimental data of the
% centrifugal compressor (unshrouded), radial pump (2D impeller), and two
% gas turbines (consisting of unshrouded centrifugal compressors and
% radial inflow turbines).

% The hybrid method is published as an open access article in 2021 in
% International Journal of Rotating Machinery.
% Link to original published version:
% https://doi.org/10.1155/2021/6669193

% References:
% - Tiainen, J. et al. (2021) Validation of the axial thrust estimation
% method for radial turbomachines. International Journal of Rotating
% Machinery, Volume 2021, Article ID 6669193, p. 18. DOI
% 10.1155/2021/6669193.
% - Japikse, D. (1996) Centrifugal Compressor Design and Performance.
% Wilder (VT): Concepts ETI. p. appr. 500. ISBN 0-933283-03-2.
% - Larjola, J. (1988) Centrifugal compressors, the fundamentals of design.
% (Radiaalikompressorin suunnittelun perusteet, in Finnish).
% Lappeenranta: Lappeenranta University of Technology. Publ. No. EN B-61.
% p. 57. ISBN 951-763-505-2.

% The following lines of code can be used as such to perform the axial
% thrust calculations with Matlab or Octave or you can transfer the
% equations to your preferred tool.

%% List of edits
% Added third, manual option for density input (lines 140-150) and
% calculations (lines 253-256) \\Ahti Jaatinen-Värri, 23.11.2022

%% List of input variables
% The user needs to define the following variables in the section "Input
% data":

% type
% geometry
% shaft
% back
% r1h
% r1s
% r2
% rseal
```

```

% rshaft
% r2bd
% fluid
% rho
% R (not defined, if type == 2)
% gamma (not defined, if type == 2)
% pamb
% Tamb
% p1
% T1
% p2
% T2
% n
% qm
% p0 (only defined, if type >= 3)
% T0 (only defined, if type >= 3)
% pshaft (only defined, if type == 4)
% Tshaft (only defined, if type == 4)
% delta

clc
clear
close all
%% Input data

% Turbomachine type:
% 0 = Centrifugal compressor
% 1 = Centrifugal compressor of the gas turbine (connected to the same
    % shaft with the radial turbine)
% 2 = Radial pump
% 3 = Radial turbine
% 4 = Radial turbine of the gas turbine (connected to the same shaft with
    % the centrifugal compressor)
type = 0; % Fill

% Geometry:
% 2 = 2D impeller
% 3 = 3D impeller
geometry = 3; % Fill

% Shaft configuration:
% 0 = Shaft does not reduce the area of the compressor inlet/turbine outlet
% 1 = Shaft reduces the area of the compressor inlet/turbine outlet
shaft = 0; % Fill

% Back disk configuration:
% 0 = Conventional back disk
% 1 = Scalloped back disk
back = 0; % Fill

% Geometry:
% If turbomachine type is centrifugal compressor or radial pump:
    % r1h [m] = Impeller inlet hub radius (if 2D impeller: r1h = 0)
    % r1s [m] = Impeller inlet shroud radius
    % r2 [m] = Impeller outlet radius
    % rseal [m] = End of the radial labyrinth seal from the shaft direction,
        % (if no labyrinth seal: rseal = 0)

```

```

        % (if no labyrinth seal, but less material in the back disk: rseal = x
and
        % x = end of the less-material-area from the shaft direction)
        % rshaft [m] = Shaft radius
        % r2bd [m] = Outer radius of the scalloped back disk < impeller outlet
radius
% If turbomachine type is radial turbine:
    % r1h [m] = Rotor outlet hub radius
    % r1s [m] = Rotor outlet shroud radius
    % r2 [m] = Rotor inlet radius
    % rseal [m] = End of the radial labyrinth seal from the shaft direction,
        % (if no labyrinth seal: rseal = 0)
        % (if no labyrinth seal, but less material in the back disk: rseal = x
and
        % x = end of the less-material-area from the shaft direction)
        % rshaft [m] = Shaft radius
        % r2bd [m] = Outer radius of the scalloped back disk < rotor inlet radius

r1h = 0.0353 ; % Fill
r1s = 0.1253; % Fill
r2 = 0.2110; % Fill
rseal = 0.47 * r2; % Fill arvioitu hihavakiolla
rshaft = 0.025; % Fill

if back == 0
    r2bd = 0;
elseif back == 1
    %r2bd = ; % Fill or Comment out, if back == 0
end

% Fluid properties:
% 0 = Compressible fluid
% 1 = Incompressible fluid
% 2 = compressible, non-ideal
fluid = 0; % Fill

if fluid == 0
    % Inlet and outlet densities will be calculated using the ideal gas law
elseif fluid == 1
    % Give the density for the incompressible fluid
%     rho = ; % Fill density [kg/m3] or Comment out, if fluid == 0
elseif fluid == 2
    %input inlet and outlet densities in [kg/m3]
    rho1 = 2.60;
    rho2 = 10.24;
end

% Based on your turbomachine type (type), uncomment the corresponding
% section below (lines 143 - 197) and fill the required input data.

if type <= 1 % Centrifugal compressor or centrifugal compressor of the gas
turbine
    R = 55.99; % Fill specific gas constant [J/kgK]
    gamma = 1.0884; % average between inlet and outlet conditions
    pamb = 101; % Fill ambient pressure [kPa]
    Tamb = 293; % Fill ambient temperature [K]
    p1 = 35; % Fill impeller inlet static pressure [kPa]
    T1 = 307; % Fill impeller inlet static temperature [K]

```

```

    p2 = 149; % Fill impeller outlet static pressure [kPa]
    T2 = 359; % Fill impeller outlet static temperature [K]
    n = 11000; % Fill rotational speed [rpm]
    qm = 7.81; % Fill mass flow rate [kg/s]
elseif type == 2 % Radial pump
%     pamb = ; % Fill ambient pressure [kPa]
%     Tamb = ; % Fill ambient temperature [K]
%     p1 = ; % Fill impeller inlet static pressure [kPa]
%     T1 = ; % Fill impeller inlet static temperature [K]
%     p2 = ; % Fill impeller outlet static pressure [kPa]
%     T2 = ; % Fill impeller outlet static temperature [K]
%     n = ; % Fill rotational speed [rpm]
%     qm = ; % Fill mass flow rate [kg/s]
elseif type == 3 % Radial turbine
%     R = ; % Fill specific gas constant [J/kgK]
%     gamma = ; % Fill ratio of specific heat capacities [-]
%     pamb = ; % Fill ambient pressure [kPa]
%     Tamb = ; % Fill ambient temperature [K]
%     p0 = ; % Fill turbine inlet static pressure [kPa]
%     T0 = ; % Fill turbine inlet static temperature [K]
%     p2 = ; % Fill turbine outlet static pressure [kPa]
%     T2 = ; % Fill turbine outlet static temperature [K]
%     n = ; % Fill rotational speed [rpm]
%     qm = ; % Fill mass flow rate [kg/s]
%     p1 = sqrt(p0*p2); % Rotor inlet static pressure [kPa]
%     T1 = T0*(p1/p0)^((gamma-1)/gamma); % Rotor inlet static temperature [K]
elseif type == 4 % Radial turbine of the gas turbine
%     R = ; % Fill specific gas constant [J/kgK]
%     gamma = ; % Fill ratio of specific heat capacities [-]
%     pamb = ; % Fill ambient pressure [kPa]
%     Tamb = ; % Fill ambient temperature [K]
%     p0 = ; % Fill turbine inlet static pressure [kPa]
%     T0 = ; % Fill turbine inlet static temperature [K]
%     p2 = ; % Fill turbine outlet static pressure [kPa]
%     T2 = ; % Fill turbine outlet static temperature [K]
%     n = ; % Fill rotational speed [rpm]
%     qm = ; % Fill mass flow rate [kg/s]
%     pshaft = ; % Fill static pressure behind the back disk at the shaft if
leakage
%     % flow comes from the compressor outlet in the gas turbine (can be
%     % evaluated by estimating the net axial thrust of the centrifugal
%     % compressor of the gas turbine first) [kPa]
%     Tshaft = ; % Fill static temperature behind the back disk at the shaft if
leakage
%     % flow comes from the compressor outlet in the gas turbine (can be
%     % evaluated by estimating the net axial thrust of the centrifugal
%     % compressor of the gas turbine first) [K]
%     p1 = sqrt(p0*p2); % Rotor inlet static pressure [kPa]
%     T1 = T0*(p1/p0)^((gamma-1)/gamma); % Rotor inlet static temperature [K]
end

% Number of data points on the back disk side = delta + 1
% The value of delta can be varied to demonstrate the effect of it on the
% result. The value of 15 is recommended.
delta = 15;

%% Hybrid method
% Calculation of the parameters

```

```

% Diameters
dseal = 2*rseal;
dshaft = 2*rshaft;
if type <= 2
    d1h = 2*r1h;
    d1s = 2*r1s;
    d2 = 2*r2;
elseif type >= 3
    d2h = 2*r1h;
    d2s = 2*r1s;
    d1 = 2*r2;
end

if back == 1
    if type <= 2
        d2bd = 2*r2bd;
    elseif type >= 3
        d1bd = 2*r2bd;
    end
end

% Densities
if fluid == 0
    rho_amb = (pamb.*1000)./(R.*Tamb);
    rho1 = (p1.*1000)./(R.*T1);
    rho2 = (p2.*1000)./(R.*T2);
    if type == 4
        rho_shaft = (pshaft./1000)./(R.*Tshaft);
    end
elseif fluid == 1
    rho1 = rho;
    rho2 = rho;
elseif fluid == 2
    rho1 = rho1;
    rho2 = rho2;
end

% Absolute flow velocities
if geometry == 2
    c1 = qm./(rho1.*pi./4.*(dshaft^2));
elseif geometry == 3
    if type <= 2
        c1 = qm./(rho1.*pi./4.*(d1s^2-d1h^2));
    elseif type >= 3
        c2 = qm./(rho2.*pi./4.*(d2s^2-d2h^2));
    end
end

% Average density
rhos_ave = (rho1+rho2)./2;

% Rotational speed [rps]
n = n/60;

% Angular velocity [rad/s]
omega = 2*pi*n;

```

```

% Fraction on the back disk side
fbd = 0.5;

% Fraction on the shroud side
if type <= 1 || type >= 3
    fs = 0.5;
elseif type == 2
    fs = 0.7;
end

%% Back disk
% Calculation of the back disk pressure distribution

% The method proposed by Larjola (1988) is used to estimate the pressure
% distribution from the impeller outlet to the outer radius of the radial
% labyrinth seal (in the case of the labyrinth seal) or to the shaft.
% Linear reduction in pressure is assumed from the outer radius of the
% labyrinth seal (from the shaft direction) to the shaft.

% Back disk diameter distribution
dbd = zeros(delta+1,1);
for i = 2:delta
    if type <= 2
        if dseal ~= 0
            dbd(1) = dseal;
        elseif dseal == 0
            dbd(1) = dshaft;
        end
        dbd(end) = d2;
    elseif type >= 3
        if back == 0
            bd(1) = d1;
        elseif back ~= 0
            bd(1) = d1bd;
        end
        dbd(end) = dshaft;
    end
    dbd(i) = dbd(i-1)+(dbd(end)-dbd(1))./delta;
end
% Back disk radius distribution
rbd = dbd./2;

% Back disk pressure distribution
pbd = zeros(delta+1,1);
for i = 1:delta
    if type <= 1
        pbd(end,:) = p2.*1000;
        pbd(i,:) = (p2.*1000).*((((gamma-
1)./(2*gamma*(p2.*1000))).*rho2.*fbd.^2.*omega.^2.*(rbd(i).^2-
(d2./2).^2)+1).^(gamma/(gamma-1)));
    elseif type == 2
        pbd(end,:) = p2.*1000;
        % pbd(i,:) = (p2.*1000).*((((gamma-
1)./(2*gamma*(p2.*1000))).*rho2.*fbd.^2.*omega.^2.*(rbd(i).^2-
(d2./2).^2)+1).^(gamma/(gamma-1)));
        % The above equation gives the same result for incompressible flow
        % as this equation:

```

```

        pbd(i,:) = (p2.*1000) + rho2.*fbd.^2.*omega.^2.*0.5*(rbd(i).^2-
(d2./2).^2);
        elseif type == 3
            pbd(end,:) = pamb.*1000;
            pbd(i,:) = (pamb.*1000).*((gamma-
1)./(2*gamma*(pamb.*1000))).*rho_amb.*fbd.^2.*omega.^2.*(rbd(i).^2-
(dshaft./2).^2)+1).^((gamma/(gamma-1)));
        elseif type == 4
            pbd(end,:) = pshaft.*1000;
            pbd(i,:) = (pshaft.*1000).*((gamma-
1)./(2*gamma*(pshaft.*1000))).*rho_shaft.*fbd.^2.*omega.^2.*(rbd(i).^2-
(dshaft./2).^2)+1).^((gamma/(gamma-1)));
        end
    end

if type == 1
    % Calculation of the static temperature distribution on the back disk side
    % The static temperature on the back disk side at the shaft will be
    required
    % when estimating the net axial thrust of the radial turbine of the
    % gas turbine
    Tbd = T2.*(pbd./(p2.*1000)).^((gamma-1)./gamma);
end

% Back disk pressure force distribution
Fbd = zeros(delta,1);
for i = 1:delta
    Fbd(i,:) = (pbd(i,:)+pbd(i+1,:))./2.*pi*(rbd(i+1).^2-rbd(i).^2);
end

% Pressure force at the back disk
if type <= 3
    F_bd1 = sum(Fbd,1);
elseif type == 4
    F_bd1 = (pshaft.*1000).*pi./4.*(d1bd.^2-dshaft.^2);
end

% Linear reduction in static pressure from the end of the seal (from the shaft
% direction) to the shaft
if type <= 1 && shaft == 0
    if p1 <= pamb
        if dseal ~= 0
            F_bd2 = (pamb.*1000+pbd(1,:))./2.*pi./4.*(dseal.^2-dshaft.^2);
        elseif dseal == 0
            F_bd2 = 0;
        end
    elseif p1 > pamb
        if dseal ~= 0
            F_bd2 = (p1.*1000+pbd(1,:))./2.*pi./4.*(dseal.^2-dshaft.^2);
        elseif dseal == 0
            F_bd2 = 0;
        end
    end
elseif type <= 1 && shaft ~= 0
    if dseal ~= 0
        F_bd2 = (pbd(1,:)).*pi./4.*(dseal.^2-dshaft.^2);
    elseif dseal == 0
        F_bd2 = 0;
    end
end

```



```

    end
elseif type == 2
    if dseal ~= 0
        F_bd2 = (pamb.*1000+pbd(1,:))./2.*pi./4.*(dseal.^2-dshaft.^2);
    elseif dseal == 0
        F_bd2 = 0;
    end
elseif type >= 3
    if dseal ~= 0
        F_bd2 = (pamb.*1000+pbd(1,:))./2.*pi./4.*(dseal.^2-dshaft.^2);
    elseif dseal == 0
        F_bd2 = 0;
    end
end

% Pressure force at the back shaft
if type <= 3
    if shaft == 0
        F_bd3 = (pamb.*1000).*pi./4.*dshaft.^2;
    elseif shaft ~= 0
        F_bd3 = 0;
    end
elseif type == 4
    F_bd3 = 0;
end

% Pressure force at the back disk
F_bd = F_bd1 + F_bd2 + F_bd3;

%% Shroud
% Calculation of the shroud pressure distribution

% The method proposed by Japikse (1996).

% Pressure force at the shroud
if type <= 1
    U1t = pi*n.*d1s;
    F_s1 = (0.5.*0.5.*rhos_ave.*(1-
fs^2).*(2*pi*n).^2.*((d2/2).^2+(d1s/2).^2)+(p1.*1000)...
-0.5.*rho1.*(1-fs^2).*U1t.^2).*pi.*((d2/2).^2-(d1s/2).^2);
    p1s = p1.*1000;
    p2s = 0.5.*rho2.*(1-fs^2).*(2*pi*n).^2.*((d2/2).^2)+(p1.*1000)-
0.5.*rho1.*(1-fs^2).*(2*pi*n).^2.*((d1s/2).^2);
elseif type == 2
    ds = zeros(delta+1,1);
    for i = 2:delta
        ds(1) = d1s;
        ds(end) = d2;
        ds(i) = ds(i-1)+(ds(end)-ds(1))./delta;
    end
    rs = ds./2;
    ps = zeros(delta+1,1);
    for i = 1:delta
        ps(end,:) = p2.*1000;
        ps(i,:) = (p2.*1000) + rho2.*fs.^2.*omega.^2.*0.5*(rs(i).^2-
(d2./2).^2);
    end
    p1s = ps(1);

```

```

    p2s = ps(end);
    Fs = zeros(delta,1);
    for i = 1:delta
        Fs(i,:) = (ps(i,:)+ps(i+1,:))./2.*pi*(rs(i+1).^2-rs(i).^2);
    end
    F_s1 = sum(Fs,1);
elseif type >= 3
    p1s = 0;
    p2s = 0;
    F_s1 = 0;
end

% Pressure force at the impeller inlet/rotor outlet
if type <= 1 && shaft == 0
    F_s2 = (p1.*1000).*pi/4*d1s.^2;
elseif type <= 1 && shaft ~= 0
    F_s2 = (p1.*1000).*pi/4*(d1s.^2-d1h.^2);
elseif type == 2
    F_s2 = (p1.*1000).*pi/4*d1s.^2;
elseif type >= 3
    if back == 0
        F_s2 = (p2.*1000).*pi/4*d2s.^2;
    elseif back ~= 0
        F_s2 = (p2.*1000).*pi/4*d1bd.^2; % If r1s > r2bd for turbine
    end
end

% Pressure force at the shroud
F_s = F_s1 + F_s2;

%% Impulse force
if type <= 2
    F_imp = qm.*c1;
elseif type >= 3
    F_imp = -qm.*c2;
end

%% Net axial thrust
F_tot = F_s + F_imp - F_bd; % N

fprintf('Net axial thrust is %3.0f N (positive direction from the shroud
towards the back disk).\n',F_tot);
fprintf('Axial thrust on the shroud side is %3.0f N (positive direction from
the shroud towards the back disk).\n',F_s);
fprintf('Axial thrust on the back disk side is %3.0f N (positive direction from
the shroud towards the back disk).\n',-F_bd);
fprintf('Impulse force is %3.0f N (positive direction from the shroud towards
the back disk).\n',F_imp);

if type == 1
    fprintf('For the centrifugal compressor of the gas turbine, the static
pressure on the back disk side at the shaft is %3.0f kPa.\n',pbd(1)./1000);
    fprintf('For the centrifugal compressor of the gas turbine, the static
temperature on the back disk side at the shaft is %3.0f K.\n',Tbd(1));
end

```

Appendix 5: Matlab code for axial seal dynamic coefficients with Black's method

```

%% Dynamic coefficients for annular seal using Black's method (for LPC)
% by Lauri Rauhala

clc;
clear;

% Input data (Inlet swirl ratio expected to be 0.5)

zeta=0.1; % Entrance loss coefficient (typical value 0.1)
omega=11000*(2*pi/60); % rotational velocity, rad/s
L=0.030; % seal length, m
C=0.0005; % seal radial clearance, m
R=0.025; % seal radius, m
rho=2.8; % fluid density at outlet when pressure 1.9 bar and temperature 102 C,
kg/m3
Temp=375; % fluid temperature (102 C), K
myy=(1.458*10^-6*Temp^0.5)/(1+(110.4/Temp)); % fluid viscosity (Sutherlandin
yhtälö)

% Iteration of mean velocity

V=247.26; % axial flow velocity iterated so, that deltaP equals pressure drop
of seal (1.90 - 0.35 bar), m/s
Ra=(2*rho*V*C)/myy; % Axial Reynolds number
Rc=(rho*R*omega*C)/myy; % Circumferential Reynolds number
lambda=0.079*Ra^(-0.25)*(1+((7*Rc)/(8*Ra))^2)^0.375; % Friction loss factor
sig=lambda*(L/C);
deltaP=0.5*(1+zeta+2*sig)*rho*V^2; % This must equal pressure drop of seal
T=L/V;

% Short seal solution

myy0s=((1+zeta)*sig^2)/(1+zeta+2*sig)^2;
myy1s=((1+zeta)^2*sig+(1+zeta)*(2.33+2*zeta)*sig^2+3.33*(1+zeta)*sig^3+1.33*sig
^4)/(1+zeta+2*sig)^3;
myy2s=(0.33*(1+zeta)^2*(2*zeta-
1)*sig+(1+zeta)*(1+2*zeta)*sig^2+2*(1+zeta)*sig^3+1.33*sig^4)/(1+zeta+2*sig)^4;
myy3=(pi*R*deltaP)/lambda;

Kds=myy3*(myy0s-0.25*myy2s*omega^2*T^2);
kcs=myy3*(0.5*myy1s*omega*T);
Cds=myy3*myy1s*T;
ccs=myy3*myy2s*omega*T^2;
mds=myy3*myy2s*T^2;

% Finite length seal solution (more accurate)

myy0=myy0s/(1+0.28*(L/R)^2);
myy1=myy1s/(1+0.23*(L/R)^2);
myy2=myy2s/(1+0.06*(L/R)^2);

```

```
Kd=yyy3*(yyy0-0.25*yyy2*omega^2*T^2)
kc=yyy3*(0.5*yyy1*omega*T)
Cd=yyy3*yyy1*T
cc=yyy3*yyy2*omega*T^2
md=yyy3*yyy2*T^2
```

Appendix 6: Matlab code for axial seal dynamic coefficients with Child's method

```

%% Dynamic coefficients for annular seal using Child's method (for LPC)
% Lauri Rauhala

clc;
clear;

% Input data

zeta=0.1; % Entrance loss coefficient (typical value 0.1)
omega=11000*(2*pi/60); % rotational velocity, rad/s
L=0.03; % seal length, m
C=0.0005; % seal radial clearance, m
R=0.025; % seal radius, m
rho=2.8; % fluid density at outlet when pressure 1.9 bar and temperature 102 C,
kg/m3 CHECK THIS ONE AGAIN!
Temp=375; % fluid temperature (102 C), K
myy=(1.458*10^-6*Temp^0.5)/(1+(110.4/Temp)); % fluid viscosity (Sutherlandin
yhtälö, Petrin ratkaisusta otettu TARKISTA)

% Iteration of mean velocity

V=282.505; % axial flow velocity iterated so, that deltaP equals pressure drop
of seal (1.90 - 0.35 bar), m/s
Ra=(rho*V*C)/myy; % Axial Reynolds number
Rc=(rho*R*omega*C)/myy; % Circumferential Reynolds number
b=Ra/Rc;
lambda=0.066*Ra^(-0.25)*(1+(1/(4*b^2)))^0.375; % Friction loss factor
sig=lambda*(L/C);
deltaP=0.5*(1+zeta+2*sig)*rho*V^2; % This must equal pressure drop of seal

% Calculations

e=exp(1); % Neper's constant
beta=1/(1+4*b^2);
a=sig*(1+0.75*beta);
B=1+4*b^2*beta*0.75;
E=(1+zeta)/(2*(1+zeta+B*sig));
T=L/V;
v0=0;

% Solution

Kd=((pi*R*deltaP)/lambda)*((2*sig^2)/(1+zeta+2*sig))*(1.25*E-
((omega*T)^2/(4*sig))*(0.5*(1/6+E)+(2*v0/a)*((E+(1/a^2))*(1-e^(-a))-
(0.5+1/a)*e^(-a))))
kc=((pi*R*deltaP)/lambda)*((omega*T*sig^2)/(1+zeta+2*sig))*((E/sig)+(B/2)*(1/6+
E)+(2*v0/a)*(E*B+((1/sig)-(B/a))*((1-e^(-a))*(E+0.5+(1/a))-1)))
Cc=((pi*R*deltaP)/lambda)*((2*sig^2*T)/(1+zeta+2*sig))*(E/sig+B/2*(1/6+E))
cc=((pi*R*deltaP)/lambda)*((2*omega*T^2*sig)/(1+zeta+2*sig))*(0.5*(1/6+E)+(v0/a
)*((1-e^(-a))*(E+0.5+1/a^2)-(0.5+(e^(-a)/a))))

```

$$md = (\pi R \Delta P) / \lambda * ((\sigma * (1/6 + E)) / (1 + \zeta + 2 * \sigma)) * T^2$$

Appendix 7: Matlab code for aerodynamic cross-coupled stiffness by an impeller

```

%% Aerodynamic cross-coupled stiffness caused by impeller
% Code by Lauri Rauhala

% Alford's method

w=11000; % Rotational speed, rpm
P=1000; % Power, W
T=9548.8*P/w; % Torque, Nm
beta=2.5; % efficiency factor, estimated
D=0.3683; % blade pitch mean diameter, m
H=0.0890; % blade height, m
K=(beta*T)/(D*H) % cross-coupled stiffness, N/m

% Wachel's method

P=1000; % Power, W
hp=P*1.3402209; % Power, hp
Mw=28.96; % Molecular weight of air, g/mol
m2i=39.3700787; % Meter to inch factor
D=0.3683*m2i; % blade pitch mean diameter, inch
H=0.0890*m2i; % blade height, inch
rpm=11000; % stage speed, rpm
pd=2.8; % fluid density at discharge, kg/m3
ps=1.7; % fluid density at suction, kg/m3
K=175*(6300*hp*Mw)/(D*H*rpm) % cross-coupled stiffness, N/m

```